UNIVERSITÉ DE LORRAINE | BIBLIOTHÈQUES UNIVERSITAIRES

AVERTISSEMENT
DROIT D'AUTEUR

Ce document est le fruit d'un long travail approuvé par le jury de soutenance et mis à disposition de l'ensemble de la communauté universitaire élargie.

Il est soumis à la propriété intellectuelle de l'auteur. Ceci implique une obligation de citation et de référencement lors de l'utilisation de ce document. Toute contrefaçon, plagiat ou reproduction illicite encourt une poursuite pénale.

Contact bibliothèque : ddoc-theses-contact@univ-lorraine.fr
(Cette adresse ne permet pas de contacter les auteurs)

Code de la Propriété Intellectuelle. articles L 122. 4
Code de la Propriété Intellectuelle. articles L 335.2- L 335.10

UNIVERSITÉ DE LORRAINE
34 COURS LÉOPOLD — CS 25233
54052 NANCY CEDEX
TÉL : 03 54 50 54 00
CONTACT@UNIV-LORRAINE.FR
WWW.UNIV-LORRAINE.FR

Thèse

Présentée et soutenue publiquement pour l'obtention du titre de

DOCTEUR DE l'UNIVERSITE DE LORRAINE

Mention : Génie des systèmes industriels

par **Xiaolong Wang**

Conception et fabrication de structures poreuses superhydrophobes par impression 3D et séparation de phases pour la séparation huile-eau

3 décembre 2025

Membres du jury :

Rapporteurs :	**M. Frédéric VIGNAT**	**PU, G-SCOP, Université Grenoble Alpes, Grenoble, France**
	M. Rémy HOUSSIN	**MCF HDR, ICube, Université de Strasbourg, France**
Président du jury :	**Mme. Cécile NOUVEL**	**PU, LRGP, Université de Lorraine, Nancy, France**
Examinateurs :	**M. Gianluca PERCOCO**	**PU, Politecnico di Bari, Bari, Italy**
Directeur(s) de thèse :	**M. Hakim BOUDAOUD**	**PU, ERPI, Université de Lorraine, Nancy, France**
	M. Alaa HASSAN	**MCF, ERPI, Université de Lorraine, Nancy, France**
Membres invités :	**M. Xianhu LIU**	**PU, NERC, Zhengzhou Université, Zhengzhou, China**
	M. Guohua HU	**PU, LRGP, Université de Lorraine, Nancy, France**

Acknowledgement

First and foremost, I would like to express my sincere gratitude to my supervisors, Dr. Alaa Hassan and Prof. Hakim Boudaoud, for giving me the opportunity to pursue my doctoral studies in France.

I would like to sincerely thank Prof. Hakim Boudaoud for his steady guidance and generous support throughout my PhD. His remarkable expertise and broad academic vision have always impressed me, and I have benefited greatly from his constructive insights and critical thinking. Beyond his role as a supervisor, he has been a mentor who treated me with kindness and respect, and often a friend with whom I could share both academic ideas and life stories. His combination of scientific rigor and human warmth made a lasting impact on my research and personal growth.

I would also like to extend my sincere thanks to Dr. Alaa Hassan. His strong academic background and deep understanding of industrial applications provided me with essential guidance throughout my research. He was always responsive to my questions, offering timely and effective support whenever I needed it. Beyond academics, he greatly helped me adapt to life in France during my early days—personally showing me around the laboratory, assisting me in finding accommodation, and offering thoughtful advice as I settled into a new environment. Thanks to his support, I was able to begin this journey with confidence and peace of mind.

I would also like to express my gratitude to Prof. Guohua Hu and Prof. Cécile Nouvel from LRGP, who provided me with generous support even before I officially began my PhD journey in France. Although I eventually joined a different research group due to various circumstances, they continued to offer me valuable scientific feedback during our annual meetings over the years. Their encouragement and insightful suggestions contributed meaningfully to the progress and refinement of this project. Moreover, their academic perspectives have greatly enriched my way of thinking and helped me develop a more rigorous scientific mindset.

I am also sincerely grateful to the members of my jury, Frédéric Vignat, Rémy Houssin, Cécile Nouvel, and Gianluca Percoco, for their valuable time, insightful comments, and constructive feedback, which have greatly improved the quality of this thesis.

I am deeply grateful to Prof. Xianhu Liu from Zhengzhou University, who was also my master's supervisor and the one who first guided me into the world of academic research. His mentorship laid the foundation for my scientific journey. During my doctoral studies, he continued

to support me generously, especially by facilitating experimental work in China and assisting with research funding applications. I have always admired his broad knowledge, tireless dedication, and unwavering work ethic, which continue to inspire me in both research and life.

I would like to thank Mr. Benjamin Ennesser-Serville for his continuous technical support throughout my research. He was always quick to respond to any questions I had regarding the equipment and ensured that my experiments could proceed smoothly. I am also grateful to Prof. Mauricio Camargo, the head of our team, for creating a dynamic and supportive research environment. My sincere thanks go to all the staff members at ERPI and LF2L for providing me with the best possible platform to carry out my work. Their professionalism and dedication have played an important role in the progress of this project.

I would like to sincerely thank my two senior colleagues, Fangkai Xue and Yongqiang Tu, from whom I learned a great deal about scientific research. I am also deeply grateful for their support in my daily life, especially during the early stages of my PhD. Many thanks to Jaydeep, Tamara, Li Tongchun and all my colleagues, I truly enjoyed the joyful moments we shared together.

A special thanks goes to my fellow PhD students Xin Wang, Qingsen Gao, and Mingjie Feng, for their help with experiments and data processing, as well as for the mental support they offered throughout the journey. “Winner winner, chicken dinner”—I will always remember our shared motto.

I also gratefully acknowledge Bo Zhu, Yiding Wang, Qianwei Liu, and Jingjing An for their assistance in my experimental work.

Finally, I would like to express my deepest gratitude to my family for their unwavering support throughout this journey. A very special thanks goes to my girlfriend, Dr. Xinyi Wei. Together, we have traveled to remote islands in the Atlantic Ocean, walked through the snow-covered peaks of the Alps, and written chapters of our lives along the blue coasts of Spain. Her presence has been my greatest source of strength and comfort. After all, true love is best expressed through quiet, enduring companionship.

Xiaolong WANG

Nancy

June 2025

Abstract

Superhydrophobic materials, inspired by natural surfaces such as lotus leaves and water striders, have shown exceptional potential in oil–water separation due to their selective wettability. However, conventional fabrication methods—such as electrospinning, sol–gel processing, and templating—often involve complex steps and limited scalability. This thesis explores the development of bioinspired superhydrophobic membranes and three-dimensional (3D) porous structures for efficient oil–water separation using 3D printing techniques, particularly fused filament fabrication (FFF).

First, a comprehensive review is conducted to trace the origins of hydrophobicity in natural structures, such as lotus leaves, desert beetles, and rose petals. These surfaces feature hierarchical micro/nanostructures and low-surface-energy coatings, which inspired the development of synthetic materials with self-cleaning, antifouling, and water-repellent properties. Building upon this foundation, recent studies were reviewed that examine both 2D and 3D hydrophobic surfaces fabricated via 3D printing, highlighting the benefits and limitations of each.

Next, this work presents a simplified method for fabricating 2D porous membranes using fused filament fabrication (FFF) 3D printing combined with a surface spray-coating of silica nanoparticles. By adjusting slicing parameters such as infill density, pore sizes were precisely controlled without the need for CAD modeling. The resulting membranes exhibited a water contact angle of up to 154.6°, high separation efficiency (above 90%), and excellent oil flux performance (up to 81.89 $mL \cdot cm^{-2} \cdot min^{-1}$) for various organic solvents.

Finally, a novel 3D cubic porous architecture was developed using optimized FFF printing parameters to achieve pore heights as small as 186.7 μm. Surface modification with nano-silica produced a superhydrophobic coating with a contact angle of 158.2°. The printed structure showed strong mechanical durability and long-term performance in continuous suction-driven separation, maintaining an 87.2% efficiency for over 24 hours. This marks the first report of directly printing 3D porous structures with uniform pores for this purpose.

Overall, this thesis offers a customizable and cost-effective strategy for fabricating superhydrophobic materials for oil–water separation.

Key words: Additive manufacturing, Fused Filament Fabrication, Superhydrophobic, Oil–water separation, Porous architectures

Résumé

Les matériaux superhydrophobes, inspirés des surfaces naturelles telles que les feuilles de lotus et les pattes d'insectes aquatiques, ont démontré un potentiel remarquable pour la séparation huile-eau grâce à leur mouillabilité sélective. Toutefois, les méthodes de fabrication conventionnelles — telles que l'électrofilage, le procédé sol-gel ou l'utilisation de moules — impliquent généralement des étapes complexes et offrent une évolutivité limitée. Cette thèse explore le développement de membranes superhydrophobes bio-inspirées et de structures poreuses tridimensionnelles (3D) dédiées à la séparation efficace de mélanges huile-eau, en s'appuyant particulièrement sur la technique d'impression 3D par dépôt de filament fondu (FFF, Fused Filament Fabrication).

Dans un premier temps, une revue approfondie est menée pour retracer les origines de la superhydrophobicité observée dans les structures naturelles, notamment les feuilles de lotus, les coléoptères du désert et les pétales de rose. Ces surfaces se caractérisent par des micro/nanostructures hiérarchiques et des revêtements à faible énergie de surface, ce qui a inspiré le développement de matériaux synthétiques dotés de propriétés autonettoyantes, antisalissures et hydrophobes. Sur cette base, des études récentes portant sur des surfaces hydrophobes 2D et 3D fabriquées par impression 3D sont analysées, mettant en lumière leurs avantages et limites respectifs.

Ensuite, cette thèse présente une méthode simplifiée de fabrication de membranes poreuses 2D par impression 3D FFF, combinée à un revêtement de surface par pulvérisation de nanoparticules de silice. En ajustant les paramètres de découpage, tels que la densité de remplissage, il est possible de contrôler précisément la taille des pores sans recourir à la modélisation CAO. Les membranes obtenues présentent un angle de contact avec l'eau allant jusqu'à 154,6°, une efficacité de séparation supérieure à 90 % et un flux d'huile pouvant atteindre 81,89 $mL \cdot cm^{-2} \cdot min^{-1}$ pour divers solvants organiques.

Enfin, une architecture poreuse cubique 3D innovante a été développée à l'aide de paramètres FFF optimisés, permettant d'atteindre des hauteurs de pores aussi petites que 186,7 μm. Une modification de surface par pulvérisation de nano-silice a permis d'obtenir un revêtement superhydrophobe avec un angle de contact de 158,2°. La structure imprimée a démontré une excellente durabilité mécanique ainsi qu'une performance stable dans un système de séparation

continue par aspiration, maintenant une efficacité de 87,2 % pendant plus de 24 heures. Il s'agit du premier travail rapportant l'impression directe de structures poreuses 3D uniformes à des fins de séparation huile-eau.

En somme, cette thèse propose une stratégie personnalisable, rentable et respectueuse de l'environnement pour la fabrication de matériaux superhydrophobes destinés à des applications de séparation huile-eau.

Mots clés : Fabrication additive, Dépôt de filament fondu, Superhydrophobie, Séparation huile-eau, Architectures poreuses

Contents

Abstract i

Résumé ii

Résumé étendu en français xiv

1 Chapitre 1 : introduction xv

1.1 Contexte générale xv

1.2 Contenu de recherche xviii

2 Chapitre 2 : Etat de l'art sur les techniques de séparation huile-eau xx

3 Chapitre 3 : Revue sur l'impression 3D de matériaux hydrophobes bio-inspirés : séparation huile-eau, collecte d'eau et autres applications xxi

4 Chapitre 4 : Méthode simplifiée d'impression 3D pour la fabrication d'une membrane superhydrophobe de séparation huile-eau à taille de pores contrôlable xxii

5 Chapitre 5 : Architectures poreuses superhydrophobes imprimées en 3D pour une séparation continue huile-eau xxv

6 Chapitre 6 : Conclusions et perspectives xxvi

English Version *Design and fabrication of superhydrophobic porous structures by 3D printing and phase separation for oil–water separation* 1

Chapter 1: Introduction 2

1.1 Context of the present study 2

1.2 Research contents 5

1.3 Structure of the thesis 7

Chapter 2: State of the art on oil–water separation techniques 9

2.1 Introduction 9

2.2 Environmental Challenges of Oil and Organic Solvent Spills 9

2.3 Conventional Oil–Water Separation Techniques and Their Limitations 10

2.3.1 Overview of Conventional Techniques 10

2.3.2 Mechanisms and Challenges 11

2.4 Superhydrophobic Materials for Selective Oil–Water Separation 12
2.4.1 Principles of Superhydrophobicity 12
2.4.2 Mechanisms of Selective Oil–Water Separation 13
2.4.3 Fabrication of Superhydrophobic Materials 14
2.5 Summary and Comparative Analysis 22
Chapter 3: A Review on 3D Printing of Bioinspired Hydrophobic Materials: Oil–Water Separation, Water Harvesting, and Diverse Applications 25
3.1 Introduction to the Chapter 25
3.2 Introduction 25
3.3 Theoretical background of wettability 28
3.3.1 The wettability of the surface 28
3.3.2 The theory of hydrophobicity 28
3.3.3 The theory of intrinsic wetting threshold 30
3.4 3D-printing technology 31
3.5 Fabrication of hydrophobic products by 3D-printing 34
3.5.1 3D model design 39
3.5.2 Raw material preparation 40
3.5.3 Printing process 43
3.5.4 After printing process 45
3.6 Application of 3D-printed hydrophobic material 47
3.6.1 Oil-water separation 47
3.6.2 Water harvest 50
3.6.3 Drag reduction 54
3.6.4 4D-printing 57
3.7 Conclusions and perspectives 58
3.8 Link to Experimental Chapters 60
Chapter 4: Simplified 3D Printing Method for Fabrication of Superhydrophobic Oil-Water Separation Membrane with Controllable Pore Size 61

4.1 Introduction to the Chapter 61
4.2 Introduction 61
4.3 Material and methods 64
4.3.1 Material 64
4.3.2 Fabrication of 2D PLA porous membrane 64
4.3.3 Modification of PLA membrane 65
4.3.4 Characterizations 65
4.3.5 Oil filtration test 65
4.4 Result and discussion 66
4.4.1 Fabrication of 2D PLA porous membrane 66
4.4.2 Hydrophobic post-treatment 71
4.4.3 Oil-water separation experiment 75
4.5 Conclusion 77
Chapter 5: Innovative 3D-Printed Superhydrophobic Porous Architectures for Continuous Oil-Water Separation 79
5.1 Introduction to the Chapter 79
5.2 Introduction 79
5.3 Materials and Methods 81
5.3.1 Material 81
5.3.2 Fabrication of 3D PLA porous architectures 82
5.3.3 Hydrophobic Modification 84
5.3.4 Characterizations 84
5.3.5 Oil-water separation test 84
5.4 Results and Discussion 85
5.4.1 Fabrication of Porous Architectures 85
5.4.2 Hydrophobic modification 92
5.4.3 Oil-water separation experiment 96
5.5 Conclusion 99
Chapter 6: General Discussion, Conclusions and Perspectives 101

6.1 Integrated Discussion of Chapters 4–5 101
6.2 Scientific Contributions 102
6.3 Scalability Considerations for FFF-based Architectures 103
6.4 Limitations 103
6.5 Perspectives 104
List of Publications 106
References 107

List of Figures

Figure 1.1 **a** Image of spilled oil and **b** Oil cleaning skimmers. Source: International Tanker Owners Pollution Federation (ITOPF), [1]. 3

Figure 1.2 Superhydrophobic behavior on **a** lotus leaves (Image by SureshMukhiya, licensed under CC BY-SA 4.0, via Wikimedia Commons.) and **b** water striders. 4

Figure 1.3 Schematic overview of the research framework. SEM images include original scale bars (200 μm). 6

Figure 2.1 Schematic illustration of bioremediation process [31]. 11

Figure 2.2 **a** Fabrication process of Silica-PAN membrane [45]. **b** Oil-water separation process of PSF based membrane [46]. 15

Figure 2.3 **a** Schematic illustration of the preparation of the PDMS sponge. **b** photograph of the freshly prepared PDMS sponge. **c** SEM image of a sponge portion (scale bar=500μm) [54]. **d** Schematic diagram for the preparation of $NiFe_2O_4$ based porous composites [55]. 17

Figure 2.4 **a** Schematic illustration of the preparation of SOCM [61]. **b** Schematic diagram for the preparation of cotton based hydrophobic fabric and its oil-water separation process. 19

Figure 2.5 **a** The feed and filtrate of PVDF based membrane and the optical microscopy images [63]. **b** Schematic of the phase inversion process [64]. 21

Figure 3.1 Four innovative application fields for 3D-printing of bioinspired hydrophobic materials. 27

Figure 3.2 Schematic representation of a water droplet on ideal solid surface refers to **a** the Young equation, and on surface with roughness refers to the **b** Wenzel model, **c** Cassie model, and **d** micro/nano hybrid surface; e Intrinsic wetting threshold $\theta *$ schematic diagram for a given liquid and design pricinple of slective liquid adsorb material []. 30

Figure 3.3 Schematic summary of 3D-printing techniques [115]. 32

Figure 3.4 **a** Schematic of universal 3D-printing process, **b** Number of publications achieving hydrophobicity in different promotion route, **c** Temporal distribution of the publications and **d** Proportion of different applications. 36

Figure 3.5 **a** Schematic of the fabrication procedure for hydrophobic PLS structure by SLA technique and its variety shapes of printed structure; **b** CA of samples fabricated in different

orientation, resolution, shapes [185]; **c** S. Molesta leaf and its hydrophobicity as well as the SEM image of the surface with eggbeater structure; **d** SolidWorks modeled eggbeater structure [96].40

Figure 3.6 Schematic of the fabrication procedure of **a** PDMS based mechanically durable superhydrophobic porous membrane via DIW technique [187]; **b** Phase-change-enabled, rapid, high-resolution of soft silicone-based material via DIW technique [188] and **c** Superhydrophobic objects with bulk nanostructure via DLP technique [191]..... 42

Figure 3.7 **a** Illustration of key parameters and procedure in the printing process for Ratchetlike structure [95]; **b** Flow diagram for the magnetic driven fabrication of hybrid hierarchical structures; **c** steps for printing the hierarchical surface structures [192]. 44

Figure 3.8 Schematic of the fabrication procedure of **a** PDMS sponge fabricated with PCL template and micro morphology **b** [196]; **c** 3D PDMS surface fabricated with PLA template and micro morphology **d** [197]; **e** Dip-coating method for the fabrication of superhydrophobic PLA surface [117]. 46

Figure 3.9 **a-c** 3D-printing oil recycling membrane and **d** ideal oil collector floating on the water surface [204]; **e** Hydrophobic cooper mesh and 3D-printing PVDF skeleton hybrid oil collector and **f** its pumping application [205]; **g** Cactus inspired oil adsorbent and schematic of its high oil-storage [196]..... 49

Figure 3.10 **a-c** Optical image of cactus at different viewing angle; **d** SEM image of a single spine and three divided zones; **e** Schematic of water collection steps on single spine [207]; **f** Fabrication process of cactus-inspired surface via 3D-printing; **g** Water harvesting behavior and h SEM image of the fabricated surface [213]. 52

Figure 3.11 **a** Schematic about water harvesting behavior of the Namib desert beetle and **b** the 3D-printing inspired surface; **c** Water collection efficiency of surface with different coatings [209]; **d** UV-induced controllable diffusion method and 3D-printing technology for the fabrication of bio-inspired water harvesting surface; **e** Water collection efficiency of surface with different cone distance and f wholes or without wholes [97]. 54

Figure 3.12 **a** SEM image of shark skin with denticles covered by micro riblets [215,216]; **b** 3D model of denticles; **c** Surface and **d** cross-section of 3D-printing shark skin-like structure; **e** Schematic of multiscale 3D-printing, different color means different layers to printing; **f** View of

cross-section for 3D-printing with different resolution [156]; **g** Special surface microstructure inspired by nepenthes and h its' drag reduction performance [219]. 56

Figure 3.13 **a** Fabrication process of shape-shifting actuator; **b** Strip and **c** flower shape actuator with sequential water response ability [224]. (Scale bar: 10 mm.)..... 58

Figure 4.1 Comparison of the fabrication processes between prior work and this work..... 64

Figure 4.2 **a** Model building and slicing process of PLA membrane with different infill percentage. **b** SEM images (Scale bar is 200 μm), **c** digital photograph and **d** pore size distribution graph of samples with different infill percentage (Scale bar is 1 cm). d Pore size distribution of different samples. 67

Figure 4.3 **a** The mesh exhibited superhydrophobic characteristics with a positive pressure differential ($\Delta P > 0$), preventing the passage of water through its structure. **b** Conversely, the mesh demonstrated superoleophilic properties with a negative pressure differential ($\Delta P < 0$), allowing for permeability to oil. Here, O represents the center of the spherical cap of the meniscus, and R signifies the radius of curvature of the spherical cap of the meniscus. **c** Water Pressure Resistance of Membranes: **d** M70S, **e** M80S and **f** M90S. **g** Water-blocking height (cm). 70

Figure 4.4 **a** Contact angle of samples with different infill percentage and spray cycles. Digital photography of M90 and **b** its water contact angle and **c** oil contact angle (hexadecane). The phenomena of **d** water droplet sliding and **e** the silver mirror effect. SEM images of **f** M90 and **g** M90S. 73

Figure 4.5 Water absorption of **a** M90 and **b** M90S, **c** Mass increase of different samples. Contact angle of M90S in **d** water impact test and **e** tape peeling test. **f** Contact angle of M90S in different time periods and pH levels. 75

Figure 4.6 **a** Dichloromethane -water separation process by M90S. **b** Flux of different samples and oils. **c** Separation efficiency for different oils. 77

Figure 5.1 **a** Three-view schematic diagram of the diamond pore structure; **b** Detailed top-view illustration; **c** Complete 3D model of the sample; **d** Magnified detail of the pore structure; **e** Digital model of the sliced sample prepared for 3D printing. 82

Figure 5.2 **a** Three-view schematic diagram of the square pore structure; **b** Detailed top-view illustration; **c** Complete 3D model of the sample; **d** Magnified detail of the pore structure; **e** Digital

model of the sliced sample prepared for 3D printing. SEM images of printed square pore structures **f** S1, **g** S2, **h** S3 and **I** S4. (Scale bar is 200 μm). 83

Figure 5.3 **a** square and **b** diamond pore structure and printing details..... 87

Figure 5.4 SEM images of diamond pore structure. (**a**)& (**e**) D1, (**b**)& (**f**) D2, (**c**)& (**g**) D3 and (**d**)& (**h**) D4. Scale bar is 200 μm. (Blue box: Designed pore size in the model; Red circle: Defect; Blue arrow: Pore height; Red arrow: Pore width, respectively.) 88

Figure 5.5 SEM images of diamond pore structure. (**a**)& (**d**) D3LT, (**b**)& (**e**) D3LTF, (**c**)& (**f**) D3LTE. Scale bar is 200 μm. (Blue box: Designed pore size in the model; Red circle: Defect; Blue arrow: Pore height; Red arrow: Pore width, respectively.) (**g**) pore size distribution graph of different samples. 89

Figure 5.6 SEM images of diamond pore structure with **a-c** 0.4 mm and **d-f** 0.2 mm pore height. 90

Figure 5.7 SEM images of diamond pore structure. **a**& **d** D3LTE-10, **b**& **e** D3LTE-15, **c**& **f** D3LTE-20, **g**& **i** D3LTE-25 and **h**& **j** D3LTE-30. Scale bar is 200 μm. **k** Relationship between layer height and printing time. Scale bar is 200 μm. 91

Figure 5.8 **a** Hydrophobic modification process and comparison of water contact angles before and after modification of D3LTE. **b** Water contact angles of different samples. Digital photograph of D3LTE and **c** its water contact angle and **d** oil contact angle (cyclohexane). **E** Photographs of the D3LTE surface submerged in water before and after modification..... 93

Figure 5.9 **a** Experiment demonstrating the internal water pressure resistance of modified D3LTE over 24 hours. **b** Contact angle variation of modified D3LTE during the peeling test. SEM images of **c** the sample with a 0.4 mm pore size and **d** its modified version. SEM images of **e** unmodified D3LTE and **f** modified D3LTE. **g** Elemental mapping images of modified D3LTE. Scale bar is 200 μm. 95

Figure 5.10 **a** Schematic diagram of the continuous pumping oil-water separation experiment. **b** Photographs taken during the continuous pumping oil-water separation process. **c** Image of the separated oil and water after the experiment. **d** Flow rate of different samples (based on pore height) during oil-water separation. **e** Separation efficiency of different samples. **f** Efficiency variation of modified D3LTE during continuous oil-water separation over 24 hours. 96

Figure 5.11 **a** Schematic diagram of the internal oil-water separation method and its corresponding photos. **b** Schematic diagram of the adsorption-based oil-water separation method combines with sponge and its corresponding photos. 99

List of Tables

Table 2-1 Simplified comparison of fabrication methods for superhydrophobic oil-water separation materials. 24

Table 3-1 Selected related publication and detailed description. (In 'Process for hydrophobicity' part, '1,2,3,4' represents 'design of 3D models', 'preparation of raw material', 'printing process' and 'after printing process', respectively. 37

Table 4-1 Parameter for the printing PLA membrane 65

Table 5-1 Printing parameter for the diamond porous structure 83

Table 5-2 Parameter for the Square porous structure 83

Résumé étendu en français

1 Chapitre 1 : introduction

1.1 Contexte générale

Au cours des dernières décennies, les fuites accidentelles et opérationnelles de pétrole, de solvants organiques et d'autres polluants non miscibles ont constitué de graves menaces environnementales pour les écosystèmes aquatiques et la santé humaine [1]. Comme illustré à la Figure 1.1a, ces polluants — issus notamment des marées noires, des procédés chimiques ou du rejet d'effluents industriels — peuvent persister dans l'environnement, perturber les équilibres écologiques et provoquer une contamination durable des sols et des milieux aquatiques [2]. Selon la International Tanker Owners Pollution Federation (ITOPF), plus de 1 000 déversements d'hydrocarbures marins à grande échelle ont été signalés dans le monde depuis 1970, avec des catastrophes majeures telles que la marée noire de Deepwater Horizon en 2010, qui a libéré près de 5 millions de barils de pétrole brut dans le golfe du Mexique [3]. Plus fréquemment encore, des déversements localisés dus à des rejets industriels ou à des accidents de transport terrestre entraînent une contamination persistante des sols et des nappes phréatiques [4]. Ces événements de pollution perturbent non seulement la biodiversité, mais provoquent également une dégradation écologique durable, des pertes économiques dans les secteurs de la pêche et du tourisme, ainsi qu'une inquiétude croissante en matière de santé publique.

Les méthodes traditionnelles de traitement des marées noires, telles que la combustion, les épurateurs mécaniques (skimmers) [5] (voir Figure 1.1b), les dispersants chimiques [6] et la biodégradation microbienne [7] présentent certains avantages dans des conditions spécifiques, mais sont souvent limitées par une faible sélectivité, une pollution secondaire et des exigences opérationnelles complexes [8]. Par exemple, la combustion in situ [9] nécessite des conditions météorologiques précises et peut générer des sous-produits toxiques ; les agents chimiques peuvent disperser le pétrole mais introduisent également de nouveaux risques écologiques [6] ; la bioremédiation [10] est respectueuse de l'environnement mais généralement trop lente pour les interventions d'urgence. Ces limites soulignent le besoin urgent de matériaux et de technologies capables de permettre une séparation huile-eau sélective, efficace et respectueuse de l'environnement dans divers scénarios.

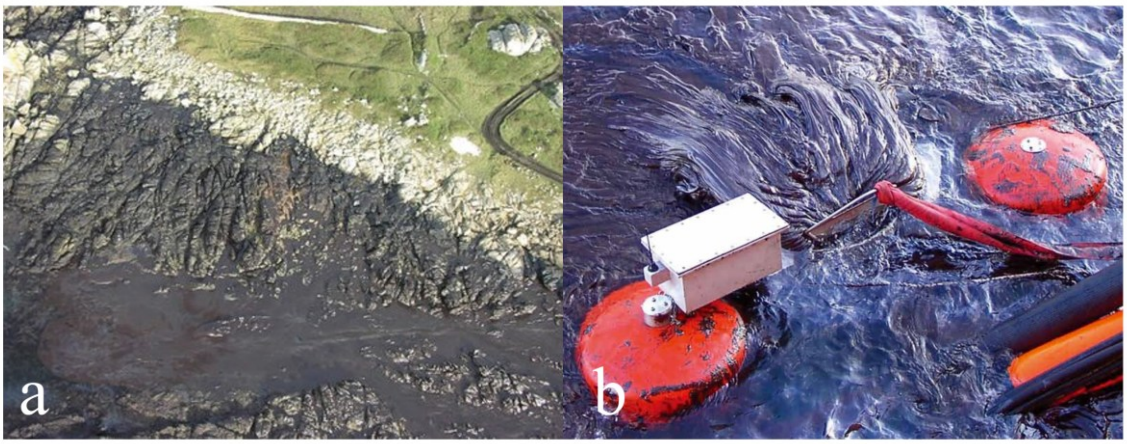

Figure 1.1 ***a****. Image d'un déversement de pétrole;* ***b****. Équipements d'écrémage de surface. Source: International Tanker Owners Pollution Federation (ITOPF) [1].*

Inspirés par des surfaces naturelles telles que les feuilles de lotus (Figure 1.2a), les insectes patineurs d'eau (Figure 1.2b), les coléoptères du désert et les pétales de rose, les matériaux superhydrophobes — présentant des angles de contact avec l'eau supérieurs à 150° — suscitent un intérêt croissant dans le domaine de la séparation huile-eau [11]. Ces surfaces possèdent généralement des micro/nanostructures hiérarchiques combinées à des revêtements à faible énergie de surface, ce qui leur permet de repousser efficacement l'eau tout en laissant l'huile passer ou être absorbée [12]. Ce mécanisme de séparation passive et sélective permet d'améliorer considérablement l'efficacité globale du procédé. Ces dernières années, les chercheurs ont développé diverses stratégies pour fabriquer de telles surfaces, notamment l'électrofilage [13], la séparation de phases [14], les revêtements sol-gel [15] et les méthodes par moulage [16]. Cependant, ces approches impliquent souvent des procédures de fabrication complexes, peu adaptées à une production à grande échelle. En outre, elles rencontrent encore des difficultés à garantir une uniformité structurelle et à offrir une flexibilité suffisante pour des conceptions personnalisées ou spécifiques aux applications.

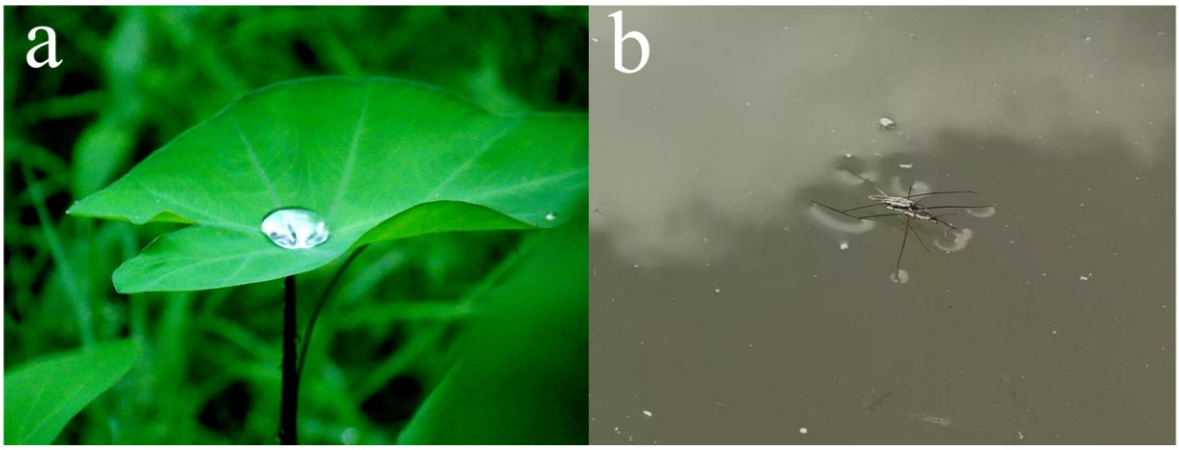

Figure 1.2 ***a****. Comportement superhydrophobe sur une feuille de lotus (Image de SureshMukhiya, sous licence CC BY-SA 4.0, via Wikimedia Commons.) ;* ***b****. Insectes patineurs d'eau observés à la surface de l'eau.*

Par rapport à d'autres méthodes de fabrication, l'impression 3D présente trois principaux avantages dans le développement de matériaux superhydrophobes pour la séparation huile-eau. Premièrement, l'impression 3D englobe une variété de technologies — telles que la stéréolithographie (SLA) [17], le traitement numérique de la lumière (DLP) [18] et la fabrication par filament fondu (FFF) [19], chacune étant compatible avec un large éventail de matériaux et adaptable à divers scénarios d'application. Deuxièmement, avec l'aide de logiciels de modélisation, les chercheurs peuvent concevoir des structures superhydrophobes personnalisées de manière hautement reproductible et évolutive. Troisièmement, la nature automatisée de l'impression 3D réduit considérablement les besoins en main-d'œuvre et facilite le passage à l'échelle industrielle. Grâce à ces avantages, l'impression 3D est devenue un outil prometteur pour le développement de matériaux fonctionnels de séparation, y compris, mais sans s'y limiter, à la séparation huile-eau.

Parmi les techniques d'impression 3D disponibles, la FFF s'est imposée comme une méthode prometteuse et polyvalente pour la fabrication de matériaux superhydrophobes destinés à la séparation huile-eau. La FFF permet la construction numérique de géométries poreuses par dépôt couche par couche de filaments thermoplastiques, tels que l'acide polylactique (PLA). Par rapport à d'autres technologies de fabrication additive, la FFF présente deux avantages majeurs. Premièrement, la FFF est la technique la plus largement utilisée, offrant un faible coût d'équipement et une grande simplicité d'emploi, ce qui la rend particulièrement adaptée à la production à grande échelle [20]. Deuxièmement, elle est hautement compatible avec les

polymères biodégradables comme le PLA et ne nécessite généralement pas d'agents supplémentaires tels que des solvants de démoulage pendant le processus d'impression — ce qui est en adéquation avec les principes de la fabrication durable [21]. Cependant, la principale limite de la FFF réside dans sa résolution d'impression relativement faible [22], ce qui nécessite un ajustement fin des paramètres d'impression ainsi qu'une optimisation de la conception structurelle afin d'améliorer la qualité et les performances du produit final.

1.2 Contenu de recherche

Dans ce contexte, l'objectif global de cette thèse est d'explorer le potentiel de la fabrication par dépôt de fil fondu (FFF, Fused Filament Fabrication) pour concevoir des matériaux poreux superhydrophobes destinés à une séparation huile-eau efficace. Parmi les différentes techniques d'impression 3D, la FFF se distingue comme la plus économique, la plus simple d'utilisation et la plus facile à industrialiser, offrant ainsi une voie privilégiée pour le développement d'architectures contrôlables et évolutives. L'utilisation du PLA, un polymère biosourcé, biodégradable, peu coûteux et largement accessible, confère en outre un caractère durable, respectueux de l'environnement et abordable à cette approche. L'étude se concentre sur deux aspects clés : la simplification du procédé de fabrication et le développement de structures poreuses architecturées en 3D.

Pour aborder cet objectif de manière systématique, l'approche de recherche est illustrée à la Figure 1.3 :

Nous commençons par une revue de la littérature et une base théorique sur les matériaux superhydrophobes imprimés en 3D et leurs applications (Figure 1.3 : Revue de la littérature sur les matériaux hydrophobes imprimés en 3D et leurs applications). Cette revue couvre les avancées récentes en matière de stratégies de fabrication, de modèles de mouillage, de principes de conception et d'applications représentatives, avec une attention particulière portée aux mécanismes de séparation huile-eau et aux techniques d'amélioration de l'hydrophobicité. Deux défis majeurs sont mis en évidence dans les travaux actuels : (1) les méthodes de fabrication sont souvent trop complexes et chronophages ; (2) il existe un manque d'études exploitant pleinement le potentiel de l'impression 3D pour créer des structures poreuses architecturées.

Suite à cette analyse, nous avons d'abord mené une étude visant à simplifier la fabrication de membranes planes 2D (Figure 1.3 : Membrane 2D avec procédé simplifié). En ajustant le

pourcentage de remplissage dans le logiciel de tranchage, nous avons supprimé le besoin de modélisation préalable. Parallèlement, l'hydrophobicité a été renforcée par un revêtement en spray de nanoparticules de silice, et la performance de séparation huile-eau a été évaluée.

Nous avons ensuite développé des structures architecturées imprimées en 3D comportant des canaux poreux orientés verticalement (Figure 1.3 : Structures 3D architecturées). Ces structures ont été obtenues grâce à une modélisation optimisée et à un contrôle précis des paramètres d'impression. Par rapport aux membranes 2D traditionnelles, ces matériaux sont mieux adaptés aux systèmes de séparation huile-eau en continu et sous pompe, grâce à leur uniformité structurelle et leur régularité spatiale.

À travers cette démarche de recherche multidimensionnelle, la thèse vise à clarifier à la fois les avantages et les limites de l'impression 3D dans la construction de systèmes fonctionnels de séparation superhydrophobes, et à contribuer à l'élaboration de connaissances fondamentales pour le développement futur de plateformes de séparation huile-eau personnalisables et évolutives.

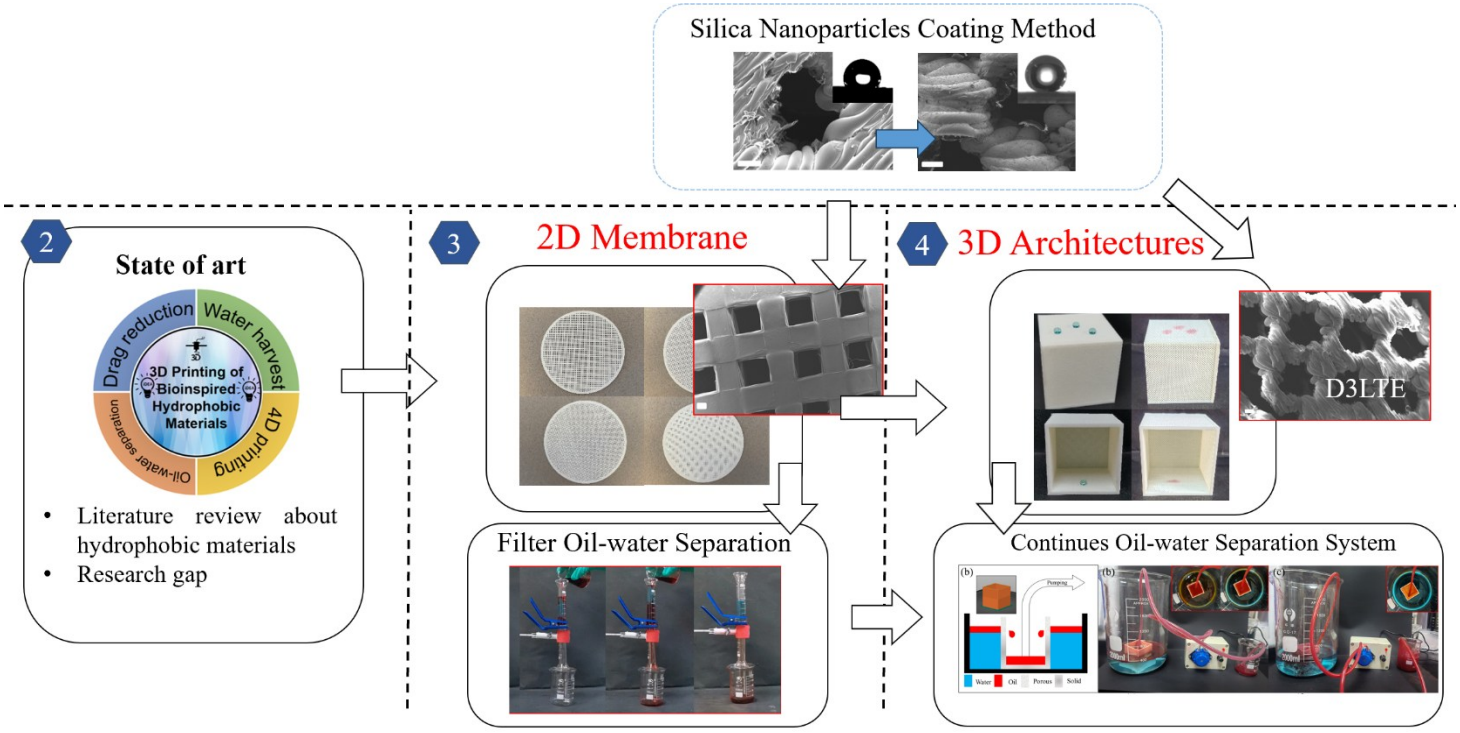

Figure 1.3 Vue schématique du cadre de recherche. Les images MEB incluent les barres d'échelle d'origine (200 µm).

2 Chapitre 2 : Etat de l’art sur les techniques de séparation huile-eau

Puisqu'il s'agit d'une recherche transdisciplinaire à travers la séparation huile-eau et la fabrication additive, une revue de la littérature couvrant ces deux domaines est indispensable. Ce chapitre présente une revue systématique des fondements théoriques et des avancées technologiques dans le domaine des matériaux poreux superhydrophobes pour la séparation huile-eau. Il commence par une analyse des risques environnementaux liés aux déversements de pétrole brut et de solvants organiques, suivie d’un survol des méthodes conventionnelles de séparation huile-eau ainsi que de leurs limites intrinsèques. Ensuite, l’attention est portée sur les matériaux bio-inspirés superhydrophobes, inspirés par des surfaces naturelles telles que les feuilles de lotus ou les coléoptères du désert, en détaillant leurs mécanismes de mouillage et leurs applications dans la séparation sélective, la protection anticorrosion ou le nettoyage de surface.

Les principales stratégies de fabrication de surfaces superhydrophobes sont ensuite abordées, notamment l’électrofilage, les méthodes assistées par gabarit, le procédé sol-gel et les techniques de séparation de phase (TIPS, NIPS). Une évaluation critique des avantages et des limites de chaque méthode est menée, en mettant en évidence les obstacles à leur mise en œuvre industrielle. Dans ce contexte, la fabrication additive — en particulier la technologie Fused Filament Fabrication (FFF) — émerge comme une alternative prometteuse grâce à sa capacité de production numérique, sa flexibilité structurelle et sa compatibilité avec des polymères biodégradables comme le PLA.

Enfin, ce chapitre positionne la présente recherche dans l’état actuel du domaine, en proposant une comparaison synthétique entre les techniques conventionnelles et l’approche par impression 3D. Il est à noter que le chapitre 3 de cette thèse étant dédié à une revue complète sur les matériaux superhydrophobes imprimés en 3D, les redondances de contenu sont volontairement réduites dans ce chapitre pour éviter toute répétition.

3 Chapitre 3 : Revue sur l'impression 3D de matériaux hydrophobes bio-inspirés : séparation huile-eau, collecte d'eau et autres applications

Ce chapitre est consacré à un article de revue intitulé « *A review on 3D printing of bioinspired hydrophobic materials: oil-water separation, water harvesting, and diverse applications* », publié dans la revue **Advanced Composites and Hybrid Materials**. Cet article présente une synthèse exhaustive complète des avancées récentes dans la conception, la fabrication et les applications des matériaux superhydrophobes réalisés par fabrication additive, notamment par les technologies telles que le FFF (Fused Filament Fabrication), le DIW (Direct Ink Writing) et la stéréolithographie (SLA).

La première partie de la revue résume les modèles classiques de mouillage [106,107] ainsi que des concepts émergents comme le seuil intrinsèque de mouillage. Les stratégies de fabrication sont ensuite classées selon plusieurs approches : conception architecturale des surfaces, modification chimique des matériaux, réglage des paramètres d'impression et traitements post-fabrication. L'article explore également les domaines d'application majeurs de ces matériaux, tels que la séparation huile-eau, la collecte d'eau atmosphérique, la réduction de traînée hydrodynamique et les structures réactives imprimées en 4D.

Ce travail fournit ainsi une base théorique et technique essentielle aux chapitres expérimentaux suivants. D'une part, il met en lumière la diversité et le potentiel de l'impression 3D dans la fabrication de surfaces fonctionnelles superhydrophobes ; d'autre part, il identifie les défis persistants, notamment en matière de contrôle de la précision structurelle, de choix de matériaux et de passage à l'échelle industrielle. Ces observations ont directement orienté la conception des protocoles expérimentaux présentés dans les chapitres 4 et 5.

Enfin, la revue retrace l'origine bio-inspirée de ces matériaux, notamment à travers les structures naturelles observées chez les feuilles de lotus, les coléoptères du désert ou encore les pattes d'insectes aquatiques. Des surfaces hydrophobes innovantes telles que les structures en "crête", les topographies en "batteur à œufs", ou les surfaces hybrides de type coléoptère ont été obtenues grâce à l'impression 3D [101,102]. Malgré leurs nombreux avantages, ces approches présentent également certaines limites, comme la difficulté à imprimer des gradients de mouillabilité ou le nombre restreint de matériaux imprimables.

La Figure 3.1 illustre les quatre domaines d'application principaux identifiés pour les matériaux hydrophobes bio-inspirés obtenus par impression 3D : séparation huile-eau, collecte d'eau, réduction de traînée et actionnement intelligent.

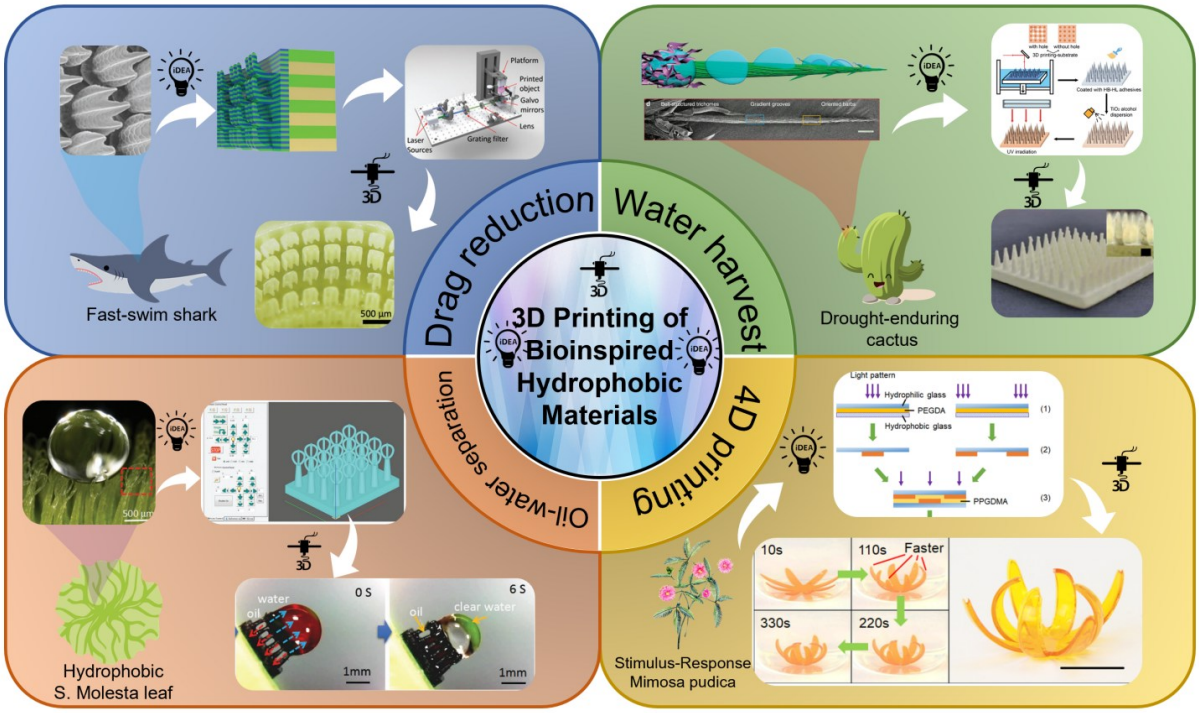

Figure 3.1 Quatre domaines d'application innovants de l'impression 3D de matériaux hydrophobes bio-inspirés.

4 Chapitre 4 : Méthode simplifiée d'impression 3D pour la fabrication d'une membrane superhydrophobe de séparation huile-eau à taille de pores contrôlable

Ce chapitre présente un article de recherche publié intitulé « *Fabrication of Superhydrophobic Poly (lactic acid) Porous Membrane via 3D Printing with Tunable Pore Size for Oil–Water Separation* », paru dans le Journal of **Applied Polymer Science**. Cette étude propose une stratégie simplifiée, sans modélisation préalable, basée sur la technologie Fused Filament Fabrication (FFF), dans laquelle des membranes poreuses en PLA sont fabriquées directement en ajustant le paramètre de densité de remplissage dans le logiciel de tranchage, permettant ainsi de contrôler la taille des pores.

En tant que première étude expérimentale de cette thèse, ce chapitre s'appuie sur les méthodes de fabrication et les axes d'application des matériaux de séparation huile-eau imprimés en 3D

examinés au Chapitre 3, et pose les bases du développement de structures plus complexes et de performances de séparation accrues explorées dans le Chapitre 5.

Face au défi persistant posé par les rejets fréquents d'eaux usées huileuses et les fuites industrielles, la séparation et la purification des mélanges huile/eau sont devenues des éléments essentiels au développement durable [231,232]. Cependant, les méthodes conventionnelles telles que le traitement biologique ou la combustion s'avèrent coûteuses et inefficaces. D'où la nécessité urgente de développer des approches innovantes, performantes et économiquement viables pour répondre aux exigences de l'industrie. Ces deux dernières décennies, des matériaux hydrophobes biomimétiques comme les aérogels [207], mousses [66,94], microsphères [208] et membranes [104] ont été développés pour la séparation huile/eau, offrant des avantages notables en termes de flux, efficacité et consommation d'énergie.

Selon leur mécanisme de séparation, ces matériaux sont généralement divisés en deux types : les adsorbants (aérogels, mousses, microsphères), qui absorbent l'huile dans leur structure interne, et les filtres (membranes), qui laissent passer l'huile sous gravité tout en bloquant l'eau [234]. Si les matériaux adsorbants sont efficaces, leur récupération nécessite des opérations supplémentaires (centrifugation, compression), ce qui réduit leur efficacité globale. Les membranes, quant à elles, sont prometteuses, mais souffrent souvent d'un manque de biodégradabilité, de procédés de fabrication complexes nécessitant des logiciels de modélisation avancés, et de coûts élevés [235].

L'impression 3D, ou fabrication additive (AM), représente une méthode révolutionnaire pour la conception et la réalisation de structures, grâce à sa flexibilité et sa capacité de personnalisation. Elle permet de produire des membranes polymères avec moins de contraintes géométriques [238,239]. Pourtant, peu de travaux ont exploré son potentiel dans la séparation huile/eau. Trois limitations majeures sont identifiées : l'utilisation de matériaux non biodégradables, la nécessité de modèles complexes préalables à l'impression (Figure 4.1), et des procédés de modification superhydrophobe complexes nécessitant plusieurs matières premières.

Parmi les techniques AM, la FFF se distingue par sa simplicité, son faible coût, et sa compatibilité avec les matériaux biosourcés [22]. Le PLA est notamment connu pour sa stabilité, ses bonnes propriétés mécaniques, sa biodégradabilité et son accessibilité économique. D'autres filaments existent, mais souffrent de limitations en termes d'imprimabilité et de disponibilité. Ainsi,

le PLA est actuellement l'option la plus viable pour une fabrication évolutive et efficace de membranes par FFF.

Comparée aux méthodes classiques telles que l'adsorption par éponge ou la flottation, l'utilisation de membranes superhydrophobes permet une filtration sélective plus efficace. De plus, la stratégie proposée ici permet une fabrication évolutive et rentable, les dimensions et tailles de pores étant facilement ajustables sans modélisation complexe. L'usage de PLA biodégradable et l'absence de pollution secondaire renforcent la durabilité du procédé.

Dans cette étude, des membranes en PLA présentant différentes tailles de pores ont été fabriquées par impression 3D FFF, en ajustant la densité de remplissage à l'aide du slicer. Comme le montre la Figure 4.1, cette méthode simplifie la phase de conception de modèle, augmentant ainsi l'efficacité de fabrication. Comparée aux modèles imprimés à partir de modèles CAO, elle offre une meilleure précision dans la taille des pores [204], avec une taille minimale atteinte de 313,02 µm. Le revêtement superhydrophobe, appliqué par pulvérisation simple, atteint un angle de contact allant jusqu'à 154,64° (les matériaux superhydrophobes ont des angles de contact avec l'eau supérieurs à 150°). Cette membrane a permis une séparation de dichlorométhane avec un flux de 81,89 ml cm^{-2} min^{-1} et une efficacité de séparation supérieure à 90 %.

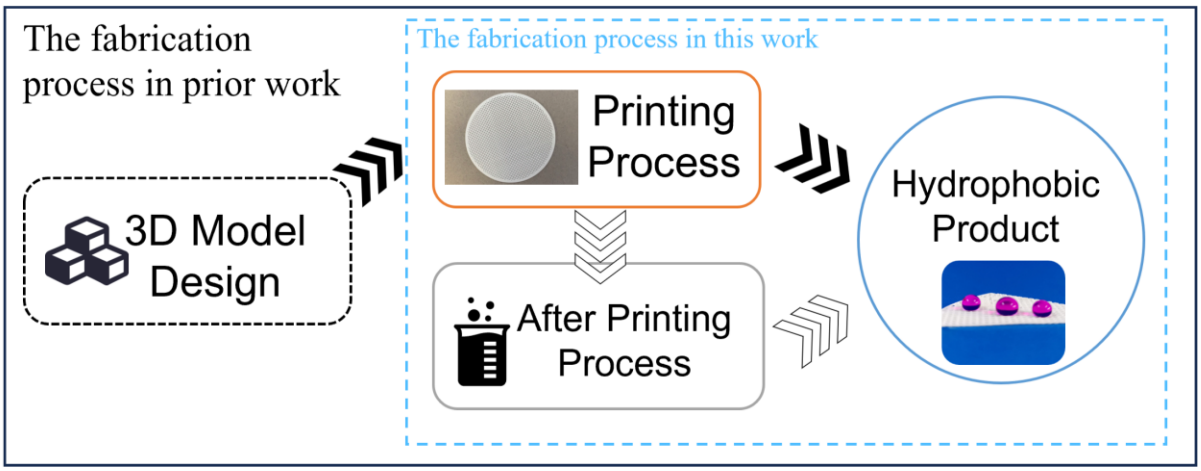

Figure 4.1 Comparaison des procédés de fabrication entre les travaux antérieurs et notre approche.

5 Chapitre 5 : Architectures poreuses superhydrophobes imprimées en 3D pour une séparation continue huile-eau

Atteindre une force d'adhérence adéquate aux interfaces multi-matériaux est toujours un défi dans la fabrication additive par extrusion de matériaux (MEAM), en particulier lorsque les matériaux ont des affinités chimiques très différentes.

Ce chapitre présente un article publié dans **Polymers** intitulé « *Innovative 3D-Printed Superhydrophobic Porous Architectures for Continuous Oil–Water Separation* ». Dans le chapitre précédent, une stratégie simplifiée de fabrication de structures 3D a été introduite. Cette étude va plus loin en proposant la conception d'architectures tridimensionnelles à base de PLA, présentant des pores rhombiques contrôlables, fabriquées par impression 3D de type FFF (Fused Filament Fabrication).

Contrairement aux membranes utilisées en mode discontinu, ce chapitre démontre le potentiel des structures en treillis imprimées en 3D dans des systèmes de séparation continue, pilotés par pompage. Elle met en évidence la possibilité d'intégrer directement ces structures dans des milieux contaminés, comme les rivières, pour collecter les hydrocarbures en continu.

La séparation huile-eau est un défi environnemental majeur. Les méthodes traditionnelles comme la coagulation, la flottation ou la combustion *in situ* souffrent souvent d'un rendement faible et d'une consommation énergétique élevée. Les matériaux superhydrophobes inspirés de la nature — tels que les aérogels, mousses, microbilles ou membranes — présentent une capacité exceptionnelle à repousser l'eau tout en laissant passer l'huile [66]. Toutefois, la plupart des études se concentrent encore sur des membranes 2D, peu adaptées à une séparation continue en conditions réelles.

Dans ce contexte, nous avons conçu une structure maillée tridimensionnelle sous forme de cube imprimée en FFF, pouvant être directement utilisée comme dispositif de récupération d'huile. L'impression 3D permet de moduler avec une grande précision la géométrie et la taille des pores, tout en maintenant un procédé simple, économique et aisément transposable à plus grande échelle. Bien que certaines études aient exploré l'impression de dispositifs 3D pour la séparation huile-eau [202,210,211], elles se limitaient à l'utilisation partielle de la technologie (moule imprimé, structure hybride ou projet conceptuel), sans fabrication directe d'une architecture poreuse fonctionnelle.

Dans notre étude, nous avons optimisé les paramètres clés du procédé FFF (vitesse d'impression, température, multiplicateur d'extrusion) pour obtenir des structures cubiques présentant des pores carrés uniformes avec une précision élevée (erreur < 36,1 µm). La taille des pores obtenue variait de 543,2 µm à 677,3 µm. En affinant les paramètres, nous avons atteint une taille minimale de 186,7 µm. L'optimisation de la hauteur de couche a permis de réduire le temps d'impression de 83,6 %, tout en conservant une hauteur minimale de pore de 287,7 µm.

Pour conférer une superhydrophobicité à ces structures, un revêtement par pulvérisation de nanoparticules de silice (SiO_2) a été appliqué, atteignant un angle de contact de 158,2°. Des tests de pelage ont confirmé la stabilité mécanique du revêtement. Les structures ainsi modifiées ont démontré une excellente efficacité de séparation dans un système continu fonctionnant par pompage, maintenant des performances stables pendant 24 heures avec une efficacité de séparation de 87,2 %.

Il s'agit de la première démonstration de fabrication directe d'architectures poreuses 3D avec des pores uniformes via la technologie FFF. Ces résultats ouvrent de nouvelles perspectives pour la production à grande échelle de matériaux superhydrophobes performants, à faible coût et destinés à la dépollution de l'eau et au traitement des effluents industriels.

6 Chapitre 6 : Conclusions et perspectives

Cette thèse s'est consacrée à la conception et à la fabrication de matériaux poreux superhydrophobes destinés à la séparation huile-eau, en mettant particulièrement l'accent sur une stratégie d'impression 3D contrôlable et évolutive basée sur la technologie Fused Filament Fabrication (FFF). L'objectif était de développer des systèmes de matériaux respectueux de l'environnement, à structure modulable, et adaptés à une production à grande échelle. À travers une série d'études expérimentales, ce travail a proposé de nouvelles méthodes de fabrication, mis en place des protocoles de validation systématiques, et mené des évaluations multidimensionnelles des performances, apportant ainsi des contributions originales au domaine des matériaux fonctionnels poreux et de la fabrication additive.

Parmi les principales contributions scientifiques, Cette thèse a d'abord présenté une revue approfondie des stratégies de fabrication et des fondements théoriques liés aux matériaux superhydrophobes imprimés en 3D. Une approche innovante a été développée pour fabriquer des membranes poreuses 2D en PLA sans modélisation complexe, simplement en ajustant le taux de

remplissage dans le logiciel de tranchage, permettant d'atteindre une taille de pore minimale de 313 µm. Ensuite, une architecture 3D à pores losangiques verticaux a été conçue pour assurer une séparation huile-eau continue, démontrant une haute uniformité dimensionnelle (écart < 36,1 µm) grâce à l'optimisation des paramètres d'impression. Une méthode de modification de surface sans solvant a été mise au point pour obtenir d'obtenir des surfaces superhydrophobes durables (angle de contact > 150°) par pulvérisation de PDMS et de nanoparticules de silice. En parallèle, une technique de séparation de phase induite thermiquement (TIPS) a été explorée, produisant des mousses polymères souples et poreuses adaptées à l'absorption d'huile en mode batch. Cette approche comparative a enrichi la compréhension des liens entre structures et fonctions, et mis en lumière la complémentarité entre impression 3D et techniques classiques dans la conception de matériaux poreux multifonctionnels.

Malgré ces progrès, certaines limites subsistent. La résolution de l'impression FFF reste contrainte par le diamètre de la buse et les propriétés thermiques du PLA, limitant la finesse des structures imprimées. De plus, les expériences ont été menées en conditions de laboratoire, sans validation en environnement marin réel. La stabilité mécanique du revêtement hydrophobe pourrait aussi se dégrader à long terme, soulevant des questions sur sa durabilité environnementale.

Deux perspectives majeures se dégagent de ce travail. D'une part, il serait pertinent d'explorer des alternatives écologiques au traitement de surface, telles que des matériaux hydrophobes biodégradables ou l'emploi de surfaces hydrophiles/oléophobes sous l'eau inspirées des membranes biologiques. D'autre part, les structures poreuses développées pourraient être transposées dans le domaine biomédical, notamment pour des implants personnalisés comme les dispositifs de renforcement du plancher pelvien. L'impression 3D offre en effet des possibilités de géométries sur mesure, l'utilisation de polymères biodégradables et l'intégration de fonctions thérapeutiques (médicaments, antibactériens), ouvrant la voie à de nouvelles générations de dispositifs médicaux personnalisés.

En résumé, ce travail ouvre des perspectives prometteuses pour étendre l'application des matériaux poreux imprimés en 3D, tant dans la dépollution environnementale que dans le domaine biomédical.

English Version

Design and fabrication of superhydrophobic porous structures by 3D printing and phase separation for oil–water separation

Chapter 1: Introduction

1.1 Context of the present study

In recent decades, accidental and operational leaks of petroleum, organic solvents, and other immiscible pollutants have posed serious environmental threats to both aquatic ecosystems and human health [1]. As shown in Figure 1-1a, these pollutants, often originating from oil spills, chemical manufacturing, or industrial wastewater discharge, can persist in the environment, disrupt ecological balance, and cause long-term contamination of water bodies and soils [2]. According to the International Tanker Owners Pollution Federation (ITOPF), over 1,000 large-scale marine oil spills have been reported worldwide since 1970, with catastrophic events such as the Deepwater Horizon spill in 2010 releasing nearly 5 million barrels of crude oil into the Gulf of Mexico [3]. Even more frequently, localized spills from industrial wastewater or inland transportation accidents cause persistent soil and groundwater contamination [4]. These pollution events not only disrupt biodiversity but also lead to long-term ecological degradation, economic losses in fisheries and tourism, and increasing public health concerns.

Traditional oil spill treatment methods such as combustion, skimmers [5] (shown in Figure 1-1b), chemical dispersants [6], and microbial degradation [7] offer certain benefits under specific conditions, but are often limited by low selectivity, secondary pollution, and complex operational requirements [8]. For instance, in-situ burning [9] requires specific weather conditions and can generate toxic by-products; chemical agents may disperse oil but introduce additional ecological hazards [6]; bioremediation [10] is environmentally benign but often too slow for emergency response. These limitations highlight the urgent need for materials and technologies that can enable selective, efficient, and eco-friendly oil–water separation across various environmental scenarios.

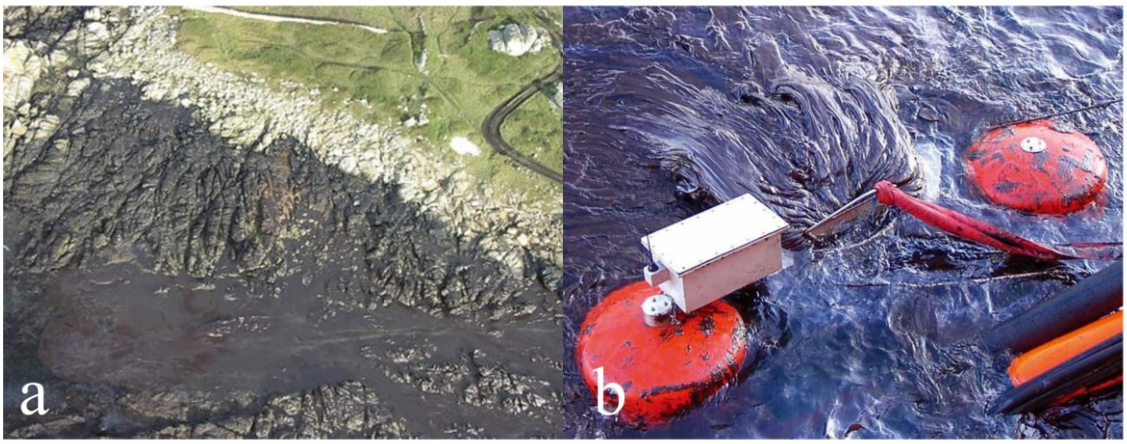

Figure 1.1 ***a*** *Image of spilled oil and* ***b*** *Oil cleaning skimmers. Source: International Tanker Owners Pollution Federation (ITOPF), [1].*

Inspired by natural surfaces such as lotus leaves (Figure 1-2a), water striders (Figure 1-2b), desert beetles, and rose petals, superhydrophobic materials—with water contact angles exceeding 150°—have attracted increasing attention in the field of oil–water separation [11]. These surfaces typically possess hierarchical micro/nanostructures combined with low surface energy coatings, which enable them to effectively repel water while allowing oil to permeate or be absorbed [12]. This passive, selective separation significantly improves efficiency. In recent years, researchers have developed a variety of strategies to construct such surfaces, including electrospinning [13], phase separation [14], sol–gel coating [15], and templating methods [16]. However, these approaches often involve complex fabrication procedures that are not conducive to large-scale production. Moreover, they still face challenges in achieving structural uniformity and offering flexibility for personalized or application-specific design.

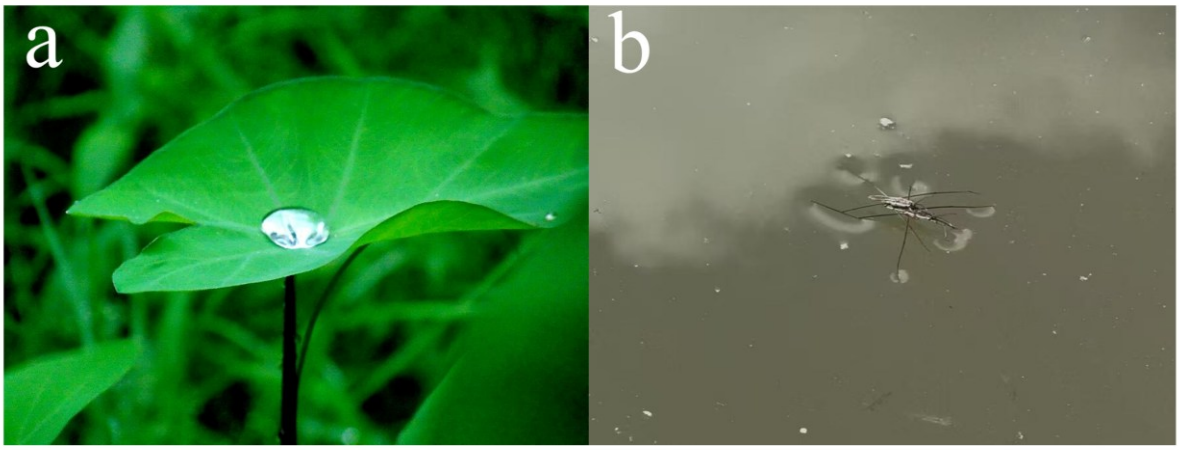

*Figure 1.2 Superhydrophobic behavior on **a** lotus leaves (Image by SureshMukhiya, licensed under CC BY-SA 4.0, via Wikimedia Commons.) and **b** water striders.*

Compared with other fabrication methods, 3D printing offers three main advantages in the development of superhydrophobic materials for oil–water separation. First, 3D printing encompasses a variety of technologies—such as stereolithography (SLA) [17], digital light processing (DLP) [18], and fused filament fabrication (FFF) [19], each compatible with a broad range of materials and adaptable to diverse application scenarios. Second, with the assistance of modeling software, researchers can construct personalized superhydrophobic structures in a highly repeatable and scalable manner. Third, the automated nature of 3D printing significantly reduces labor demands and facilitates industrial scalability. Based on these advantages, 3D printing has become a good tool for developing functional separation materials, including but not limited to oil–water separation.

Among the available 3D printing techniques, FFF has emerged as a promising and versatile method for fabricating superhydrophobic oil-water separation materials. FFF enables the digital construction of porous geometries through the layer-by-layer deposition of thermoplastic filaments, such as polylactic acid (PLA). Compared to other additive manufacturing technologies, FFF offers two major advantages. First, it is the most widely adopted technique, characterized by low equipment costs and user-friendly operation, which makes it highly suitable for large-scale production [20]. Second, it is highly compatible with biodegradable polymers like PLA and typically does not require additional agents such as mold release solvents during the printing process—aligning well with the principles of green manufacturing [21]. However, the main limitation of FFF lies in its relatively low printing resolution [22], which necessitates the fine-

tuning of printing parameters and the optimization of structural design to improve the quality and performance of the final product.

Despite these advantages, significant scientific challenges remain unresolved in the development of superhydrophobic materials for oil–water separation. Existing studies largely provide empirical designs, while the scientific criteria that define the optimal pore geometry, porosity, and multi-scale roughness required for stable Cassie–Baxter wetting are still unclear. Moreover, the relatively low resolution of FFF makes it difficult to precisely control micro- and nano-scale features, creating a gap between structural design and functional performance. These limitations highlight the need for a systematic investigation linking printing parameters, structural morphology, surface modification, and separation behavior. In this context, the present thesis aims to establish a scientific framework for understanding how FFF-printed porous structures, combined with silica-based surface modification, can be tailored to achieve robust superhydrophobicity and efficient oil–water separation.

1.2 Research contents

In this context, the **overall objective** of this thesis is to explore the potential of Fused Filament Fabrication (FFF) in fabrication of superhydrophobic porous materials for efficient oil–water separation. The study focuses on two key aspects: simplifying the fabrication process and developing architected 3D porous structures.

To address this objective in a systematic manner, the research approach is illustrated in Figure 1-3:

We begin with a literature review and theoretical foundation on 3D-printed superhydrophobic materials and their applications (Figure 1-3: Literature Review Based on 3D Printing Hydrophobic Materials and Application). This review covers recent advances in fabrication strategies, wetting models, design principles, and representative applications, with particular attention to oil–water separation mechanisms and hydrophobicity enhancement techniques. The review reveals two major challenges in the current field: (1) fabrication methods are often overly complex and time-consuming; (2) there is a lack of studies that fully leverage 3D printing to create architected porous structures.

According to the discussion above, we first conducted a study on simplifying the fabrication of 2D membrane structures (Figure 1-3: 2D Membrane with Simplified Process). By adjusting the

infill percentage in slicing software, we eliminated the need for pre-modeling. Meanwhile, hydrophobicity was enhanced using silica nanoparticle spray-coating, and the oil–water separation performance was evaluated.

We then developed 3D-printed architectures with vertically oriented porous channels (Figure 1-3: 3D Architectures). These structures were constructed through optimized modeling and printing parameter control. Compared with traditional 2D membranes, these materials are better suited for continuous, pump-driven oil–water separation systems due to their structural uniformity and spatial regularity.

Through this multi-faceted research path, the thesis aims to clarify both the advantages and limitations of 3D printing in constructing functional superhydrophobic separation systems, and to contribute foundational knowledge for the future development of customizable, scalable oil–water separation platforms.

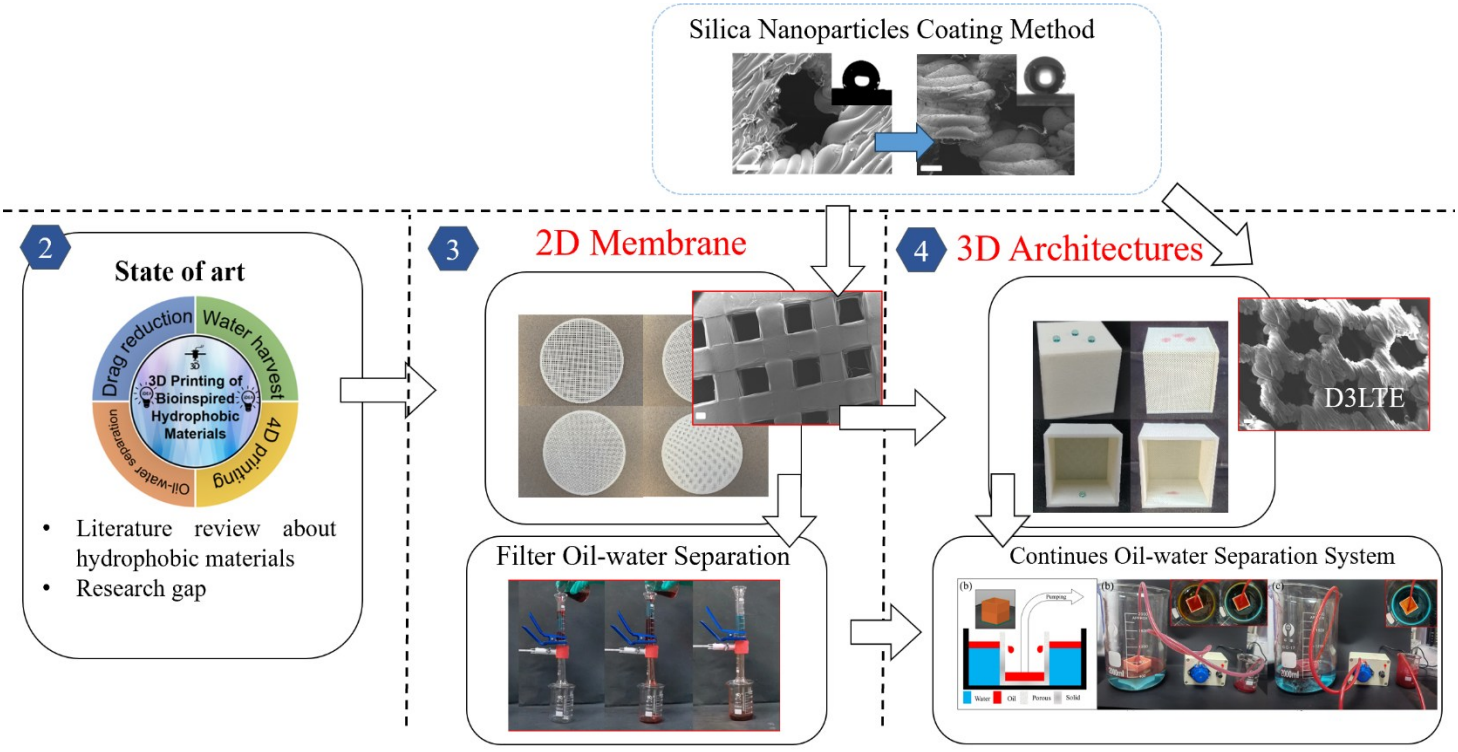

Figure 1.3 Schematic overview of the research framework. SEM images include original scale bars (200 μm).

1.3 Structure of the thesis

This thesis is structured in seven chapters, and the content of each chapter is briefly introduced as follows:

- **Chapter 1** This chapter presents the research background and motivation. Based on the identified scientific challenges, the research objectives are defined, and the overall framework of the thesis is introduced.
- **Chapter 2** studies the state of the art. This chapter introduces oil–water separation as a pressing global challenge and analyzes the limitations of conventional separation methods. It then discusses the development of superhydrophobic materials as a more efficient alternative, along with their various fabrication strategies. Finally, the advantages of 3D printing over traditional methods are assessed, leading to the identification of the research gap and the formulation of this thesis' objectives.
- **Chapter 3** This chapter includes a published review article entitled "A review on 3D printing of bioinspired hydrophobic materials: oil–water separation, water harvesting, and diverse applications", which provides the theoretical foundation and application summary relevant to this thesis.
- **Chapter 4** This chapter presents the design and fabrication of two-dimensional porous membranes using polylactic acid (PLA) via fused filament fabrication (FFF). A simplified slicing strategy was adopted by tuning infill parameters, eliminating the need for detailed modeling. Post-treatment with silica-based coatings was applied to enhance surface hydrophobicity, and the resulting membranes were evaluated for their oil–water separation performance.
- **Chapter 5** This chapter focuses on the development of three-dimensional porous architectures. These structures were digitally modeled and fabricated using FFF, with particular attention paid to infill pattern design and mechanical robustness. The fabricated samples were integrated into a continuous-flow system and tested for dynamic oil–water separation, demonstrating the benefits of spatial control and structural tunability.
- **Chapter 7** presents the conclusion and perspectives of the thesis.

This thesis has been financially supported by Chinese Scholarship Council (CSC) and the regional Council "Région Lorraine". The experiment of this work is support by the Équipe de

Recherche sur les Processus Innovatifs -ERPI- (Research Team in Innovative Process) with its research platform Lorraine Fab Living Lab® and National Engineering Research Center (NERC) for Advanced Polymer Processing Technology of Zhengzhou University.

Chapter 2: State of the art on oil–water separation techniques

2.1 Introduction

This chapter provides a systematic review of the theoretical foundations and technological advancements in superhydrophobic porous materials for oil–water separation. It begins by highlighting the environmental risks associated with crude oil and organic solvent spills. Then, conventional oil–water separation methods and their inherent limitations are examined, followed by the introduction of surface functionalization as a promising alternative. Emphasis is placed on bio-inspired superhydrophobic materials developed in recent years, inspired by natural surfaces such as lotus leaves and desert beetles. Their underlying wetting mechanisms and practical applications in liquid manipulation, anti-corrosion, and oil–water separation are discussed. Several representative fabrication strategies are analyzed, including electrospinning, templating, and thermally induced phase separation (TIPS). Among these, additive manufacturing—especially fused filament fabrication (FFF)—has gained increasing attention due to its industrial scalability, structural tunability, and environmental sustainability. Finally, this chapter outlines the positioning of the current research, which includes a comparative evaluation between FFF and other fabrication techniques.

Note: Since Chapter 3 comprises a dedicated review article on 3D-printed superhydrophobic materials, overlapping content will be streamlined in the present chapter to avoid redundancy.

2.2 Environmental Challenges of Oil and Organic Solvent Spills

Crude oil and organic solvent spills represent a persistent and widespread threat to aquatic ecosystems and terrestrial environments. These pollutants may originate from offshore oil drilling, marine transportation, industrial discharge, and pipeline ruptures. According to statistics from the ITOPF, hundreds of oil spill incidents have occurred globally each year over the past decades, leading to significant ecological and economic consequences [3]. Unlike rapidly degradable pollutants, petroleum hydrocarbons and many organic solvents are hydrophobic and chemically stable, allowing them to persist in the environment for months or even years [23].

The environmental impact of such contamination is multifaceted. Oil films reduce light penetration and oxygen exchange at the water surface, leading to the suffocation of aquatic

organisms. Aromatic hydrocarbons and other toxic constituents of crude oil exhibit carcinogenic, teratogenic, and mutagenic effects. Bioaccumulation in the food chain can further threaten human health through contaminated seafood [24]. In addition to ecological damage, the economic burden of oil spills is substantial, encompassing costs associated with remediation, loss of fisheries, and disruption of tourism and coastal industries.

Numerous high-profile oil spill disasters have illustrated the severity of the issue. For instance, the Deepwater Horizon spill in the Gulf of Mexico in 2010 released over 4 million barrels of oil into the ocean, affecting thousands of kilometers of coastline and countless marine species [3]. Similarly, frequent small- and medium-scale accidents in industrial or harbor zones are often less visible but contribute significantly to cumulative environmental damage [25]. The management of emulsified oil–water mixtures or dissolved organic contaminants poses additional challenges for conventional treatment systems.

These facts underscore the urgent need for the development of more efficient, selective, and sustainable technologies for oil–water separation. The following section will present a classification of conventional treatment approaches and critically analyze their inherent limitations.

2.3 Conventional Oil–Water Separation Techniques and Their Limitations

2.3.1 Overview of Conventional Techniques

In response to oil spills and industrial oily wastewater, a variety of conventional separation techniques have been developed and implemented over the past decades. This section provides an overview of the major categories of traditional oil–water separation methods, analyzes their working principles. Gravity separation employs the density difference between oil and water to allow phase separation over time [26]. This technique is simple but limited to large oil droplets and requires extended settling periods. Skimmers and booms are often deployed in open-water spill scenarios. While they are useful for immediate containment and recovery, their efficiency declines in turbulent or emulsified conditions [27]. Chemical dispersants act by reducing interfacial tension to promote the formation of fine oil droplets [28]. However, their application can introduce toxicity to marine ecosystems and is increasingly restricted by environmental regulations. In situ burning offers rapid reduction of surface oil volume through combustion. Despite its high throughput, it poses fire risks and generates toxic fumes and soot [29].

Bioremediation uses microbial metabolism to degrade hydrocarbons [30]. Figure 2-1 illustrates the principle of bioremediation, where microorganisms degrade environmental contaminants—such as petroleum hydrocarbons—into harmless byproducts like carbon dioxide and water [31]. This process, which depends on the presence of oxygen and nutrients, plays a critical role in ecological recovery after oil spills. It is environmentally benign but generally slow and highly sensitive to temperature, oxygen levels, and nutrient availability.

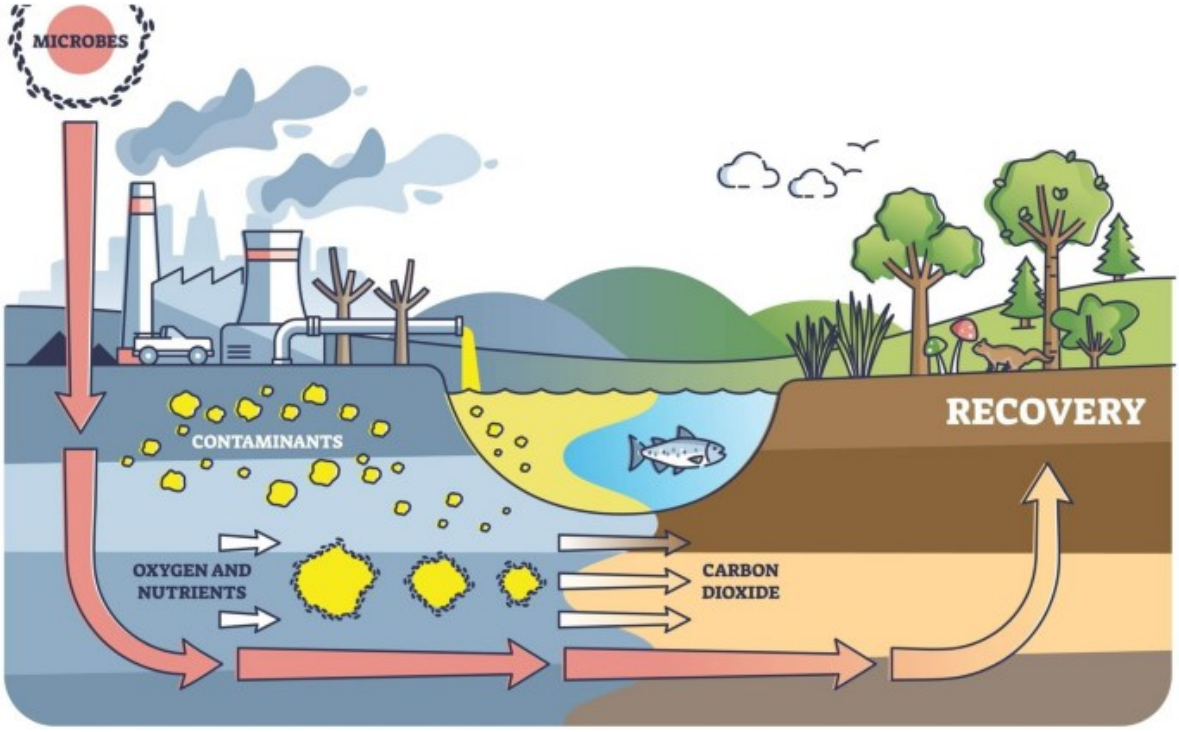

Figure 2.1 Schematic illustration of bioremediation process [31].

2.3.2 Mechanisms and Challenges

Each of the techniques mentioned has inherent limitations that restrict its widespread or long-term application:

- **Low selectivity:** Most physical and chemical methods lack molecular-level selectivity, making them less effective for emulsified oils or low-concentration pollutants.
- **Limited reusability and scalability:** Materials like absorbents or dispersants are often single-use and generate secondary waste, increasing operational cost and ecological burden.
- **Poor adaptability to continuous flow:** Many traditional methods are batch-based and unsuitable for dynamic or continuous industrial effluent treatment.

- **Environmental risk:** In situ burning and chemical agents may introduce new pollutants or hazardous byproducts.

These challenges underscore the urgent need for alternative strategies that are efficient, selective, reusable, and environmentally friendly. Beyond these qualitative considerations, several quantitative indicators further highlight the limitations of conventional techniques. For gravity separators and skimmers, the characteristic residence time typically ranges from several hours to days before acceptable phase separation is achieved, especially when small droplets or emulsions are present [32]. For absorbent-based approaches, the oil uptake capacity is often on the order of 5–30 g of oil per gram of sorbent, but the materials are generally single-use, leading to a high material consumption per unit mass of recovered oil [33]. These quantitative benchmarks further support the need for new separation materials that can combine high selectivity, reusability, and energy efficiency under practical operating conditions.

2.4 Superhydrophobic Materials for Selective Oil–Water Separation

In recent years, bioinspired superhydrophobic materials—drawing inspiration from natural surfaces such as lotus leaves, water striders, and desert beetles—have garnered increasing attention for oil–water separation. These materials typically combine hierarchical micro/nanostructures with low-surface-energy modifications, enabling selective repulsion of water and absorption of oil. This section provides a comprehensive overview of the fundamental principles, fabrication strategies, and performance advantages of superhydrophobic materials, as well as their challenges in practical applications.

2.4.1 Principles of Superhydrophobicity

Superhydrophobicity refers to the extreme water repellence observed on surfaces with a water contact angle (WCA) exceeding 150° and a low sliding angle (<10°) [34]. This phenomenon has been widely studied due to its occurrence in nature—such as lotus leaves and insect wings—and its promising applications in self-cleaning [35], anti-fouling [36], and selective separation systems [12].

Theoretical models explaining surface wettability include:

- **Young's equation,** which describes the equilibrium contact angle on an ideal smooth surface [37].

- **Wenzel's model,** which accounts for the effect of surface roughness assuming complete wetting of the surface features [38].
- **Cassie–Baxter's model,** which introduces a composite interface where liquid partially rests on solid and entrapped air, enhancing hydrophobicity [39].

In recent years, the intrinsic wetting threshold theory has been proposed to further quantify the relationship between surface energy and wetting behavior [40]. This concept suggests that selective liquid transport can be achieved when the surface energy of a material lies between the intrinsic thresholds of two immiscible liquids, such as oil and water. These theoretical frameworks lay the foundation for the design of superhydrophobic surfaces, particularly in the context of oil–water separation. The combination of low surface energy and hierarchical micro/nanostructures is critical for achieving selective permeability and durability.

Note: A detailed discussion of wetting mechanisms, surface energy modulation, and classic wetting models (Young, Wenzel, Cassie–Baxter) is presented in Section 3.3. Readers are referred to that section for in-depth theoretical derivations and schematic illustrations.

2.4.2 Mechanisms of Selective Oil–Water Separation

Superhydrophobic materials used for oil–water separation rely on selective wetting properties, which are governed by a combination of surface energy and surface topography [41]. These materials can either repel water and absorb oil (superhydrophobic/superoleophilic), depending on the designed interfacial interactions. The core mechanism relies on tuning the surface to favor the transport of one liquid while repelling the other. According to the intrinsic wetting threshold theory, a material with surface energy between the intrinsic thresholds of water and oil can selectively allow oil to penetrate while excluding water. For example, a surface with an apparent water contact angle greater than 150° and low adhesion enables gravity-driven oil permeation while blocking water.

In porous membranes or lattice structures, capillary pressure also plays an essential role. Based on the Laplace equation, we know that capillary force is controlled by both surface tension and contact angle [42]. When the contact angle exceeds 90°, the capillary pressure acts as a barrier preventing liquid infiltration into the pores. Moreover, pore diameter significantly influences the magnitude of this force.

In practice, such selective mechanisms are combined with gravity filtration, pump-driven flow, or continuous separation systems to achieve scalable and environmentally friendly oil–water treatment. By fine-tuning pore geometry and surface modifications, materials can be customized for targeted separation performance.

Note: The theoretical basis and experimental validation of capillary pressure and intrusion pressure will be discussed in detail in Section 4.4.1. Here, only a simplified overview is provided.

2.4.3 Fabrication of Superhydrophobic Materials

To achieve superhydrophobicity, surface structures must combine low surface energy with hierarchical micro/nano-scale roughness. Over the past decades, various fabrication techniques have been developed to construct such surfaces. Each approach has distinct advantages depending on the target substrate, desired porosity, and scalability. In this section, four widely reported fabrication methods will be discussed.

2.4.3.1 Electrospinning

Electrospinning is a widely applied technique for producing micro- and nanofibrous membranes. It relies on the use of a high-voltage electric field to stretch a polymer solution or melt into continuous fibers [43]. The resulting fibrous membranes typically possess high surface area, interconnected porosity, and hierarchical architecture, offering a robust structural platform for multifunctional separation materials. This technique has shown broad applicability in oil–water separation [44], gas filtration [45], and sensing applications [46].

Tai et al. developed a carbon–silica composite nanofibrous membrane via electrospinning a polyacrylonitrile (PAN) and tetraethyl orthosilicate (TEOS) precursor, followed by stabilization and carbonization [47]. The resulting membrane exhibited high flexibility, thermal and chemical resistance, and superhydrophobic/superoleophilic properties after silicone oil coating. Figure 2-2a illustrates the fabrication process, where TEOS undergoes in-situ hydrolysis and forms a silica network embedded within the PAN matrix. Upon high-temperature treatment under inert atmosphere, the PAN is converted into carbon, producing an interpenetrating carbon–silica framework. This structure contributes to the membrane's enhanced mechanical durability and enables ultrafast gravity-driven separation of oil–water mixtures without external pressure. Sun et al. fabricated a flexible superhydrophobic carbon nanofiber membrane via electrospinning followed by fluorination treatment [48]. In their design, zinc acetate was introduced as a pore-

forming agent during the carbonization process, which significantly enhanced the porosity and flexibility of the resulting fibers. The membrane achieved a water contact angle (WCA) of 155.9°, demonstrating excellent superhydrophobicity. As shown in Figure 2-2b, the membrane could be applied for separation of oil-water mixture under gravity-driven operation. Luo et al. developed Janus composite porous membranes via electrospinning followed by plasma treatment and selective surface modification [49]. The resulting membrane exhibits asymmetric wettability—one side being superhydrophobic and the other superhydrophilic—which enables directional fluid transport and effective oil–water separation. This configuration acts as a liquid diode, allowing unidirectional penetration of oil or water while blocking the reverse flow. The Janus membrane achieved a separation efficiency exceeding 99% and demonstrated significantly higher flux than conventional homogeneous membranes. This work highlights the potential of integrating electrospinning with post-treatment techniques to construct smart, directional separation systems.

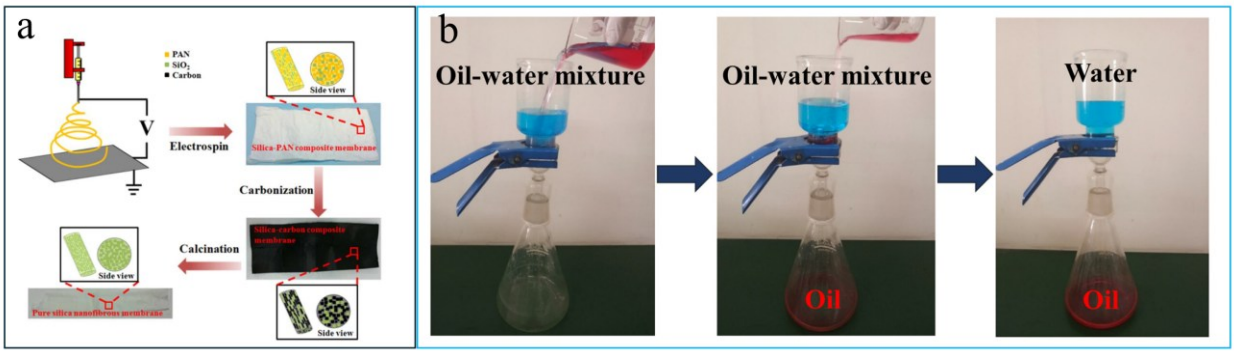

Figure 2.2 ***a*** *Fabrication process of Silica-PAN membrane [47].* ***b*** *Oil-water separation process of PSF based membrane [48].*

Electrospinning offers several advantages in the fabrication of superhydrophobic membranes, such as high specific surface area, tunable porosity, and excellent flexibility. It is compatible with a wide range of polymers and allows for easy surface modification, which makes it highly adaptable for oil–water separation applications. Moreover, electrospinning membranes can be designed with hierarchical structures that promote selective wettability and enhance separation efficiency [50]. Despite its benefits, electrospinning also faces several challenges. Many formulations rely heavily on organic solvents, raising environmental and safety concerns. Additionally, conventional electrospinning systems typically suffer from low production throughput, and the fabrication process tends to be complex, making scale-up difficult. Electrospinning is also sensitive to environmental parameters such as humidity and temperature,

which may affect the consistency and quality of the resulting membranes [51]. Lastly, the mechanical strength and long-term operational stability of electrospinning membranes still require optimization to meet practical application demands [52].

In conclusion, electrospinning is an effective and versatile method for producing functional membranes, but further advancements are needed to improve its scalability and durability for real-world deployment.

2.4.3.2 Template-Assisted Method

Template-assisted Method is a widely adopted strategy for constructing porous superhydrophobic materials, relying on the use of removable templates to guide the formation of micro- and nanostructures. This method allows for fine control over pore size, porosity, and surface morphology, which are critical for achieving selective wettability and efficient oil–water separation. Hard templates such as sugar crystals [53] and salt particles [54] are used. After infiltration of a hydrophobic precursor (e.g., Polydimethylsiloxane [PDMS] or polyurethane), the template is removed by dissolution or thermal treatment, leaving behind a porous structure. However, due to the inherently low surface energy of PDMS, water or other solvents have difficulty penetrating its matrix, making the hard template difficult to remove and often resulting in incomplete removal [55].

To address these limitations, Turco et al. proposed a soft-template method using a water-in-silicone emulsion system to fabricate porous PDMS sponges for oil–water separation [56]. As illustrated in Figure 2-3a, PDMS prepolymer is mixed with hexane and emulsified with water, followed by thermal curing at 120 °C. During curing, water droplets expand and burst, forming interconnected pores. As shown in Figure 2-3b and c, a unique porous structure was formed after water evaporation. The resulting sponge exhibited a high porosity (~93%), excellent oil absorption (up to 32.3 g/g for dichloromethane), mechanical resilience under compression, and strong reusability over 300 cycles. Zhao et al. prepared a magnetic-responsive superhydrophobic porous $NiFe_2O_4$ based composite using a high internal phase Pickering emulsion (HIPPE) templating approach [57]. As shown in Figure 2-3d, the emulsion was stabilized by lipophilic surfactant Span 80 and $NiFe_2O_4$ nanoparticles, allowing the internal water phase to exceed 98% by volume. After polymerization and evaporation of the aqueous phase, a 3D interconnected porous network was formed. Compared with traditional soft templates like sugar or salts, the aqueous phase in HIPPEs does not constitute part of the material framework, but serves as a sacrificial pore-forming

component, functioning as a non-materialized soft template. Furthermore, the incorporation of $NiFe_2O_4$ nanoparticles enabled magnetic responsiveness, facilitating external magnetic recycling. The resulting material exhibited high oil adsorption capacity (up to 84.2 $g \cdot g^{-1}$) and excellent reusability, making it promising for efficient oil/water separation in environmental applications.

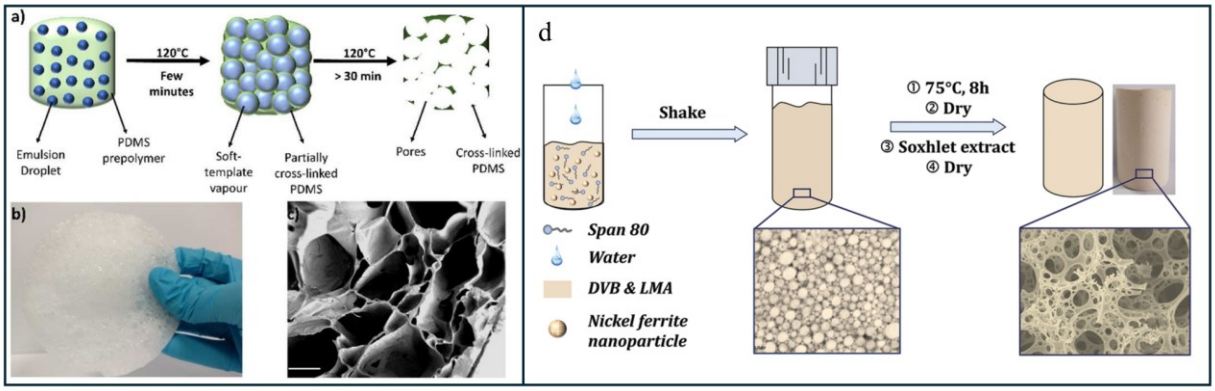

Figure 2.3 ***a*** *Schematic illustration of the preparation of the PDMS sponge.* ***b*** *photograph of the freshly prepared PDMS sponge.* ***c*** *SEM image of a sponge portion (scale bar=500μm) [56].* ***d*** *Schematic diagram for the preparation of $NiFe_2O_4$ based porous composites [57].*

Template-based fabrication enables the design of hierarchical porous structures that significantly enhance capillary forces, directional liquid transport, and selective permeation—key factors in high-efficiency oil–water separation. Recently developed soft-templating method offers scalable alternatives to traditional hard-template strategies. However, the template method still faces notable challenges. The multistep processing, time-consuming drying and curing procedures, and frequent reliance on volatile or toxic solvents limit the method's suitability for large-scale industrial production. Therefore, although template-based methods are valuable for laboratory-scale innovation, their complexity and limited scalability remain major hurdles to commercial implementation.

2.4.3.3 Sol-Gel Process Method

The sol–gel process is a widely utilized bottom-up fabrication strategy for constructing superhydrophobic surfaces with controlled micro- and nanostructures. It typically involves the hydrolysis and condensation of metal alkoxides or organosilane precursors—such as tetraethyl orthosilicate (TEOS) [58] or methyltrimethoxysilane (MTMS) [59] in the presence of solvents and catalysts. The resulting colloidal "sol" undergoes gradual transformation into a "gel" network, which can be deposited onto various substrates via dip-coating, spin-coating, spray-coating, or

casting techniques [60]. Upon drying and thermal curing, a rough, often porous silica-based layer is formed, providing the hierarchical surface morphology required for superhydrophobicity. To further reduce surface energy for improvement of hydrophobicity, the gel-derived surface is typically functionalized with low-energy compounds such as fluorinated silanes or alkyl silanes [61].

The sol–gel approach offers several advantages, including facile processing, low-temperature operation, and strong compatibility with a wide range of substrates (glass, polymers, metals, fabrics). It is particularly suited for producing transparent or flexible superhydrophobic coatings. Moreover, it allows tunable control over porosity, surface roughness, and chemical composition, making it attractive for oil–water separation, self-cleaning, anti-fogging, and corrosion-resistant applications [62].

As shown in Figure 2-4a, Xie et al. developed a sustainable superhydrophobic cellulose membrane (SOCM) via a one-step sol-gel process by immersing filter paper into a TEOS based ethanol solution in the presence of ammonia [63]. The resulting membrane exhibited a hierarchical micro/nanostructure, superhydrophobicity (WCA ~161.8°), and excellent oil/water separation efficiency (>98%) even under harsh chemical environments. Notably, SOCM maintained its performance after multiple cycles and showed good mechanical durability under tape-peeling and scratch-resistance tests. Wen et al. developed a simple and economical modifier-free sol–gel method to fabricate superhydrophobic–superoleophilic cotton fiber@SiO_2 fabrics for oil–water separation [15]. As shown in Figure 2-4b, the method utilizes only tetraethyl orthosilicate (TEOS), ethanol, and aqueous ammonia as the catalyst, avoiding the need for expensive fluoroalkylsilane or siloxane modifiers typically required in conventional sol–gel processes. By adjusting the concentration of ammonia water, the surface wettability of the resulting fabrics can be precisely tuned. Specifically, at an ammonia concentration of 3–6%, the prepared fabrics exhibit superhydrophobicity with a water contact angle of approximately 156° and complete oil wettability (0°). As illustrated in Figure 2-4b, the resulting superhydrophobic membranes demonstrate an oil–water separation efficiency up to 98%, offering a sustainable alternative to conventional coating methods. This work highlights the potential of sol–gel chemistry for scalable and environmentally friendly fabrication of functional surfaces without relying on organic surface modifiers.

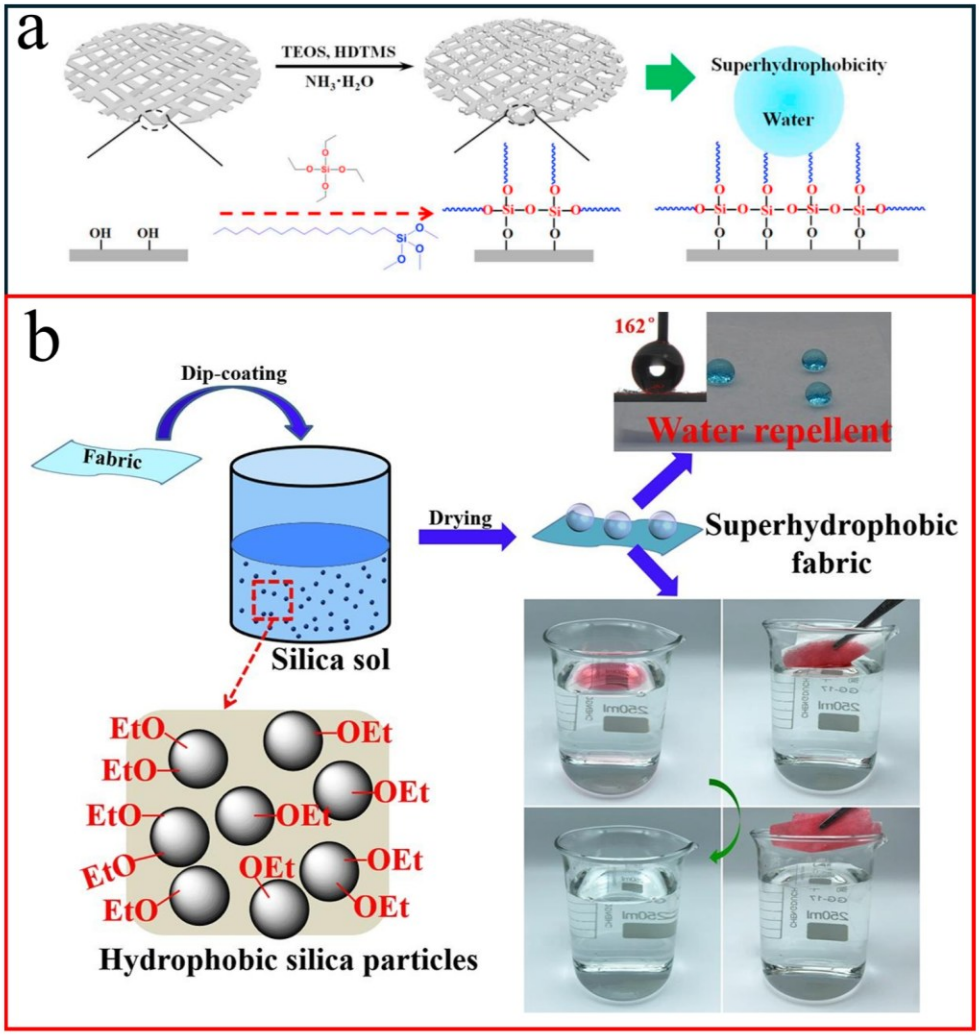

Figure 2.4 ***a*** *Schematic illustration of the preparation of SOCM [63].* ***b*** *Schematic diagram for the preparation of cotton based hydrophobic fabric and its oil-water separation process.*

However, several limitations should be noted. The sol–gel process often requires lengthy gelation and aging times. The resulting coatings may exhibit mechanical fragility or poor abrasion resistance. In addition, the process frequently involves the use of volatile organic solvents and acidic or basic catalysts, posing safety and environmental concerns. These issues limit the scalability of the sol–gel technique for large-scale or industrial applications, despite its versatility in laboratory research.

2.4.3.4 Phase Separation Techniques

Phase separation techniques have emerged as powerful bottom-up strategies for fabricating porous superhydrophobic membranes, relying on the spontaneous segregation of polymer-rich and

polymer-poor phases under controlled thermodynamic conditions [64]. These methods enable the generation of hierarchical pore structures within polymeric matrices, which are critical for achieving selective wettability, capillary-driven transport, and efficient oil–water separation. The most employed phase separation methods include thermally induced phase separation (TIPS) and non-solvent induced phase separation (NIPS).

In TIPS, a polymer is first dissolved in a high-boiling-point solvent at elevated temperatures. Upon cooling, phase separation occurs as the system enters a metastable region, leading to the formation of a polymer-rich solid skeleton and solvent-rich domains that are later removed during extraction or drying. Zuo et al. proposed a novel strategy to fine-tune the morphology and separation performance of TIPS-fabricated Polyvinylidene fluoride (PVDF) membranes by using saline water with different NaCl concentrations as the quenching bath [65]. The resulting membranes exhibited continuous fibrillar morphology and tunable surface roughness. As shown in Figure 2-5a, these membranes demonstrated over 95% oil rejection for surfactant-free emulsions and excellent reusability across multiple filtration–regeneration cycles. This work underscores the feasibility of using environmentally benign salt-induced thermal tuning to enhance the performance of TIPS membranes for oil–water separation applications. However, in the study by Zuo et al. using saline water to modulate the cooling rate during TIPS, the water contact angle of the resulting PVDF membranes did not meet the superhydrophobic standard, although enhanced permeability was achieved. In our previous work, we addressed this limitation by proposing a water-assisted TIPS strategy to fabricate pure PLA foam with hierarchical micro-/nanostructures [66]. As shown in Figure 2-5b, the sublimation of water ice crystals created additional pores, thereby increasing the surface roughness of the sample. The resulting PLA foams exhibited a water contact angle of 151°, qualifying as superhydrophobic, and demonstrated excellent oil adsorption capacity (up to 31.5 g/g) and long-term durability, maintaining a separation efficiency of 98% for over 15 hours in continuous pumping tests. This green and scalable method shows great potential for the practical remediation of large-scale oil pollution.

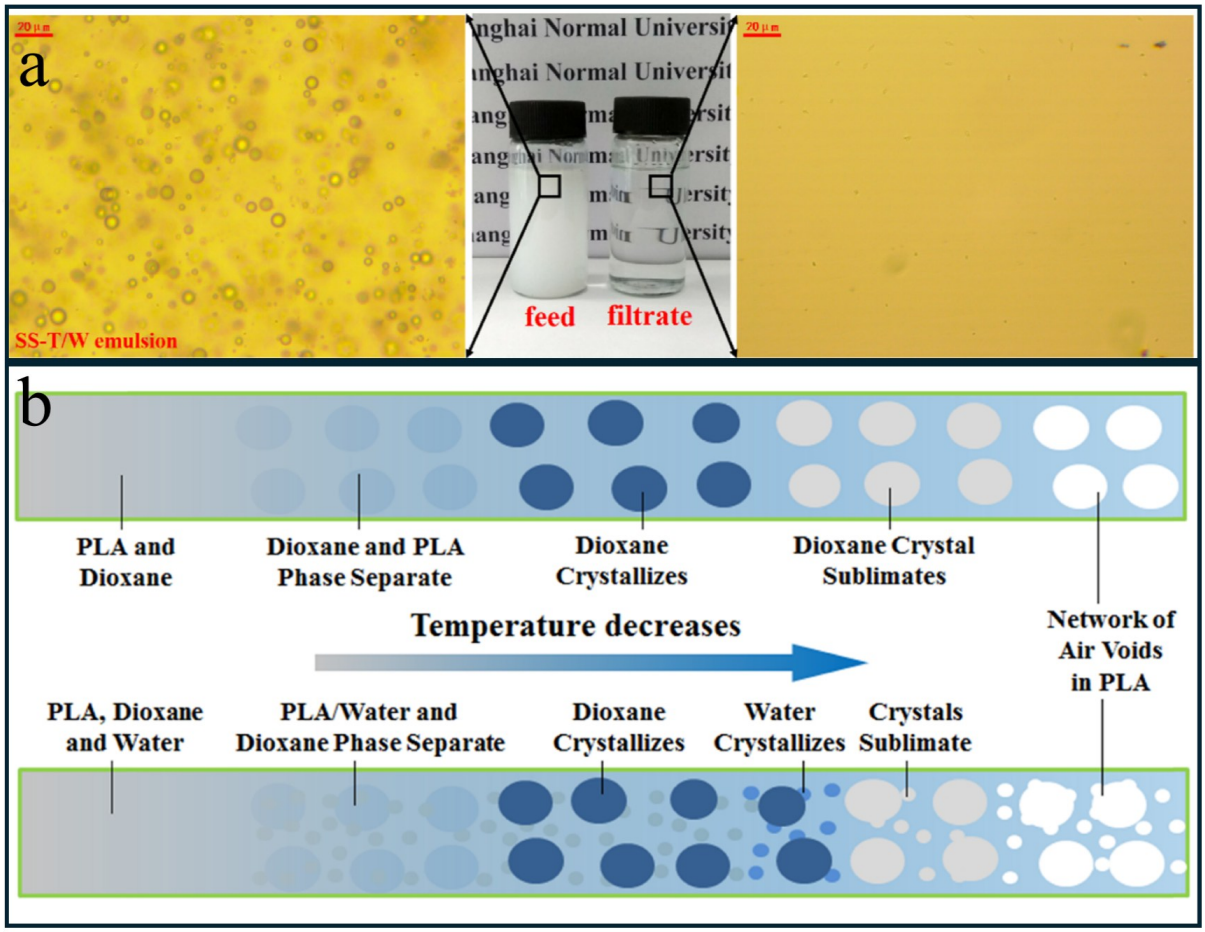

Figure 2.5 ***a*** *The feed and filtrate of PVDF based membrane and the optical microscopy images [65].* ***b*** *Schematic of the phase inversion process [66].*

NIPS involves the immersion of a polymer solution into a non-solvent (typically water), triggering phase separation through solvent exchange [67]. This method allows for greater control over membrane thickness and pore gradients but often requires precise tuning of solvent/non-solvent ratios, polymer concentration, and coagulation bath conditions. Hai et al. reported the fabrication of an intrinsically superhydrophobic and superoleophilic PVDF membrane using the nonsolvent-induced phase separation (NIPS) method [68]. The unique feature of the prepared membrane was its uniform wettability across the entire membrane structure, not just the surface, which was attributed to its interconnected fibrous morphology. The membrane demonstrated exceptional water repellency and oil affinity, achieving an oil flux of 8800 $L \cdot m^{-2} \cdot h^{-1}$ under ambient conditions for the separation of water-in-oil emulsions. The membrane also showed stable performance in both acidic and basic environments, along with enhanced fouling resistance when compared to conventional PVDF membranes. This work highlights the potential of using a simple

one-step NIPS method to fabricate high-performance membranes for oil–water emulsion separation without the need for surface modification or chemical treatment.

Despite their versatility, phase separation methods face challenges such as solvent toxicity, post-processing complexity, and environmental impact. Moreover, controlling long-range pore uniformity and ensuring mechanical robustness remain active areas of optimization.

2.5 Summary and Comparative Analysis

The fabrication strategies discussed in this chapter—electrospinning, template-assisted methods, sol–gel processing, and phase separation techniques—have demonstrated effectiveness in constructing superhydrophobic surfaces. However, they still face practical limitations that hinder their broad implementation in scalable oil–water separation systems.

Electrospinning enables the creation of highly porous and tunable fibrous networks, but it suffers from low throughput, the use of complex solvent systems, and limited structural flexibility. Template-assisted methods can generate well-defined pore structures, but they often involve multi-step procedures, sacrificial templates, and difficulties in template removal, particularly when hydrophobic matrices such as PDMS are used. The sol–gel approach offers chemical versatility and effective surface roughening, yet it commonly depends on environmentally unfriendly modifiers and exhibits poor mechanical durability. Phase separation techniques (e.g., TIPS and NIPS) are widely adopted in membrane science due to their tunability and polymer compatibility. Nonetheless, they lack geometrical design freedom, often require post-modification steps, and involve issues such as solvent toxicity and complex waste management. Additionally, these methods typically have stringent environmental or equipment requirements—for instance, electrospinning must be conducted under controlled temperature and humidity, while TIPS processes demand precise thermal regulation. Moreover, the manual nature of these processes limits their automation potential, posing challenges for large-scale or industrialized production.

In this context, additive manufacturing (3D printing) has emerged as a promising alternative. It enables precise control over 3D geometry, porosity, and material distribution in a single digital step. Fused filament fabrication (FFF) is compatible with sustainable and biodegradable polymers such as PLA, and its mechanically controlled operation is well-suited for industrial-scale production. Among the different additive manufacturing techniques, direct ink writing (DIW) has also demonstrated remarkable capabilities for fabricating micro-architectured porous structures.

However, DIW generally requires carefully formulated, high-viscosity inks, sophisticated rheological control, and customized equipment, which currently limits its accessibility and scalability for routine industrial deployment. [69] In contrast, FFF is widely available as a robust, low-cost platform using commercially accessible filaments such as PLA, making it more suitable for the practical, large-scale implementation scenarios targeted in this thesis.

This thesis focuses on harnessing the unique advantages of 3D printing in the fabrication of superhydrophobic porous materials, especially for oil–water separation applications. Chapter 3 presents a comprehensive review on the recent progress in 3D-printed superhydrophobic materials, from fabrication strategies to practical applications. Section 3.6.1 specifically analyzes the oil–water separation performance of membranes fabricated via 3D printing. Based on the analysis, research gaps in current 3D printing approaches are identified, which informs the experimental investigations presented in subsequent chapters.

Table 2-1 presents a comparative analysis of the major fabrication methods discussed above. The assessment criteria—such as porosity control, structural flexibility and industrial readiness—are based on performance indicators reported in representative studies and synthesized from the evaluations in Sections 2.4. It should be emphasized that the qualitative scores (“High”, “Moderate”, “Low”) in Table 2-1 are not arbitrarily assigned but represent a synthesis of trends reported in the literature [70-72] and discussed in Sections 2.4. “Porosity control” reflects the ability of a given method to tune pore size, distribution and connectivity over a relevant range for oil–water separation. “Structural flexibility” refers to the freedom to design different geometries or architectures, which is crucial for adapting the material to specific separation configurations. “Industrial readiness” qualitatively estimates the maturity of the technique in terms of process robustness, throughput, and compatibility with large-scale equipment, while “eco-friendliness” qualitatively integrates the use of toxic solvents, waste management requirements, and the potential for using biodegradable or low-impact materials. A dedicated cost column is not included because economic aspects are partly embedded in “industrial readiness” and “eco-friendliness”, and because reliable, comparable cost data are rarely reported in a consistent way across the surveyed studies. While specific values may vary depending on material and process parameters, the overall trends provide a useful framework to guide the selection of fabrication methods for practical applications.

Table 2-1 Simplified comparison of fabrication methods for superhydrophobic oil-water separation materials.

Method	Porosity Control	Structural Flexibility	Industrial Readiness	Eco-friendliness	Remarks
Electrospinning	High	Low	Low	Low	Solvent-heavy, low throughput
Template-Assisted Method	High	Moderate	Low	Low	Multi-step, template removal is challenging
Sol–Gel Process	Moderate	Low	Moderate	Moderate	Brittle coatings, uses volatile reagents
Phase Separation	High	Moderate	Moderate	Low	Solvent-heavy, limited design freedom
3D Printing	High	Very High	High	Moderate	Digital control, template-free

Chapter 3: A Review on 3D Printing of Bioinspired Hydrophobic Materials: Oil–Water Separation, Water Harvesting, and Diverse Applications

3.1 Introduction to the Chapter

This chapter presents a review article entitled *"A review on 3D printing of bioinspired hydrophobic materials: oil-water separation, water harvesting, and diverse applications"*, published in **Advanced Composites and Hybrid Materials**. The article systematically reviews recent advances in the design, fabrication, and application of superhydrophobic materials enabled by additive manufacturing techniques, especially fused filament fabrication (FFF), direct ink writing (DIW), stereolithography (SLA), and others. To avoid redundancy with Chapter 2, overlapping background content has been shortened or reorganized, while preserving the core analytical framework of the published work.

The review first summarizes classical wetting models (Young, Wenzel, Cassie–Baxter) and emerging concepts such as the intrinsic wetting threshold. It then classifies fabrication strategies for achieving hydrophobicity, including design of surface architecture, material modification, printing parameter control, and post-treatment. The article also explores major application fields such as oil–water separation, water collection, drag reduction, and 4D-printed responsive structures.

This review provides the theoretical foundation and technical background for the experimental chapters that follow. On the one hand, it systematically illustrates the diversity and potential of 3D printing technologies in the fabrication of functional superhydrophobic materials. On the other hand, it highlights existing challenges in structural precision control, material selection, and application scalability. These issues directly motivated the research design and methodological choices presented in Chapters 4 and 5.

3.2 Introduction

'Growing form the mud without being stained, scouring by the water without being demonized.' The wisdom of a Chinese poet a thousand years ago described the special self-cleaning and water-

repellent characteristics of lotus leaves. With support from electron microscope, Barthlott et al discovered the reason for the formation of the special wettability of lotus leaves [73]. The leaves are covered with waxy substances, and it has an intriguing multi-scale microstructure: micro-scale synapses have been observed with nanoscale "villi" structures on the synapses surface. Therefore, the intrinsic chemical properties and special microstructure of the surface which are common in hydrophobic surface discovered in nature considered to be the two domain principles to promote hydrophobicity [74].

In fact, creatures and plants possessing this idiosyncratic wetting phenomenon are not rare in nature, e.g., mosquitoes, roses, water striders, geckos, desert beetles, and so on [75-79]. By mimicking this peculiar structure origin from nature, more and more hydrophobic materials have been reported which are practical for a wide array of applications including anti-corrosion [80,81], anti-icing [82], anti-fogging [83], self-cleaning [84-86], anti-fouling [87], etc. Beetle-like structure, a bionic special design mimicking the creatures living in desert, with distinct mixing property of both hydrophobic and hydrophilic could be applicated in harvesting water in extreme environments and handling the global frequent discharge of water scarcity [88]. Hydrophobic face masks and other wearable protectors with properties of anti-droplets could reduce the spread of the virus [89]. In industrial fields, such as automobiles, building materials, textiles, and electronic devices, the market for hydrophobic coating is rapidly increasing. In summary, the fabrication of new hydrophobic materials remains challenging and would benefit many practical applications.

In order to fabricate hydrophobic materials, increasing methods including electrospinning [90-92], phase separation [66,93,94], template methods [95], extrusion [96,97] and foaming [98] have been developed. However, if consider the most recent major study, the following three problems limit the practical application. Initially, complex and expensive raw materials are not economically competitive. More importantly, complex chemically induced processes consume a lot of time and human resources. Finally, the size and shape of manufactured products cannot be customized. 3D-printing, or named also as additive manufacturing, is a fast-growing technique which could transform a numerical model into an integrated material by deposition raw material layer by layer under the control of precision 3D-printer [99]. Viewed from a social standpoint, 3D-printing technique has participated in a large proportion of industrial production such as automobile manufacturing and pharmaceutics [100], which has a profound impact on the global supply chain. Considering the shortcoming of the traditional fabrication methods mentioned above, 3D-printing

is considered as a relevant candidate for the simple and rapid fabrication of hydrophobic material without expensive equipment or complex raw material. In the past decade, many innovative bioinspired hydrophobic surfaces including ratchetlike surface [101], eggbeater topography [102] and beetle-like hybrid surface [103] have been manufactured by 3D-printing technique. However, compared to traditional methods, 3D printing also has some limitations. For example, it may face challenges in constructing gradient wetting structures, have a limited selection of raw materials suitable for 3D printing, and may not be as efficient for large-scale production.

Therefore, a review of the hydrophobic products fabricated by 3D-printing and their applications is necessary. Here, we will introduce the formation principle of the hydrophobic surface and wettability theory origins from nature. We will also discuss the main advanced technological methods of 3D printing, and the significant methods used to achieve hydrophobicity. Finally, we will introduce the 3D-printing bioinspired materials in the application fields of drag reduction, water harvesting, oil-water separation and actuator, together with the outlook for future development (Figure 3-1).

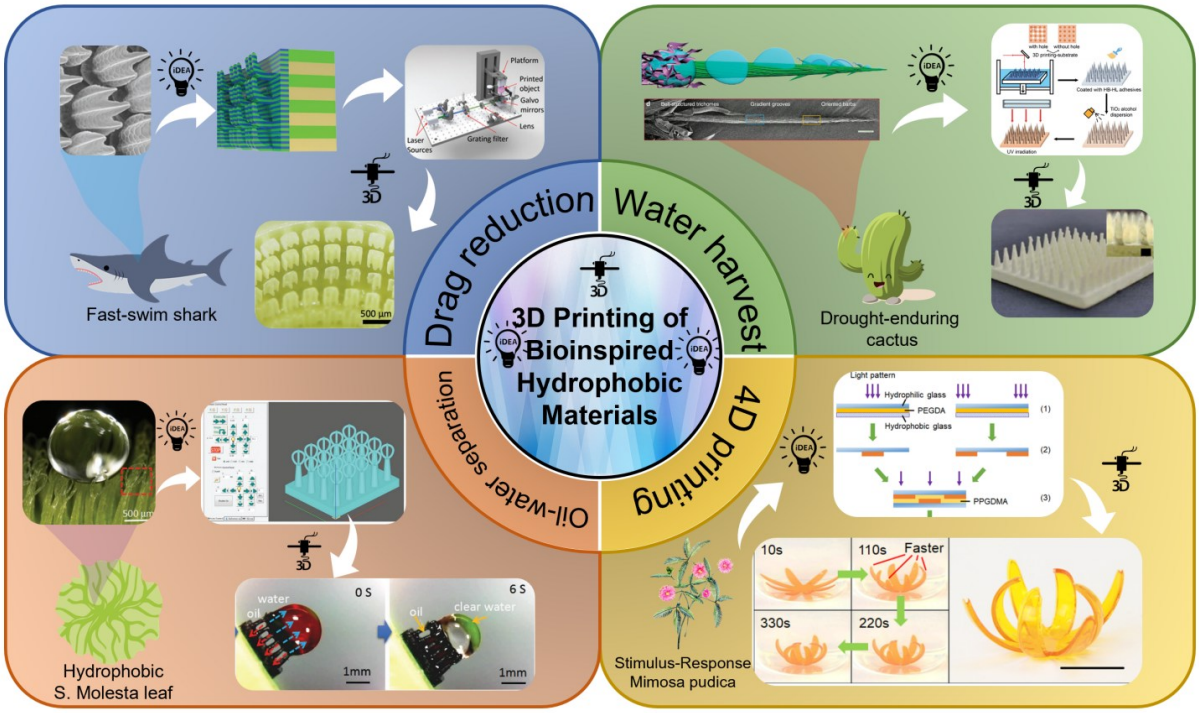

Figure 3.1 Four innovative application fields for 3D-printing of bioinspired hydrophobic materials.

3.3 Theoretical background of wettability

3.3.1 The wettability of the surface

The contact angle (CA), rolling angle, advancing angle and lagging angle of the liquid phase on the solid surface are the key indicators to characterize the wettability of the solid surface. CA can reflect the wettability of a solid surface. As illustrated in Figure 3-2a, at the intersection point of the gas-liquid-solid three-phase position, the angle between the tangent of the gas-liquid-phase contact surface relative to the liquid phase and the boundary line between the solid and liquid phases is CA (θ_0). The rolling angle could be used to measure the adhesion ability of the solid to the liquid phase, which refers to the minimum angle at which the liquid droplets on the solid surface start to roll down as the inclination angle of the solid surface increases. The advancing angle and the lagging angle are the CA at the front and the end in the moving direction of the droplet when it rolls down. The smaller the difference between the two, the lower the adhesion force of the solid surface to the droplet.

The wettability of a solid surface is affected by many factors; the main influencing factors are synergistic action of the microstructure of the surface and the surface energy (SE) [104]. It has been proved by experiments that when a solid surface with a micro-nano composite structure is in contact with a liquid droplet, an air cushion is easily formed in the micro-nano pores, which can support the water droplet, thereby increasing the CA. The higher the SE of the solid surface, the stronger the adsorption force to the liquid, and the smaller the CA is. On the contrary, if the SE is lower, the CA will be larger. When designing and preparing hydrophobic materials, the SE and microstructure of the materials should be properly matched to increase the CA of the materials. According to the CA between the solid surface and the droplet, there are mainly four different types of wetting. When the droplet CA is greater than 150°, it is called superlyophobic; when the droplet CA is greater than 90° and less than 150°, it is called lyophobic; when the droplet CA is less than 90° and greater than 0°, it is called lyophilic; when the droplet CA is less than 30°, it is called superlyophilic.

3.3.2 The theory of hydrophobicity

The Young's equation is the simplest formula for calculating the CA under the condition of solid-liquid contact, that is, the solid surface is ideally smooth and plane, and there is no interaction

between solid and liquid (Figure 3-2a). The CA at this time can be calculated by Young's equation [105]:

$$cos\,\theta_0 = \frac{(\gamma_{SV} - \gamma_{SL})}{\gamma_{LV}} \quad (3-1)$$

The interfacial tension between solid-gas, solid-liquid, and liquid-gas phase in this formula is represented by γ_{SV}, γ_{SL} and γ_{LV}, respectively. This equation is a basic equation of interface chemistry. The CA θ_0 at which a droplet contacts a smooth solid surface under such conditions is often referred to as the intrinsic CA. θ_0 reflects the SE of a smooth solid surface which is an inherent property of the solid surface itself.

However, the surface of the real object has a certain roughness. Wenzel model [106] was constructed based on the condition that water droplets are in contact with a uniform rough solid surface (Figure 3-2b). It is supposed that liquid can completely fill the gaps on the rough solid surface and reach a stable state which could be defined by the following equation:

$$cos\,\theta_w = \frac{r(\gamma_{SV} - \gamma_{LV})}{\gamma_{LV}} = r cos\theta_0 \quad (3-2)$$

where *r* represents the roughness of the solid surface, obtained by dividing the area of the surface that has been wet and the apparent surface area, θ_w refers to the surface CA with a rough structure, and θ_0 refers to the CA with a smooth structured surface calculated by Young equation. Wenzel's model is because the roughness of a solid surface is much smaller than that of a liquid. Owing to the surface roughness is always bigger than 1, it can be concluded that for lyophobic surface (CA>90°), the presence of roughness will make θ_w larger than θ_0; For lyophilic materials (CA < 90°), roughness will make θ_w smaller than θ_0. This conclusion has guiding significance for the experiment.

Cassie and Baxter [107] perfected Wenzel's theory. As shown in Figure 3-2c, they believed that the bottom of the droplet cannot penetrate into the gaps on the solid surface when it contacts the surface with special microstructure contains micro& nano-scale pores, wires or synapse. In case of this, the gas phase will accumulate in these gaps, forming a similar "air cushion" structure. Hence liquid can be regarded as being in contact with the gas and the solid at the same time, according to the Wenzel equation:

$$cos\,\theta_w = f_1\,cos\,\theta_0 - f_2 \quad (3-3)$$

where f_1 and f_2 is the ratio of liquid-solid contact area and liquid-vapor contact area, respectively. According to Cassie's model, increasing the liquid-vapor contact area can improve the hydrophobicity of the material surface. Considering this, the lotus-leaf-like surface with micro-nano hybrid structure has been proved to benefit the trap of air and the formation of air cushion which could increase the contact angle (Figure 3-2d). A special silver mirror phenomenon could be observed when this kind of special surface was immersed in water, which is due to the refraction and reflection of light on the surface of the air cushion. In summary of the wetting theory, existence of low SE of intrinsic surface chemical component basal is pivotal for hydrophobicity [108] and micro-nano hybrid micro morphology will achieve synergistic action which greatly improve the hydrophobicity [109,110].

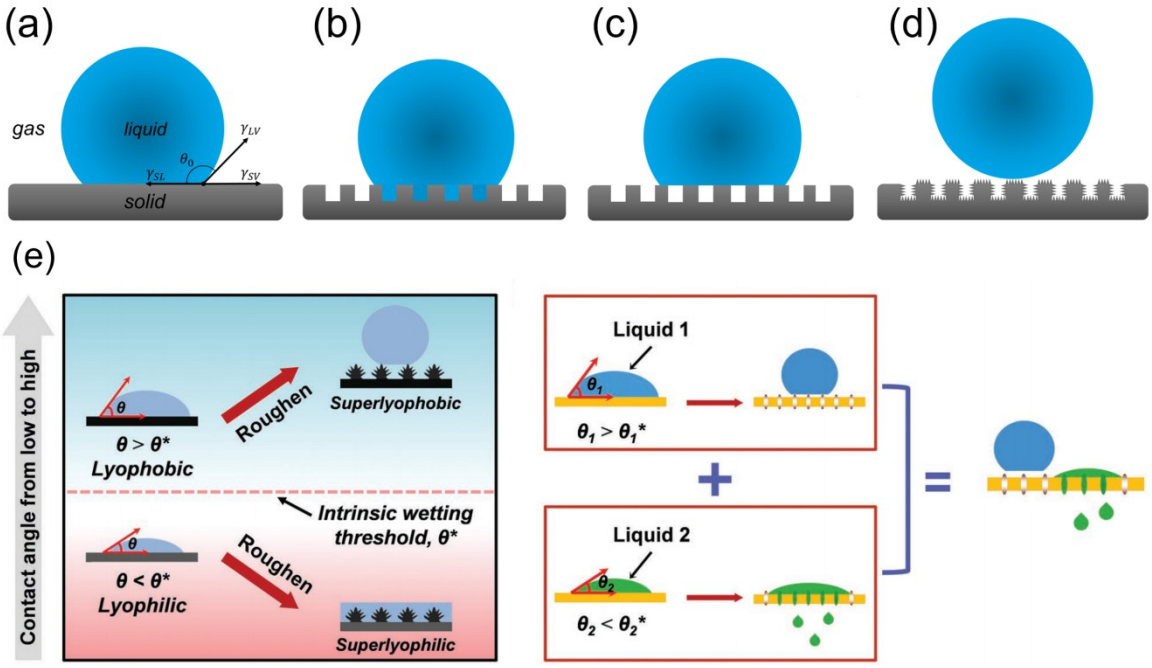

*Figure 3.2 Schematic representation of a water droplet on ideal solid surface refers to **a** the Young equation, and on surface with roughness refers to the **b** Wenzel model, **c** Cassie model, and **d** micro/nano hybrid surface; e Intrinsic wetting threshold θ^* schematic diagram for a given liquid and design pricinple of slective liquid adsorb material [111].*

3.3.3 The theory of intrinsic wetting threshold

Based on Young's equation, the theory of intrinsic wetting threshold substantiates the importance of the SE in the field of immiscible solution separation. As exhibited in Figure 3-2e, intrinsic wetting threshold θ^* represents the boundary between lyophobic and lyophilic of the

liquid which is determined by the SE. As for the idea, lyophobic smooth surface possesses certain chemical composition which θ_0 is higher than θ^*, an increase in roughness leads to an increase in the CA. On the contrary, the CA of lyophilic surface with θ_0 lower than θ^* will be lower when the roughness increases. The theory indicates that if the SE of the solid porous surface lies in the middle of the intrinsic wetting threshold value of two liquids, the liquid with higher surface will not be able to permeate thus achieve the selective separation of liquids [111]. The related γ_{SV} could be obtained by Kwok's equation [112]:

$$cos\,\theta_0 = -1 + 2\sqrt{\frac{\gamma_{SV}}{\gamma_{LV}}}e^{-\beta(\gamma_{LV}-\gamma_{SV})^2} \qquad (3-4)$$

where θ_0, γ_{LV}, θ_w could be measured in experiment and β could be obtained by Newton method. Based on this theory, Wang and co-workers first demonstrated the method to separate a range of organic solvents by precisely adjust the SE of silanes modified surface [113]. In addition, the disparity between water (high SE) and oil (low SE) benefits the separation of them with material which owns the SE in the middle. In summary, porous material owns θ_0 higher than the $\theta^*_{\mathrm{water}}$ and lower than the θ^*_{oil} simultaneously will selectively permeate oil and block water which leads to the separation of oil and water.

3.4 3D-printing technology

3D-printing, an emerging and hopeful processing technology, is a promising candidate which refers to forming three-dimensional products through accumulating materials point by point and layer by layer controlled by computer programs [114-117]. Compared with traditional processing methods, it does not require mold and could be customized simply into many special structures through CAD, CAM and other software according to requirements [118-120]. The main manufacturing process of the product is carried out by 3D-printers, which greatly reduces the consumption of human resources. As illustrated in Figure 3-3, 3D-printing can be divided into a variety of methods according to the disparate raw materials, printing strategies and equipment [121].

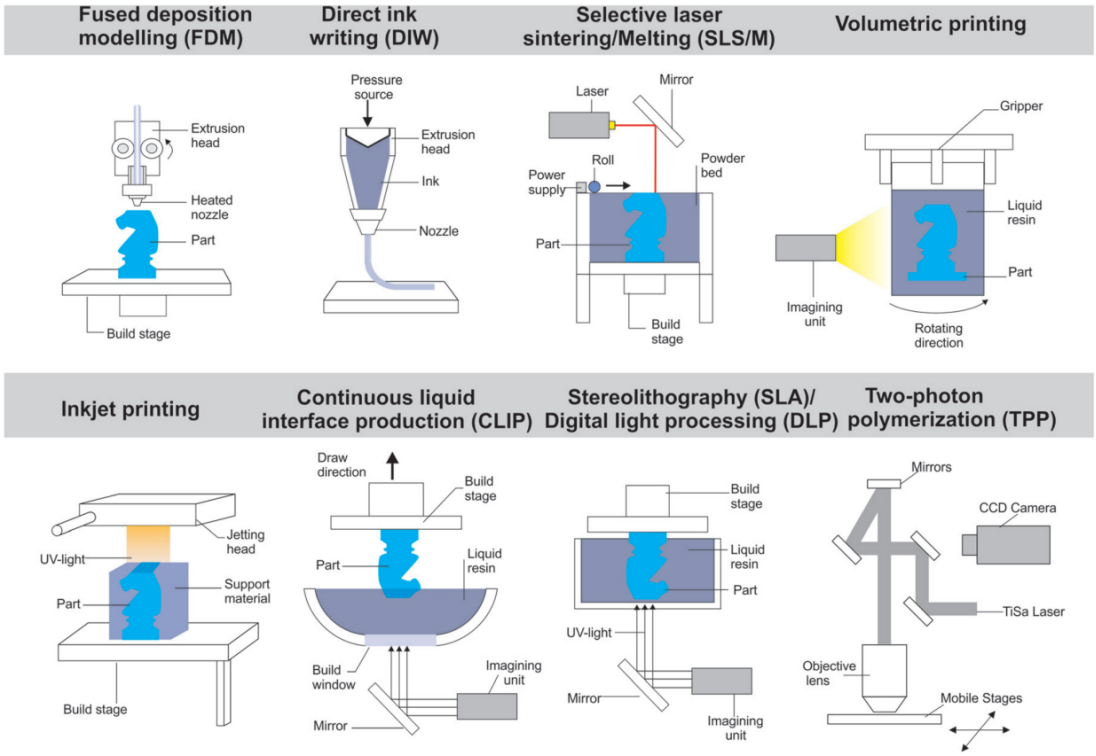

Figure 3.3 Schematic summary of 3D-printing techniques [121].

Fused deposition molding (FDM) is one of the most used 3D-printing technologies [122]. During the printing process, polylactic acid (PLA) [123], polycarbonate (PC) [124], thermoplastic polyurethane (TPU) [125] or other thermoplastic based filament is heated into semi-liquid state and extruded by the nozzle on a mobilizable platform layer by layer to form the designed structure with the aid of the computer system. The printing accuracy of FDM is mostly limited by its nozzle diameter (100 μm). The equipment of FDM technique is inexpensive and commercialized, hence it's an excellent choice for both commercial production and individual user [126].

Direct ink writing (DIW) is an emerging technology for printing functional material including sensor and soft robot [127]. The ink is extruded from the nozzle under external pressure and deposited on the plat form with a designed shape. DIW are compatible with varies of materials, but the ink needs to have stranded rheological properties (non-Newtonian fluids) to promise the flow during the mailing process [128-130]. Like FDM, the printing accuracy of DIW is limited by the diameter of the nozzle (1 μm-100 μm). DIW is a remarkable technique in the field of bioengineering due to its advantage in processing viscoelastic raw material such as living cells and hydrogel [131-133].

Selective laser sintering/melting (SLS/M) is a method based on the principle of high-temperature sintering/melting of powder materials under laser irradiation [134,135]. Computer-controlled positioning devices were applied to ensure the formation of precise structure, and the platform will go down to leave the space for the next layer. Wide range of materials, including polymers such as nylon and polystyrene, metals such as iron, titanium, alloys, and ceramics could be applied in SLS/M method. In case of unnecessary defects of the product caused by edge effect during sintering, the diameter of the raw particle could not be lower than 10 μm which also limit the accuracy of SLS/M [136]. This 3D-printing technique plays an important role in the fields of sensor [137], medical materials [138] and so on.

Inkjet printing technology uses inks that can be cured by UV-light. During the printing process, the ink is cured layer by layer until the designed structure is printed [139,140]. Support structures is evitable in inject orienting, and water-soluble support materials are widely used which can be easily removed with water. Inkjet printing is an efficient method to fabricate customized conductive patterns with excellent mechanical properties [141].

Different from the layer-by-layer forming method, continuous liquid interface printing (CLIP) is a rapid and consecutive printing method whose product is smoother because of the avoidance of the gap between layer and layer [142,143]. The pivotal element of the CLIP printer is the build window at the bottom which will allow the transition of oxygen and UV-light. Oxygen enrichment at the bottom prevents the liquid resin from solidification and thus avoids the adhesion between the product and the substrate. During the printing process, liquid resin will be continuously solidified by the UV-light in the cross-section according to the designed structure. At the same time, a build stage continuously draws the formed product out of the liquid resin vat. CLIP technique could be applicated in the fabrication of medical device [142,144].

Stereolithography apparatus (SLA) is the original light curing printing technology which uses ultraviolet laser (355 nm or 405 nm) as the light source and liquid photocurable resin as raw material [145]. In the printing process, the laser beam outlines the first layer shape of the object on the surface of the liquid resin, and then the build stage will lower which allows the solidified resin to be submerged. The size of the laser beam will define the accuracy parameter of SLA technique [146]. SLA technique is widely used in the fields of drug delivery [147] and biocompatible materials [148].

Digital light processing (DLP) is considered as the second generation of photo-curing printing technology. The cross-section of the designed structure is projected onto the surface of the photocurable resin, and the irradiated resin is photocured layer by layer to form the final structure [149]. The printing speed of the DLP method is generally higher than that of SLA technology, but the size of its products is limited by the resolution of the projector. The DLP method form the designed structure through curing the liquid resin surface to surface, while the volume printing is much faster because it directly cures the entire 3D structure synchronously. During the printing process, several DLP projectors are mounted around the container of liquid resin and simultaneously project images of the cross-section onto the resin [150]. As the container is rotated, selective crosslinking occurs at the irradiated sites and rapidly forms the designed structure.

Among all the printing technologies, commercialized projection micro stereolithography (P-μSL) and two-photon polymerization (TPP) are the promising technology to print high-precision micro-nanostructures which is still a remaining challenge [151,152]. Single-photon absorption (SPA) refers to the process in which excited-state electrons absorb enough energy and transition from a low energy level to a high energy level. The light absorption efficiency is linearly related to the incident light intensity. P-μSL is a printing technology based on SPA polymerization. After the incident light enters the liquid resin, the light intensity gradually decreases under the action of the absorber. Therefore, the effective polymerization reaction only occurs on a very thin layer of the resin surface. Two-photon absorption (TPA) is a process in which excited electrons simultaneously absorb the energy of two photons to achieve a transition. This is a nonlinear effect that the process will be more rapid as the light energy density increases. The TPP method achieves high-precision printing trough controlling the intensity of the incident light which could be enough for the solidification of the focus position of the double beam but insufficient for the generation of TPA around the focus point [153].

3.5 Fabrication of hydrophobic products by 3D-printing

According to the above discussion, a multi-level hierarchy based on microscale and nanoscale surface structure and low SE raw material are two dominating factors to achieve hydrophobicity of the material. Therefore, fabrication of hydrophobic materials remains a challenge. 3D-printing is a versatile method, diverse printing techniques based on different design concepts were reported [154].

All these creative 3D-printing techniques follow a similar technological route, as proposed in Figure 3-4a. Before the printing process, design of 3D models and preparation of raw material including filament, powder, resin, etc. are prerequisite. Following the printing process, various 3D-printers will process the raw material into the shape of designed 3D models with the computerized aids. Finally, the product is obtained directly or after extra treatment.

In this part, the problem of how to achieve hydrophobicity was analyzed in the open literature systemically. Based on ‘web of science’ databases and search equation ‘("3D-printing" OR "additive manufacturing") and (hydrophobic)’, 57 research publications which focus on the fabrication of hydrophobic material was selected. Table 3-1 presents a detailed description of the set of 57 studies. The limited research quantity on 3D printing hydrophobic materials is mainly due to three reasons. Firstly, the range of materials suitable for 3D printing hydrophobic surfaces is still limited. he majority of available materials for 3D printing don’t have good hydrophobicity. Secondly, 3D printing of hydrophobic materials requires a multidisciplinary team with expertise in both 3D printing technology and hydrophobic materials. Finally, the full potential of 3D printing has not been fully utilized, as it enables the production of customized structures with higher efficiency in various application scenarios. As illustrated in Figure 3-4b, the improvement in ‘3D model design’ and ‘after printing process’ are widely used to achieve hydrophobicity. The method in each printing procedure will be investigated and discussed. Figure 3-4c shows temporal distribution of the publications. It is obvious that increasing interests have been focused on the related field. In these studies, 31 of them did not mention a specific application. Nevertheless, improving hydrophobicity will bring benefits such as antiwater and antifouling. The proportion of different applications of these studies are proposed in Figure 3-4d. Oil-water separation is the hottest research field.

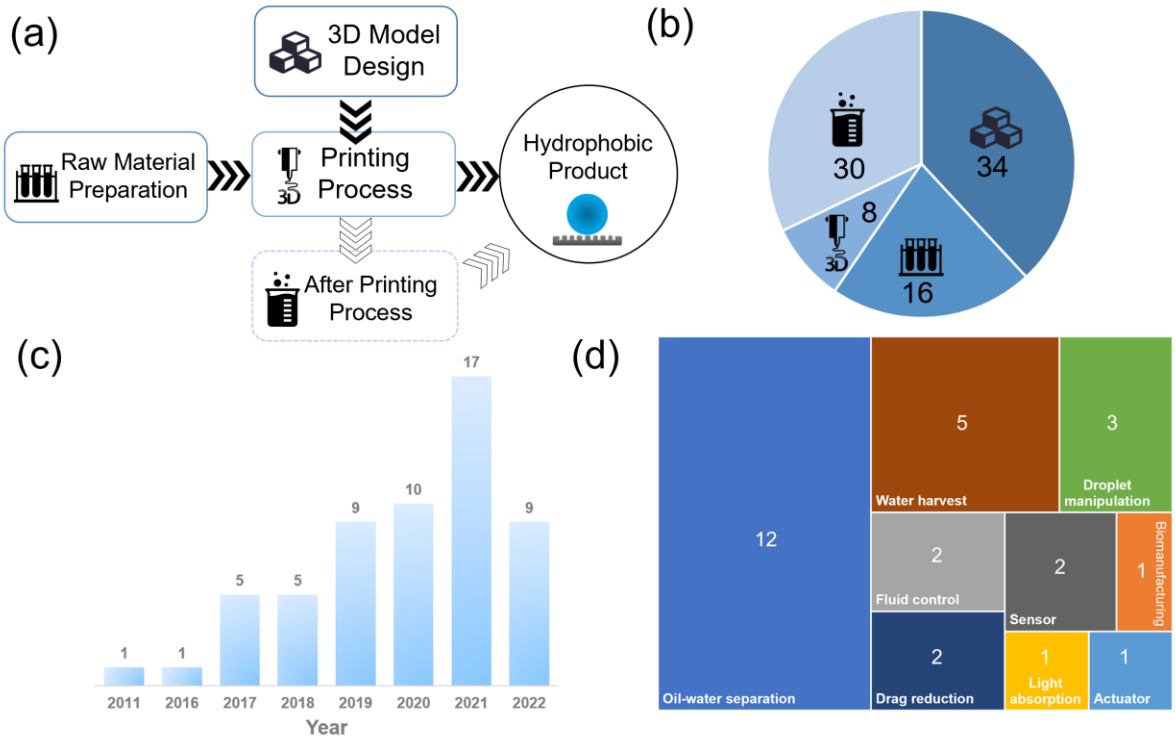

Figure 3.4 ***a*** *Schematic of universal 3D-printing process,* ***b*** *Number of publications achieving hydrophobicity in different promotion route,* ***c*** *Temporal distribution of the publications and* ***d*** *Proportion of different applications.*

Table 3-1 Selected related publication and detailed description. (In 'Process for hydrophobicity' part, '1,2,3,4' represents 'design of 3D models', 'preparation of raw material', 'printing process' and 'after printing process', respectively.

Year	Printing technique	Material	Process for hydrophobicity	Application	Ref
2011	DIW	PDMS	3	/	101
2016	FDM	PLA, PCL	1	Biomanufacturing	155
2017	FDM	PLA	4	/	156
2017	SLS	polyamide 12	4	/	157
2017	DIW	PDMS	1,2	/	158
2017	DIW	PDMS	1,2	Oil-water separation	193
2017	STL	PTFE	1,2,3	/	159
2018	DLP	PEGA, PPGDMA	1	Actuator	229
2018	SLM	Cu	3	Light absorption	160
2018	SLA	Silane mixture	2	Fluid control	161
2018	ISA	Resin	1	Droplet manipulation, Oil-water separation	102
2018	SLM	Ti-Al alloy	1,2,4	/	135
2019	SLA	Resin	1	Drag reduction	162
2019	FDM	PLA	2	/	163
2019	FDM	PLA	4	/	123
2019	FDM	PDMS	1,4	/	164
2019	FDM	PLA	4	/	165
2019	PSL	Resin	1,3	Droplet manipulation, Drag reduction, Oil-water separation	226
2019	DIW	PCL, PDMS	1,4	Oil-water separation	202
2019	DLP	Resin	1	/	166
2019	FDM	Polyimide	1,4	Oil-water separation	210
2020	ISA	Resin	1	Water harvest	167
2020	SLA	Photopolymer	1	/	190
2020	SLS	PA	4	Oil-water separation	134
2020	FDM	PLA, ABS	4	/	199
2020	DLP	DPGDA	1,2	/	168
2020	SLM	Cu	1,4	/	169

2020	FDM	PLA	1,4	Water harvest	215
2020	FDM	PLA, PDMS	1,4	/	203
2020	Inkjet printing	PTFE	1,2	/	170
2020	m-SL	Resin	2,3	/	198
2021	PSL	Resin	1	Fluid control	171
2021	PSL	Resin	1	Droplet manipulation	172
2021	SLA	Resin	1	/	191
2021	FDM	PLA	1,2	Water harvest	173
2021	SLA	Photopolymer	2,4	Water harvest	103
2021	DIW	PDMS	2	/	174
2021	Electrochemical printing	Cu	1,2	/	175
2021	FDM	PLA	1,4	Oil-water separation	204
2021	FDM	PVDF	4	Oil-water separation	211
2021	SLA	Resin	1,4	/	176
2021	DLP	Ceramic	1,4	Oil-water separation	177
2021	DLP	Ceramic	2,4	Oil-water separation	178
2021	DLP	Resin	2,4	Oil-water separation	197
2021	FDM	ABS	4	Underwater sensor	179
2021	DIW	PDMS	4	/	180
2021	SLA	PFPE	4	Oil-water separation	181
2021	SLM	Stainless steel	3	/	182
2022	SLM	Ti-Al alloy	3	/	183
2022	SLA	Photopolymer	1	/	184
2022	FDM	PLA	2	/	196
2022	FDM	PLA	1,2	Water harvest	185
2022	SLM	Ti-Al alloy	4	/	186
2022	DIW	PDMS	2	Sensor	194
2022	SLA	Photopolymer	1,4	/	187
2022	Multi Jet Printing	PLA	1,4	/	188
2022	SLM	Nickel-based superalloy	4	/	189

3.5.1 3D model design

First is the model design part, where a model should be designed by the computer which gives us space to build our desired structure. Among all these miscellaneous 3D-printing technologies, some of them could print material in a designed nanoscale structure which enable us to directly build some similar hydrophobic surface inspired by nature with a nanoscale surface structure [190]. By mimicking this pillar-like structure (PLS), many hydrophobic surfaces have been developed. PLS in various shapes fabricated via fast and affordable SLA printer has been demonstrated by Cruz and co-workers [191]. In this work, SLA printers were used to print PLS arrays with variety shapes including pine, sphere, spiral, stepped pyramid, cube, mouse, mushroom, tulip, cone, and cylinder in two orientations as shown in Figure 3-5a. In addition, to lower the SE, all the samples have been salinized after the printing process. The sample with a flat surface has also been fabricated for comparation. Figure 3-5b shows the static CA of PLS with 10 different geometric shapes. Compared with the flat sample, PLS exhibit much higher CA due to the special microstructure. Interestingly, the PLS fabricated with a tilted direction at 33° owns a higher contact angle than the samples fabricated in the horizontal direction. This was attributed to the stair-case effect that the tilted printing samples have a reduced contact area compared with the horizontal printing PSL [192]. As illustrated above, many intriguing hydrophobic structures have been discovered in nature. Considering this, biomimetic models could be built and printed. Yang et al illustrated an innovative eggbeater structure inspired by hydrophobic S. Molesta leaf (Figure 3-5c) [102]. The customized model of eggbeater arrays shown in Figure 3-5d was built with SolidWorks software. The peculiar geometry structure enables the material to manipulate droplets. The adhesive forces to the water droplet could be adjusted by changing the increment of eggbeater arms.

As a result, designing a model with the biomimetic structure will greatly improve the hydrophobicity of the printed materials and endow them with different application outlooks. Unfortunately, some 3D-printing technologies are limited by the feature resolution which result in failure to build nano structure.

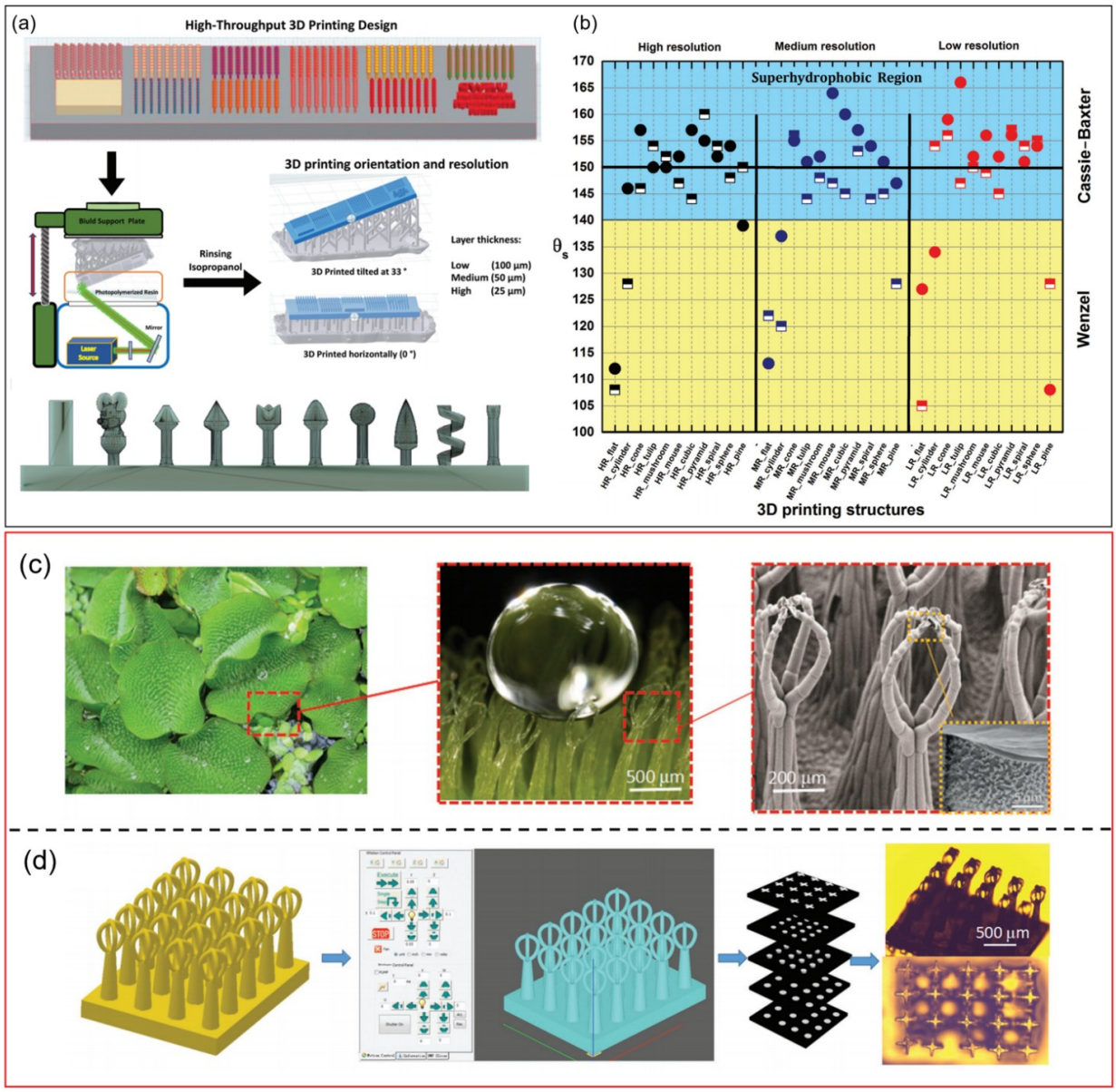

Figure 3.5 ***a*** *Schematic of the fabrication procedure for hydrophobic PLS structure by SLA technique and its variety shapes of printed structure;* ***b*** *CA of samples fabricated in different orientation, resolution, shapes [191];* ***c*** *S. Molesta leaf and its hydrophobicity as well as the SEM image of the surface with eggbeater structure;* ***d*** *SolidWorks modeled eggbeater structure [102].*

3.5.2 Raw material preparation

Another part before the printing process is raw material preparation in which the filament, ink and photocurable resin could be processed for the application of FDM, DIW and SLA technologies. Adding fillers with low SE to the raw material will change the chemical content and the micro geometry structure of the surface of the material which will be an efficient way to improve

hydrophobicity but there remain challenges to get the homogeneous mix of the raw material and the filler.

Lv and co-workers put forward a typical ink for DIW technology to fabricate mechanically durable superhydrophobic porous membrane [193]. As shown in Figure 3-6a, during the ink preparation part, different amounts of silica nanoparticles were added into the ink. The additional silica particles bring two crucial benefits. First, it improves the rheological property of the ink to make it printable. Storage (G′) and loss (G″) moduli are functions of shear stress for polydimethylsiloxane (PDMS) inks with various silica loadings. When the additional silica particles loading reached 15%, G″ will be higher than G′ under high shear stress which means that the ink will be able to flow during the printing process. Furthermore, G″ will be lower than G′ under low shear stress which enables the ink to reach solid-like state to maintain its designed geometry structure after leaving the nozzle. Second, the additional silica particles could lower the SE and simultaneously bring a nano-scale roughness structure which will benefit the hydrophobicity of the membrane. As a result, the additional silica nanoparticle is the key element for the successful fabrication of the hydrophobic membrane. Wang et al reported silicone-based ink which contains silica nanoparticles and wax micro-particles [194]. As illustrated in Figure 3-6b, the additional wax micro-particles could modify the rheological properties by introducing a temperature sensitive micro- and nanoscale network [195]. Besides, low SE of wax also benefits the hydrophobicity of the material. Rajakaruna and co-worker demonstrated a method to fabricate filament consisting of PLA, hexadecyltrimethoxysilane (HDTMS) and polytetrafluoroethylene (PTFE) for FDM printer [196]. The additional fillers help create a new extra PTFE layer above the original surface which improves the hydrophobicity of the material. Dong et al designed a novel ink for DLP printing technology consist of hydrophobic (meth) acrylate monomers and pyrogen solvents [197]. As demonstrated in Figure 3-6c, combined with leaching process after printing to remove the polymer poor phase, a bulk hydrophobic material could be obtained.

In summary, it is efficient to improve hydrophobicity during the raw material preparation part, however too many costly and complicated fillers will limit the largescale production and costs second pollution during practical application.

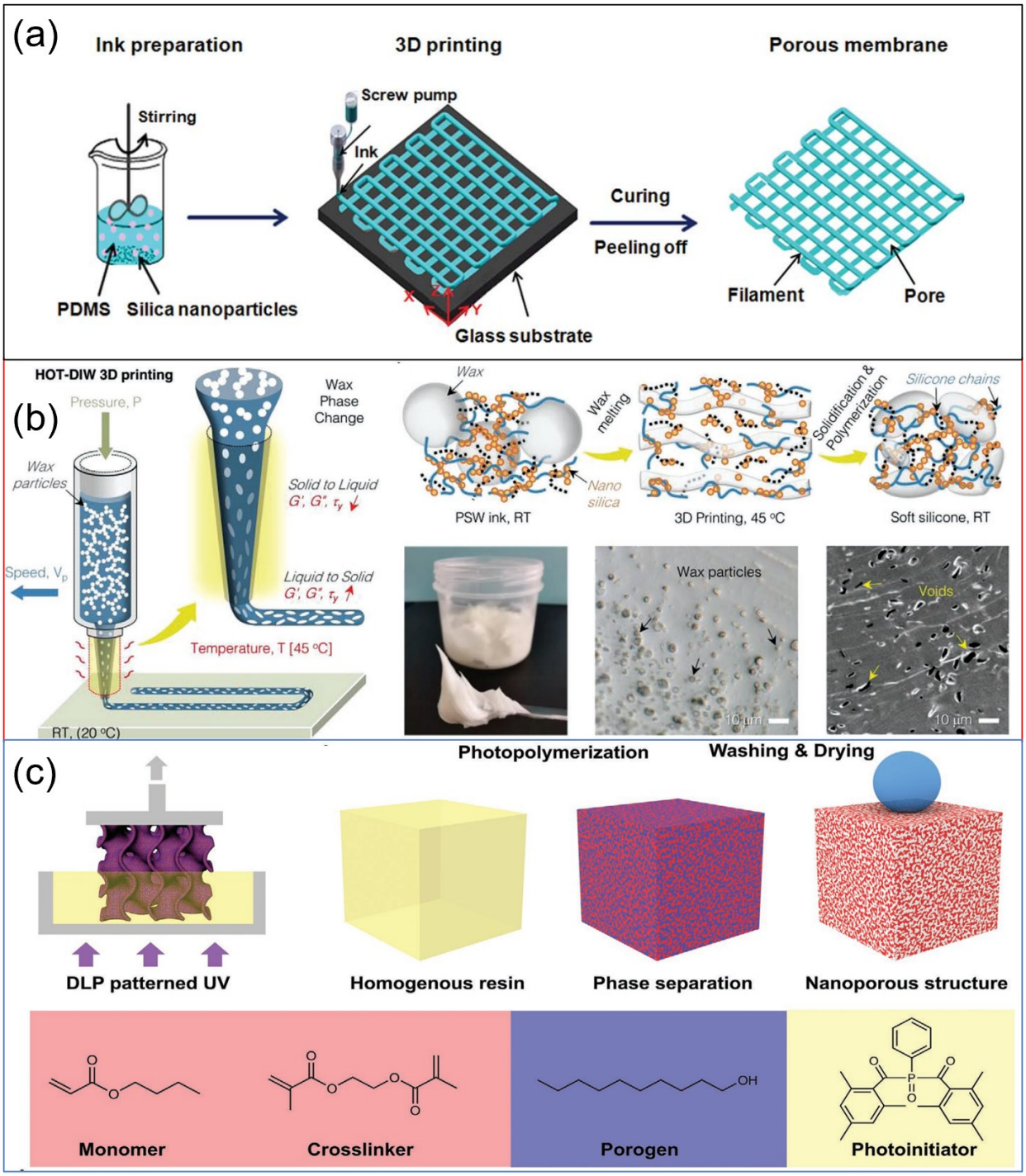

*Figure 3.6 Schematic of the fabrication procedure of **a** PDMS based mechanically durable superhydrophobic porous membrane via DIW technique [193]; **b** Phase-change-enabled, rapid, high-resolution of soft silicone-based material via DIW technique [194] and **c** Superhydrophobic objects with bulk nanostructure via DLP technique [197].*

3.5.3 Printing process

During the printing process, the 3D-printer will be controlled by the computer system and finishing the process automatically results in more challenges in achieving hydrophobicity improvement at this stage. However, some extra support method will contribute to the formation of the geometric structure and the modification of parameters during the printing process will also be helpful.

As shown in Figure 3-7a, Barahman et al. proposed a method to fabricate Ratchetlike structure via precisely controlling the route of the nozzle while printing, which will be considered as the first publication about the fabrication of biomimetic hydrophobic material via 3D-printing [101]. The highest CA of the fabricated sample could reach 161°. Joyee and co-workers develop a magnetic field-assisted method for SLA technology to build biomimetic structure which is already a wide-used technology in polymer manufacturing [198]. In the printing process, magnetic particles or particle suspension were deposited in the polymer resin under the accurate control of a programmable computer system (Figure 3-7b). Under the strong magnet field, the magnetic particles will be re-assembled into micro clusters and create roughness structure on the surface of the material (Figure 3-7c) which makes the CA of the surface increasing from 38° to 146°. Yang et al. prepared a PLA/ABS hydrophobic surface by precisely choosing the optimal printing parameter for FDM technology including printing speed and grid filling method [199]. The result of the experiment shows that the layer thickness and filling will influence the micro morphology of the printed material.

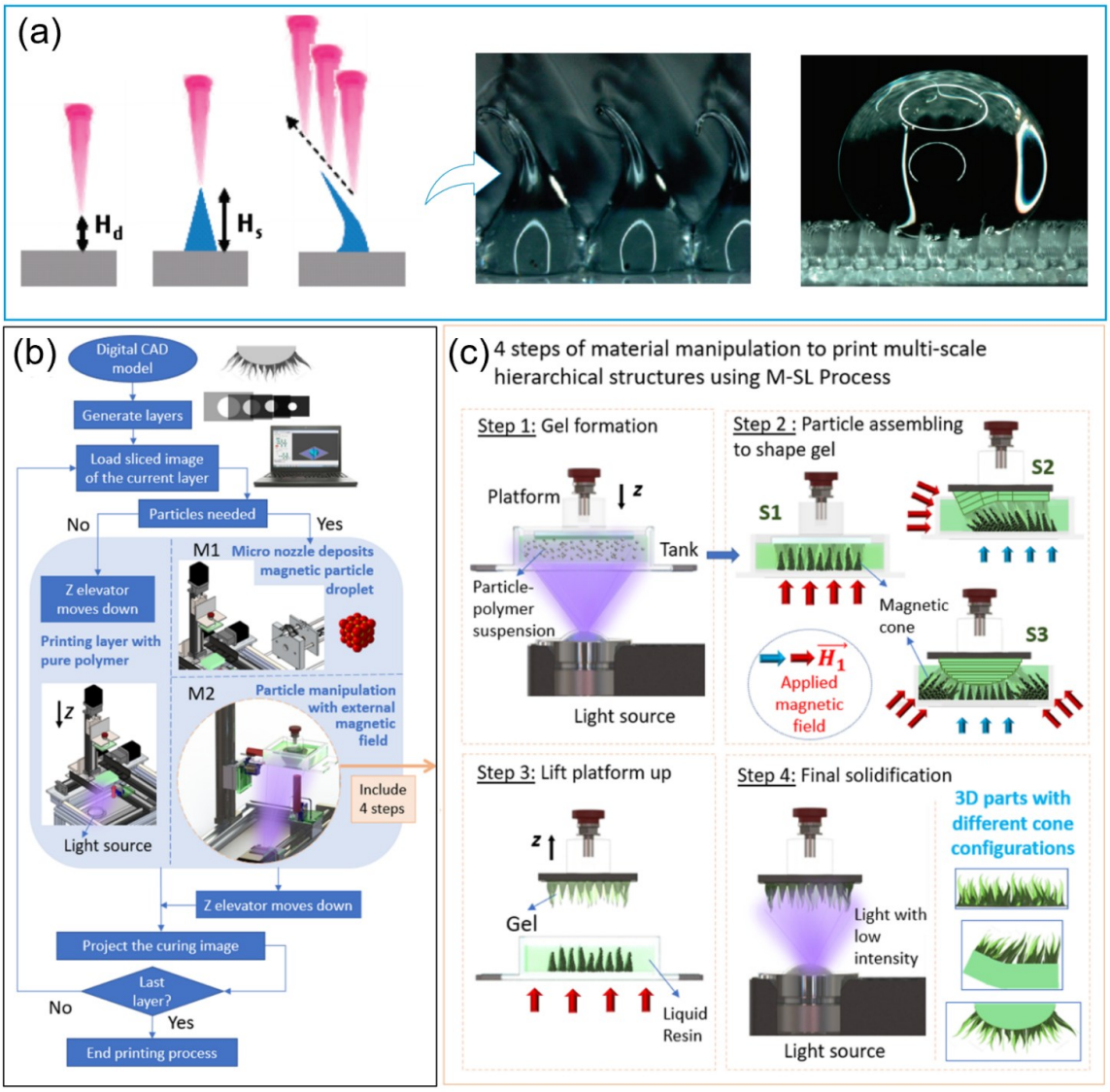

Figure 3.7 ***a*** *Illustration of key parameters and procedure in the printing process for Ratchetlike structure [101];* ***b*** *Flow diagram for the magnetic driven fabrication of hybrid hierarchical structures;* ***c*** *steps for printing the hierarchical surface structures [198].*

In the printing process, ingenious auxiliary device systems will be a creative way to fabricate hydrophobic structure. Furthermore, many parameters, such as temperature may also be a key factor affecting the wettability of the material surface. Above the glass transition temperature, the molecular chains of polymers can move freely and form structures without defects [200,201], which may have an impact on the microstructure and wettability of the material surface. Nevertheless, up to now, no relevant research has focused on this topic.

3.5.4 After printing process

After the fabrication of original material, some methods could be applicated to increase hydrophobicity. Limited by the printing feature resolution, some 3D-printing technologies are not able to form nano-scale roughness structure directly. Therefore, after printing process, it is necessary for the material to gain hydrophobicity. In some research works, the material printed has been used as a model instead of as the final product. PDMS is a common material in the field of hydrophobic material fabrication, because of its low SE and excellent mechanical properties. Before cross-linking, PDMS shows a state between liquid with high viscosity and semi-solid which could be able to fluid while processing. The cross-linked PDMS will become a chemically stable elastomer with mechanical properties determined by crosslinking ratio. PDMS could be used as a key element of the ink for DIW technology directly but in some works based on 3D-printing technologies, sacrificial-template methods were applied for the processing of PDMS materials. Shin and co-workers reported a sacrificial-template method to fabricate bioinspired PDMS sponge for oil-water separation [202]. As shown in Figure 3-8a, first a polycaprolactone (PCL) porous template has been printed followed by the curing of PDMS in the template and finally the template has been removed by acetone with a porous PDMS sponge left. The PDMS sponge shows a micro-scale roughness structure (Figure 3-8b), good elasticity and hydrophobicity with a CA of 143°. Kang et al demonstrated a 3D-printing PLA template for the fabrication of hydrophobic pyramid-shaped PDMS surface which shows a low adhesion force to the water droplet and has promising application fields such as agriculture, bioengineering and aeronautics (Figure 3-8c and d) [203]. Coating was a simple and widely used method for the modification of the original 3D-printing material to improve its properties. Guo et al presents a coating method for the fabrication of superhydrophobic PLA membrane. In this work, commercial 3D-printer has been applied [204]. Limited by the feature resolution of the FDM printing, the original material has been designed without a nano-scale roughness. Herein, the printed PLA membrane has been immersed in methyl ethyl ketone (MEK) solution with hydrophobic nanoparticles and 1H, 1H, 2H, 2H-perfluorodecyltrichlorosilane (FDTS). After the coating process, a nano-scale roughness structure was obtained because of the silica nanoparticles bonded by the MEK on the surface and the SE was lower due to the existence of the FDTS. As a result, a superhydrophobic surface with a CA of 170° was obtained and ready for application. Dip-coating method is a familiar treatment to improve hydrophobicity. As illustrated in Figure 3-8e, Lee and co-workers demonstrated a PLA

superhydrophobic surface obtained by immersing the samples in the solution consists of methyl ethyl ketone (MEK) and silica nanoparticles [123]. The promotion of hydrophobicity was owing to the low SE of silica nanoparticles. Besides, only small mechanical properties could be observed because of the swelling-effect caused by MEK which means the treatment mainly influences the surface properties.

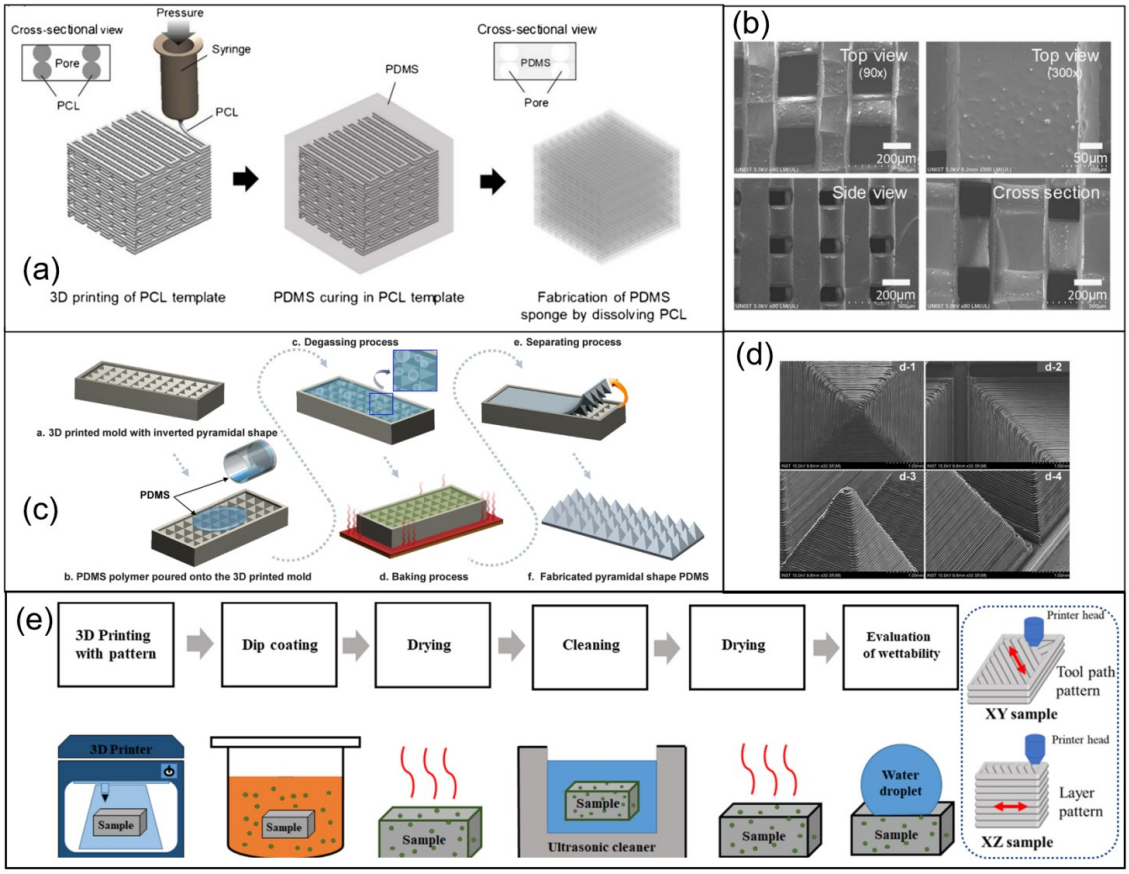

*Figure 3.8 Schematic of the fabrication procedure of **a** PDMS sponge fabricated with PCL template and micro morphology **b** [202]; **c** 3D PDMS surface fabricated with PLA template and micro morphology **d** [203]; **e** Dip-coating method for the fabrication of superhydrophobic PLA surface [123].*

After the printing process, there is an unnecessary part in the 3D-printing technology which makes the production more complicated and expensive. Nevertheless, many printing technologies are limited by the feature resolution to achieve hydrophobicity. Therefore, developing facile and cheap methods to improve the hydrophobicity of the material after printing remains a challenge.

In summary, many creative post-treatment methods have been proposed for 3D-printing techniques to improve hydrophobicity which makes 3D-printing a promising technology to

fabricate hydrophobic material. In future, research should focus on large-scale and industrialization. Because most of the post-treatment methods are complicated and time-consuming.

3.6 Application of 3D-printed hydrophobic material

It is very important and challenging to translate the results of the laboratory into practical applications. As shown in Figure 3-4d, based on 3D-printing technique, diverse applications have been proposed. Herein, we will introduce four research fields with practical application value. Compared with other applications, they have more urgent practical demands. Among them, oil-water separation and water harvest have attracted more extensive attention from researchers. Drag reduction can effectively reduce energy consumption during traffic transport. Besides, there is still a lack of relevant reports on 4D printing technology which has high application possibilities such as actuators. Other fields of application such as droplets manipulation and fluid control focus more on the experiment techniques. Besides, hydrophobicity could help the material gain the ability of anti-water which will benefit their performance in the fields such as sensor, biomanufacturing and light adsorption.

3.6.1 Oil-water separation

Among these applications, the preparation of oil-water separation materials is in urgent demand because of the growing threat caused by oil spill accident. Traditional leaked oil treatment such as biological treatment [205] and burning [206], have been wildly used but these methods are limited by their low efficiency. With the inspiration of nature, growing attention has been focusing on the hydrophobic oil-water separation material including aerogel [207], monolith [66,94], microsphere [208], and membrane [104] which own the ability to selectively separate oil from water. The theoretical background of the high efficiency separation was mentioned in part 2.3 known as the intrinsic wetting threshold.

These days, 3D-printing has become a promising technology in the field of oil-water separation. Han and co-workers present a novel method to fabricate hydrophobic ABS-Nickel (Ni) membrane for oil-water separation with a highlight on coating process [209]. In this work, original porous ABS membrane has been fabricated with a commercial FDM 3D-printer. Whereafter, the membrane was coated with Ni via an in-situ reduction method. After the coating process, an increase of the C-OH group could be observed which demonstrates that there will be more

hydroxyl groups on the surface. Considering this, the hydrophilicity of the surface will be greatly increased, and the membrane show a high oil CA underwater which means after wetting with water the membrane could be able to block oil and let water pass freely thus achieve oil-water separation. Notably, the performance of the material could benefit by the smart designed 3D structure in which typical fabrication method including electrospinning, phase separation and templating was limited to fabricate. However, through customized 3D-printing, this dimensional limitation can be broken, and more efficient oil-water separation can be achieved. Li and co-workers demonstrate an interesting 3D-printing device for oil water separation [210]. The graphene has been printed on the surface of nickel foam which has been bent into a tube-like structure. As shown in Figure 3-9a-c, combining with a vessel the tube could collect oil on the water surface using the hydrophobicity of the surface which blocked water. Figure 3-9d illustrates the smart design of a new concept leaked oil collector. The skeleton could also be obtained by 3D-printing technology which could achieve self-floating. The device could remain on the water surface while collecting leaked oil with zero energy consumption. Xu et al reported a similar design of oil collect device [211]. As illustrated in Figure 3-e, the smart device consisted of a 3D-printing polyvinylidene difluoride (PVDF)skeleton and a hydrophobic coated copper mesh. Notably, the structure of the collector has been designed into circular truncated cone which owns the fastest collecting speed compared to the tube-like and other structure. With the connection of the device to the pump, the high efficiency oil-water separation could be achieved (Figure 3-9f). The adsorption capacity is a significant property of the leaked oil adsorbent. Inspired by water collecting behavior of cactus, Shin and co-workers fabricated a hollow sponge with a hydrophobic surface which has more space for the storage of collected oil (Figure 3-9g) [202].

Many works for the fabrication of oil-water separation materials via 3D-printing have been proposed which utilizes the advantages of 3D-priting. Compared with traditional fabrication method, 3D-printing could provide more customized shape which could greatly increase the efficiency of the separation. In the future, research should focus on developing simple and low-cost methods.

3.6.1.1 Limitations of 3D-printed structures for oil-water separation

The literature survey also reveals two practical gaps that motivate the present work. First, many reported routes for fabricating 3D-printed hydrophobic surfaces rely on complex ink formulations, multistep templating or post-treatments (e.g. leaching, plasma, multi-layer coatings), which

increase cost, processing time and barriers to scale-up. There is a clear need for simplified, more robust fabrication strategies that can achieve reliable hydrophobicity while minimizing chemical complexity and processing steps. Second, although additive manufacturing inherently enables three-dimensional design freedom, most existing studies still focus on 2D membranes or simple planar coupons and rarely exploit fully 3D architectures tailored for continuous separation or integrated collection functions. The limited exploration of structurally optimized 3D collectors and porous networks for oil–water separation therefore represents a key opportunity that this thesis aims to address.

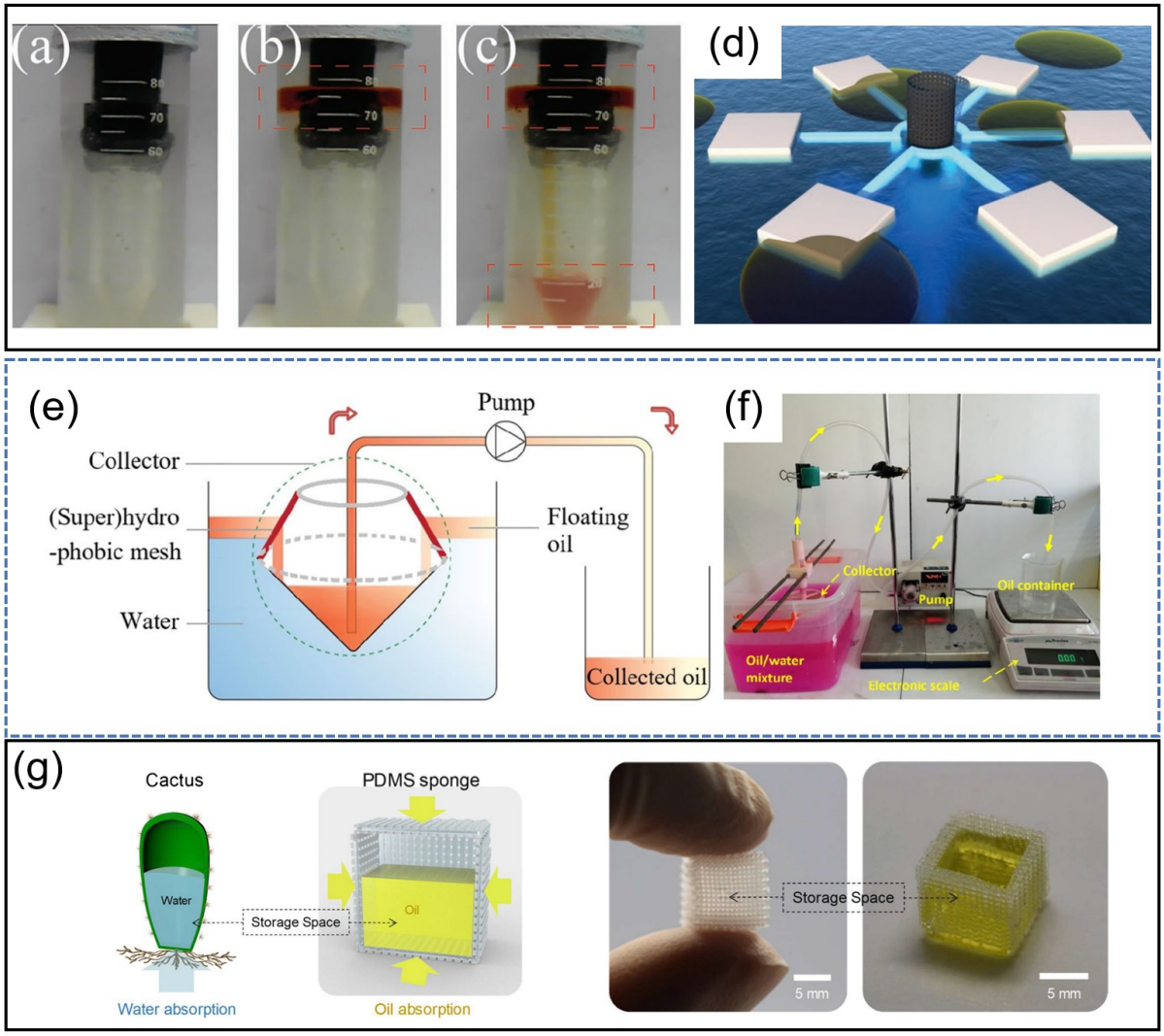

Figure 3.9 ***a-c*** *3D-printing oil recycling membrane and* ***d*** *ideal oil collector floating on the water surface [210];* ***e*** *Hydrophobic cooper mesh and 3D-printing PVDF skeleton hybrid oil collector and* ***f*** *its pumping application [211];* ***g*** *Cactus inspired oil adsorbent and schematic of its high oil-storage [202].*

3.6.2 Water harvest

Numerous regions of the world are facing severe water scarcity, and how to efficiently achieve water harvesting remains a challenge [103]. Many creatures survived in the arid environment could collect water from the fog with the aid of intriguing microstructure, such as Namib Desert Beetle with humps on their carapace [88], spider web with periodical geometry structure and regularly distributed conical spines on the surface of cactus [212]. The mechanism of these creatures were studied for the inspiration of the fabrication of water harvest material.

For instance, Figure 3-10a-c shows the optical images of the cactus stem in different viewing angle. Obviously, acicular spines formed hemispheric cluster were distributed regularly on the surface [213]. As shown in Figure 3-10d, acicular spines consist of oriented barbs on the cusp, gradient grooves in the middle and belt-structured trichomes on the root. The water harvesting procedure could be demonstrated as follows. First, the small water droplets have been captured and sedimented on the oriented barbs. Second, with the advance of the capture procedure small water droplets begin to integrate droplets with increasing size. Following the captured big droplets moving towards the orientation of the spine and finally adsorbed by belt-structured trichomes part. The cone shape of the spine generated gradient Laplace pressure, and the gradient wettability of the spine are the two mean factors to achieve water harvesting. The spine could seem like a cone with an increasing semidiameter from the root to the cusp. According to the Laplace pressure theory, the droplets will be forced to move towards the direction of the increasing semidiameter [78,214]. The cone structure generated Laplace pressure gap (ΔP) could be defined as follows:

$$\Delta P = -\int_{R_1}^{R_2} \frac{2\gamma}{(R+R_0)^2} sin\,\alpha\, dz \qquad (3-5)$$

R, R_1, R_2 and R_0 represent the local radius of the spine, radius of the cone in front and behind the droplet and radius of the droplet, respectively. α is half angle of the spin tip and dz is the incremental of the radius. It is obvious that the Laplace pressure adjacent to the cusp side is larger than the side adjacent to the root which will explain the force driven the droplets to move along the specific direction.

As we discussed in equation (2), for the surface with consistent chemical content, the CA will increase with the increase of the surface roughness. A decrease of roughness from the cusp to the root could be observed on the spine which generated gradient wettability. The gap of wettability

between the front and back side of the droplet will also cause driven force (F_w) [78] shown as follows:

$$F = \int_{l_{cusp}}^{l_{root}} \gamma(cos\,\theta_1 - cos\,\theta_2)\,dl \qquad (3-6)$$

where θ_1 and θ_2 represent the CA of the front side and back side of the droplet. dl represents the variable of integration from the side adjacent to the (l_{cusp}) to the side adjacent to the root (l_{root}). As we discussed above, the side adjacent to the root shows a lower CA. Therefore, the driven force caused by the gradient wettability will be in the direction from the cusp to the root.

As shown in Figure 3-11a, Namib desert beetles show another way to achieve water harvesting [215]. Their carapace is not only hydrophobic but also covered with some hydrophilic humps. The water droplet will be captured by the hydrophilic and accumulated into larger droplet following the sliding along the hydrophobic low-adhesion carapace driven by gravity.

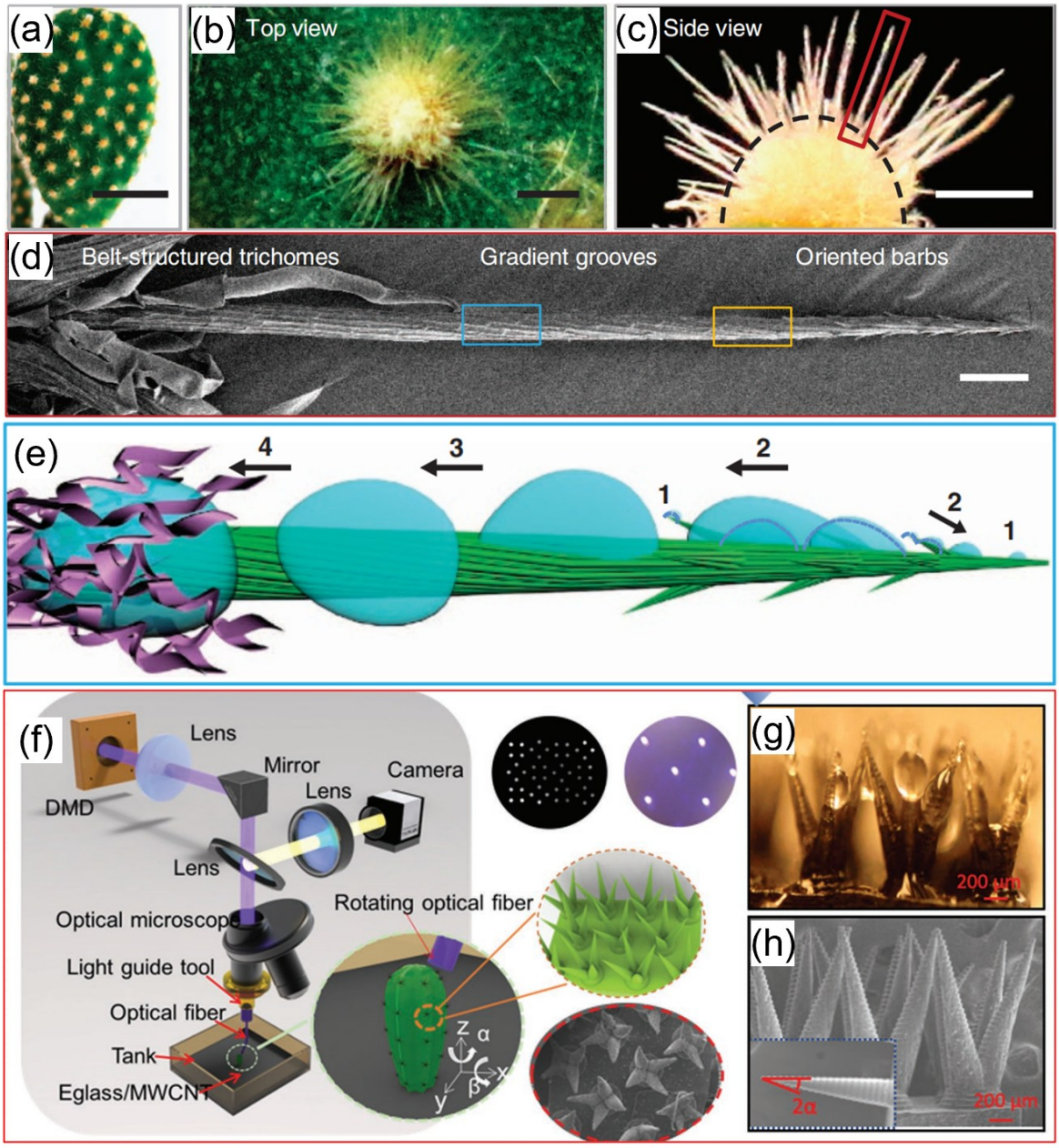

Figure 3.10 ***a-c*** *Optical image of cactus at different viewing angle;* ***d*** *SEM image of a single spine and three divided zones;* ***e*** *Schematic of water collection steps on single spine [213];* ***f*** *Fabrication process of cactus-inspired surface via 3D-printing;* ***g*** *Water harvesting behavior and h SEM image of the fabricated surface [219].*

Based on the inspiration from nature, many research has focused on reproducing the intriguing microstructure to achieve water harvesting and solve the increasing water shortage challenge in many droughts' region. Many methods have been applicated to fabricate the biomimetic surface, such as UV-induced technique [216], aerogel coating [217] and selective modification [218]. Compared with 3D-printing, these methods were limited by the complicated equipment and high-

cost raw material. Furthermore, the microstructure could not be controlled precisely and freely. Inspired by intriguing water collection behavior of cactus, Li and co-workers demonstrated a high efficiency and eco-friendly water harvesting device via 3D-printing [219]. As illustrated in Figure 3-10f, a surface with diverse spines texture was fabricated and splashed with a hydrophobic coating. As illustrated in Figure 3-10g, the bio-mimetic surface could achieve water collection. Because of the advantages of 3D-printing, researchers could design surfaces with numerous shapes arranged clusters and diverse arrangement of multibranched spines and investigate their water collection efficiency. Han et al developed a novel method to fabricate water harvesting surface [215]. In this work, a PLA template with certain roughness was printed with FDM technology and etched with organic solvent for the creation of nano and micro-scale roughness (Figure 3-11b). With the application of this template, hydrophobic PDMS surface was been created and hydrophilic Pt metal has been deposited on the surface with a metal sputter. After the modification, the surface shows higher water collection ability (Figure 3-11c). Thus, a hydrophobic and hydrophilic hybrid surface inspired by the desert beetle was obtained with 42.6% increased water harvesting efficiency. Peng and co-workers demonstrated an enhancing water collection structure fabricated by UV-induced controllable diffusion method and 3D-printing technology [103]. As shown in Figure 3-11d, the structure was designed with cones inspired by the cactus and a hybrid coating with hydrophobic and hydrophilic content inspired by the beetle. Structures with different cone distances (Figure 3-11e) and with or without holes (Figure 3-11f) were all fabricated and investigated because of the flexibility of 3D-printing technology. The water collecting rate of the structure fabricated with optimized parameter could reach 2.68 g h-1 cm-2 which is higher than many reported structures. The combination of Laplace pressure and hybrid wettability surface was the key element to achieve water harvesting.

In the future, related research should focus on applications in real natural environments.

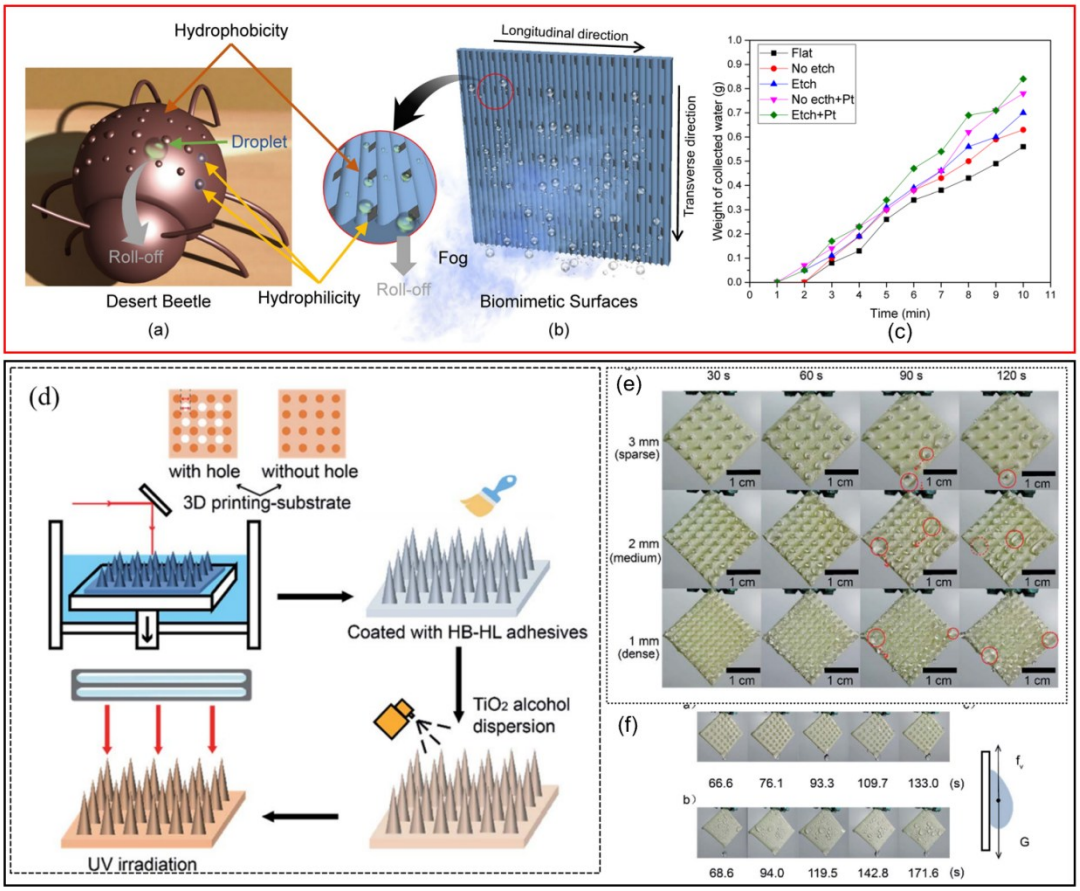

Figure 3.11 ***a*** *Schematic about water harvesting behavior of the Namib desert beetle and* ***b*** *the 3D-printing inspired surface;* ***c*** *Water collection efficiency of surface with different coatings [215];* ***d*** *UV-induced controllable diffusion method and 3D-printing technology for the fabrication of bio-inspired water harvesting surface;* ***e*** *Water collection efficiency of surface with different cone distance and f wholes or without wholes [103].*

3.6.3 Drag reduction

Drag is a superfluous force which induces additional energy consumption in ships, turbines and pipelines. Therefore, the design of drag reduction surface could effectively reduce energy loss and bring considerable economic benefits [220]. For instance, sharks are one of the fastest swimmers in the ocean. Their riblets with exceptional microstructure on dermal denticles could help them achieve antifouling and drag reduction (Figure 3-12a). The antifouling phenomenon relies on the special microstructure which is similar with the lotus leaves to achieve liquid repellence and self-cleaning. Compared with many other creatures in the ocean such as Humpback whale covered with barnacles, sharks own a cleaner skin [221].

To fabricated surface with drag reduction ability, the mechanism of the generation of drag should be studied. Initially, the drag force could be divided into the pressure drag force which is the necessary force consumption to remove the fluid blocked in the direction of motion and the friction drag force which could be demonstrated as the interaction between the surface and the hithermost fluid layer [222]. The streamlined body of shark, similar with the design of many vehicles such as roadster and aircraft wings, will benefit the reduce of the pressure force. The boundary layer of laminar which controlled by the interaction between the fluid molecular or turbulent which controlled by the inertial force is the fluid layer press close to the surface. Increasing momentum transfer and shear stress could be observed in the turbulent boundary layer due to the movement and mixture of the generated vortices which lead to the higher drag force. The special microstructure of shark skin covered with dermal denticles which own the riblets parallel to the swimming direction have been proved to be able to control the generated vortices and thus reduce the drag force [223]. Therefore, based on the mechanism of the drag reduction behavior many practical applications could be applied.

Many methods have been developed such as textured liners and laser cutting for the fabrication of the sharkskin-like structure [224]. However, these methods are limited to reproduce the complicated dermal denticles microstructure of the sharkskin with high feature resolution and high throughput. 3D-printing technology is a promising candidate to achieve high resolution reproduction of biomimetic surface. For instance, Wen et al developed a multi-material printing method for the fabrication of biomimetic shar-skin like structure [222]. The high-resolution model of the shark skin is obtained by micro-CT scan and results in 8.7% drag reduction in the static hydrodynamic experiment. During the liquid transportation through pipelines, which significantly increases the cost. Li and co-workers used an optimized multiscale SLA technology to rebuild the shark skin microstructure pipe precisely [162]. Figure 3-12b-d shows the 3D models of the denticles, the printed denticles, and the parameter of the denticles, respectively. Obviously, each denticles is suspended with a large space which is hard to reproduce with other manufacturers. As shown in Figure 3-12e and f, multiscale stereolithography technology allows to print different structures with different resolutions. For the pipe wall, the large laser beam has been adapted to rebuild the low-resolution part. For the denticle features, small beam was applicated to reproduce the high-resolution microstructure. Therefore, multiscale SLA is a precise and low-cost technology

to rebuild the biomimetic surface. As a result, the printed shark skin like surface presents 10% drag reduction in the pipe flow setup experiment.

Inspired by droplet pining effect of nepenthes peristome, petal-like microstructure for droplet manipulation, oil-water separation and drag reduction was presented by Liu and co-workers [225]. As illustrated in Figure 3-12g, by precisely controlling the parameter of the surface such as the petal number, spacing distance and ratio of arch length to circumference, the printed surface showed high water repellence. In this work, a drag force monitor was used to test the drag reduction of the material and the different flow velocities were applicated. An obvious drag reduced effect could be observed, especially in the high velocity (0.12m/s), as shown in Figure 3-12h. The bubble captured by the hydrophobic surface may cause boundary slip effect thus reducing the drag force.

Material with drag reduction behavior could effectively reduce energy consumption and generate economic benefits. In the practical application, the environment is very complicated. Therefore, future research could focus on improving the mechanical properties of the material, which can improve the durability of the material.

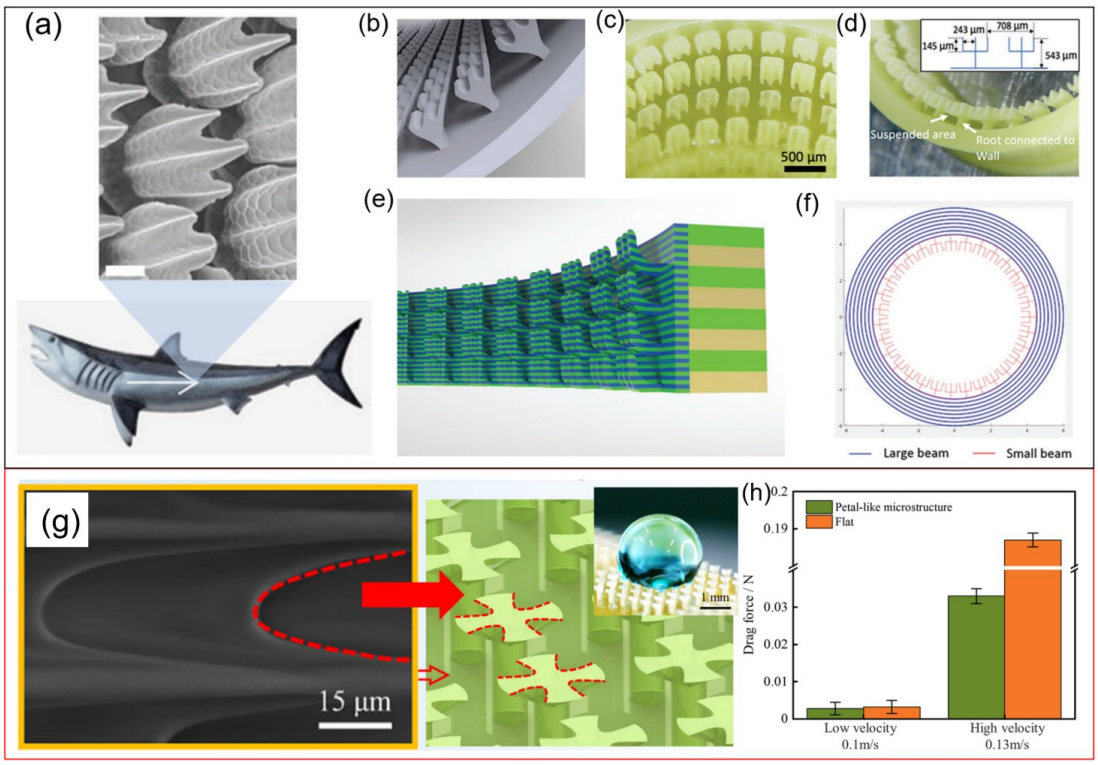

Figure 3.12 ***a*** *SEM image of shark skin with denticles covered by micro riblets [221,222];* ***b*** *3D model of denticles;* ***c*** *Surface and* ***d*** *cross-section of 3D-printing shark skin-like structure;* ***e*** *Schematic of multiscale 3D-printing, different color means different layers to printing;* ***f*** *View of*

cross-section for 3D-printing with different resolution [162]; ***g*** *Special surface microstructure inspired by nepenthes and h its' drag reduction performance [225].*

3.6.4 4D-printing

Mimosa pudica, a smart plant originates from South American, will bend its foliage to protect itself when stimulate by external environment. The variation of the cytoderm permeability which influenced by the external stimulus induced asymmetrical swelling could explain this intriguing phenomenon [226]. Smart material that could respond to variation of external environment such as magnetic field, temperature, humidity and etc. were named actuators which have been widely used in the fields of artificial organs [227], soft robot [228], soft grippers [229], etc.

A paper-based Janus actuator with opposite wettability that could be dynamically driven by water adsorption was demonstrated by Liu et al [226]. The conjunction of PDMS and candle soot enable the material with stable super-hydrophobicity which will lead to inhomogeneous swelling while immersing the actuator in water. The Janus-paper has promising applications in the fields of microdroplet transportation and water storage. 4D-printing, an innovative research division generated from 3D-printing combined with time dimension which is a promising technology for the fabrication of smart stimulation-respond actuator. With 4D-printing technology, actuators with more complicated structure and versatile deformation behavior such as bending, elongating, twisting, and corrugating could be fabricated. Meanwhile, intricate and high-cost procedures could be avoided. Zhao and co-workers reported a hydrophobic/hydrophilic hybrid shape-shifting actuator fabricated by DLP technique [230]. The mismatch bilayer structure consists of hydrophilic poly (ethylene glycol) diacrylate (PEGDA) and hydrophobic poly (propylene glycol) dimethacrylate (PPGDMA) could achieve noninotropic swelling underwater. Compared with traditional hydrogel actuators, PEGDA, which is an elastomer with high crosslinking density, owns a faster actuation time and higher actuation force because of lower equilibrium swelling ratio and higher rubbery modules. Figure 3-13a illustrates the printing process of the actuator. First, liquid PEGDA resin was filled between hydrophilic glass and hydrophobic glass and illuminated by the light pattern. Following the photocuring process, PEGDA will stick on the hydrophilic glass and two glass slides with photocured PEGDA have been utilized as a model for liquid PPGDMA resin. The final product could be obtained after illumination of the composite of PEGDA and PPGDMA. On the condition of identical full layer thickness, curvature and actuation time could be influenced by the thickness of the PEGDA layer. Considering this, sequential deformation actuator could be

fabricated with grayscale image induced different PEGDA layer thickness. As shown in Figure 3-12b& c, a strip and a flower shape actuator were fabricated with sequential water-respond ability. The bilayer contains a higher thickness of PEGDA will have a high deformation speed and larger final curvature. Considering the advantages of DLP technique, customized shape could be fabricated and applicate in promising future.

4D-printing has a very broad application prospect. But currently there is only one 4D-printing work based on wettability. Therefore, more research should focus on this field to make more complex and interesting structures by 4D-printing.

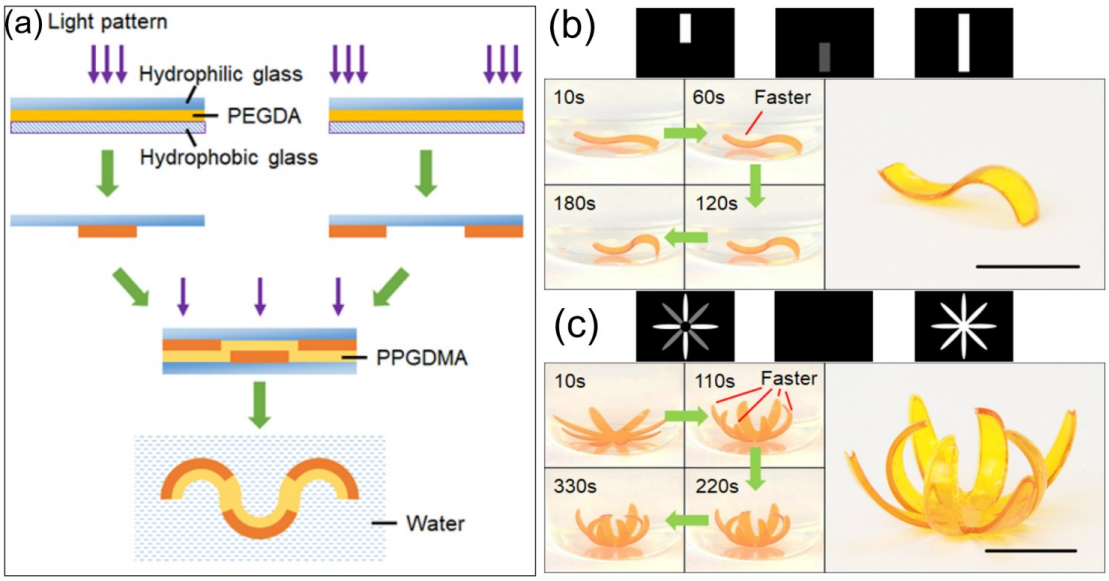

Figure 3.13 ***a*** *Fabrication process of shape-shifting actuator;* ***b*** *Strip and* ***c*** *flower shape actuator with sequential water response ability [230]. (Scale bar: 10 mm.)*

In general, compared to traditional manufacturing methods, 3D printing has three main advantages. Firstly, 3D printing could replicate known structures from the natural. Secondly, 3D printing allows for convenient fabrication of the customized 3D structure based on user requirements. Lastly, the 3D printing process reduces the consumption of human resources, resulting in more efficient manufacturing.

3.7 Conclusions and perspectives

To promote the field advancement of the hydrophobic material fabricated by 3D-printing, fundamental theory of wettability, mechanism of diverse 3D-printing techniques, methods to gain hydrophobicity and bioinspired applications are systematically reviewed here. Despite the various

raw materials and printing strategy, a shared printing procedure was demonstrated which consists of raw material preparation, model design, printing process and after printing process. Facing the challenge to achieve hydrophobicity, methods in each process were discussed. For some 3D-printing techniques with high feature resolution, nano scale roughness could be gained directly with a designed model. Adding hydrophobic fillers, magnetic driven method, coating and modeling could also benefit the fabrication of hydrophobic surface. Inspired by the hydrophobic phenomena in nature, applications including drag reduction, water harvesting, oil-water separation and 4D-printing were reviewed from fundamental theory to practical application. An outlook for promoting advancement in the field on fabrication of hydrophobic materials via 3D-printing could be demonstrated as follows:

(1) Most of the theoretical models are based on the ideal situation including a flat surface and a motionless droplet. However, inclined or parallel surfaces which could be easily fabricated via 3D-printing are not rare in practical applications. Considering this, future research should be focus on the dynamic models of the droplet's movement.

(2) Although achieving hydrophobicity remains challenge, it is necessary to find methods which is simple and low-cost. New 3D-printer with higher feature resolution could be used to reduce the additional cost on building nano-scale roughness. Some evitable procedures such as modeling, leaching and coating could be avoided. Furthermore, the related research content should be open access, which is beneficial for the advancement and progress of this field.

(3) The fabricated material should be designed to fully utilize using the advantages of 3D-printing. For example, in the field of oil-water separation. Many methods have been reported to fabricate 2D membrane for filtration. However, this kind of equipment could only separate oil which owns a higher density than water. Besides, it will consume more energy for the collection of oil-water mixture. With 3D-printing technique, the filter could be built as a 3D collector which could float on the water surface and separate oil automatically. In the future, highly customized 3D model should be designed to improve the performance of the material.

(4) Research should focus on the application. Many reported materials only focus on the improvement of hydrophobicity but ignore the importance of practical applications which will promote the development of the field. Besides, research toward more applications should be developed. For example, Janus structure has wide applications and 3D-printing is a promising

technique to fabricate Janus structure because it could easily control the distribution of hydrophilic part.

3.8 Link to Experimental Chapters

The gaps identified in this review directly inform the experimental strategy adopted in this thesis. First, existing studies frequently rely on complex or multi-step approaches—such as solvent-rich ink formulations, sacrificial templating, plasma modification, or multi-layer coatings—to achieve hydrophobicity. These processes increase cost, environmental burden, and limit industrial scalability. This motivates the development of simplified and environmentally responsible fabrication routes capable of producing robust hydrophobic surfaces without extensive chemical treatments. Second, although 3D printing inherently enables the construction of fully three-dimensional architectures, most reported works restrict their designs to 2D membranes or planar samples, failing to exploit the unique geometrical freedom that could enhance capillarity control, fluid routing, and continuous oil–water separation performance. This thesis therefore aims to explore structurally optimized 3D porous designs and evaluate their functional benefits beyond those achievable with traditional membrane-like formats.

These two research gaps shape the direction of the experimental chapters. Chapter 4 investigates a simplified FFF-based strategy for constructing hydrophobic porous PLA membranes using minimal post-processing, thereby addressing the need for fabrication routes that are both practical and scalable. Chapter 5 extends the concept to fully 3D printed architectures with controlled pore geometry, illustrating how structural design can be explicitly leveraged to tune wetting behavior and continues separation efficiency.

Chapter 4: Simplified 3D Printing Method for Fabrication of Superhydrophobic Oil-Water Separation Membrane with Controllable Pore Size

4.1 Introduction to the Chapter

This chapter presents a published research article entitled *"Fabrication of Superhydrophobic Poly (lactic acid) Porous Membrane via 3D Printing with Tunable Pore Size for Oil–Water Separation"*, published in **Journal of Applied Polymer Science**. The highlight of this study is a simplified, model-free strategy based on fused filament fabrication (FFF), in which porous PLA membranes are fabricated by directly adjusting the infill density parameter in slicing software to control the pore size.

As the first experimental study in this thesis, this chapter is designed based on the fabrication methods and application directions of 3D-printed oil–water separation materials reviewed in Chapter 3 and lays the groundwork for the development of more complex structures and enhanced separation performance explored in Chapter 5.

4.2 Introduction

In the face of the persistent challenge posed by the frequent discharge of oily wastewater and industrial oil leaks resulting from human activities in recent years, the separation and purification of oil/water mixtures have emerged as critical components for sustainable development [231,232].However, conventional separation methods, such as biological treatment [205] and burning [206], are not only costly but also inefficient, leading to significant energy consumption. Consequently, there is an urgent imperative for the development of novel, highly efficient, and cost-effective approaches to address this pressing issue and meet the practical demands of the industry. Over the past two decades, biomimetic hydrophobic materials, including aerogels [207], foam [66,94], microspheres [208] and membranes [104], have been developed for oil/water separation, offering several notable advantages over conventional techniques such as enhanced flux rates, elevated separation efficiencies, and reduced energy consumption, attributed to their hydrophobic surfaces selectively blocking water while allowing oil to pass through [50,233].

According to their separation mechanisms, these materials are typically categorized into two types. The first type is adsorptive, such as aerogels, foam, and microspheres, which achieve oil/water separation by adsorbing oils into their internal structures [234]. The second type is filtrate, such as membranes, which separate oil and water by allowing oil to pass through under gravity while blocking water [235].

While adsorptive oil/water separation materials like aerogels and monoliths are good candidates, additional techniques such as centrifugation and squeezing are necessary to recover the adsorbed oil, resulting in relatively lower recovery efficiency [236,237]. Among the various hydrophobic materials utilized in treating oily wastewater, membranes hold promising prospects for practical application [104]. However, the reported membranes used for oil/water separation are frequently associated with non-degradable materials [209], leading to environmental issues, complex fabrication processes which need the additional support from model design software [204], and high raw material costs, thereby hindering widespread industrial fabrication. Additionally, these membranes present challenges in designing membrane structures and controlling pore sizes.

The rapidly developing Additive Manufacturing (AM) or 3D printing technology is viewed as a revolutionary method for designing and creating structures due to its unmatched versatility, flexibility, and customization capabilities [238,239]. AM relies on the sequential layer-by-layer deposition of material, enabling the fabrication of complex structures with fewer geometrical constraints [240]. This technology can be effectively utilized to produce polymer membranes. Despite its significant potential, research on fabricating oil/water separation using 3D printing remains relatively limited. Upon reviewing relevant literature, three main issues were identified in previous studies. Firstly, most materials are completely non-biodegradable, which negatively impacts ecological and environmental protection [66]. Secondly, as shown in Figure 4-1, complex models typically need to be prepared before printing in prior work. In prior work, the before printing the model design is inevitable which significantly increases the time cost of adjusting the pore size []. Lastly, the superhydrophobic modification in many processes is highly complex and requires multiple raw materials, limiting large-scale production.

Among the various 3D printing systems, Fused Filament Fabrication (FFF) is one of the most cost-effective, widely applicable, easy-to-operate technologies and offers the possibility to use biodegradable and bio sourced materials.[22] However, although the advantages of the FFF

process are numerous, there remains a significant obstacle to the widespread use of this technique, namely the directly fabricating from micro- and nanoscale structures. Indeed, for FFF, Polylactide acid (PLA) is one of the most used materials due to its stability, good mechanical properties, biodegradability, and affordability [241]. Other filaments also possess favorable mechanical properties, but their poor printability and limited commercial availability restrict their use in practical FFF applications. Therefore, PLA represents the most feasible option for scalable, efficient membrane fabrication using this method.

Compared with conventional oil-water separation methods such as sponge adsorption, flotation, or combustion, the use of superhydrophobic membranes provides selective filtration. This significantly enhances efficiency. Furthermore, the FFF-based fabrication strategy enables scalable and cost-effective production, as membrane dimensions and pore sizes can be rapidly customized without complex modeling. From an environmental perspective, the use of biodegradable PLA and the avoidance of secondary pollution further contribute to the sustainability of this approach. Here, we prepared PLA membranes with different pore sizes using FFF 3D printing technology by controlling the infill density in the slicer software. As shown in Figure 4-1, this approach eliminates the model design step, enhancing manufacturing efficiency. Compared to samples fabricated using modeling, the higher accuracy of the pore size is readily apparent [204]. The method in this work could achieve a minimum pore size of 313.02 micrometers. The entire process does not require complex modeling, and pore size changes can be made with just a few simple clicks in the software. Subsequently, a superhydrophobic coating with a contact angle of up to 154.64° was applied to the membrane surface using a simple spraying method. Based on the membrane's superhydrophobicity, the samples can be used for oil-water separation. When separating dichloromethane, the flux reached 81.89 ml cm-2 min-1, maintaining a separation efficiency of over 90%.

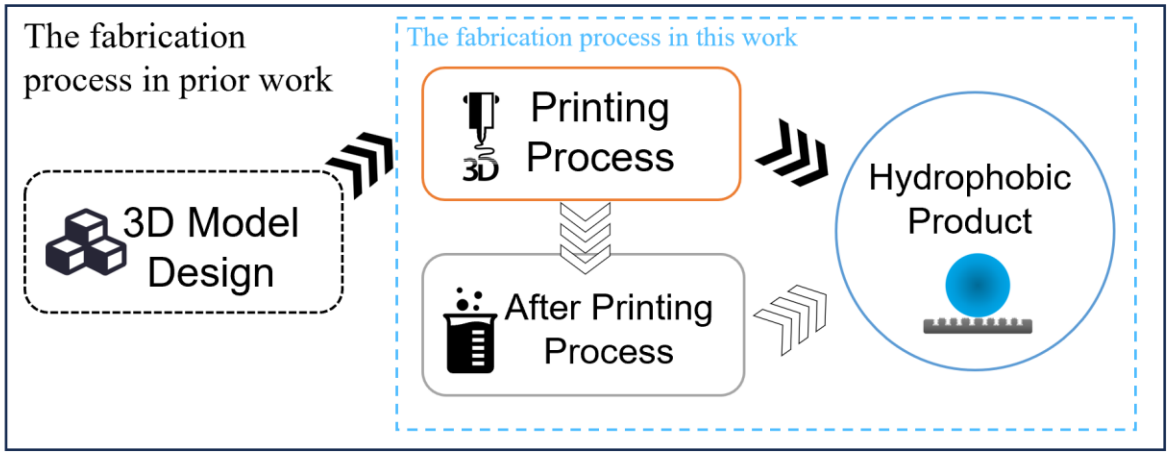

Figure 4.1 Comparison of the fabrication processes between prior work and this work.

4.3 Material and methods

4.3.1 Material

The Filament used is PLA (Raise Premium 1.75 mm PLA filament). PDMS and the curing agent were purchased from Dow Corning Co. Ltd Shanghai, China. Silica nanoparticles were purchased from Lanling Chemical Co. Ltd Foshan, China. Ethanol, Isopropanol and other solvent were purchased from Zhiyuan Reagent Co. Ltd Tianjin, China. All materials were used as received.

4.3.2 Fabrication of 2D PLA porous membrane

The 3D printer used is a commercial dual extruder FDM machine Ender-3 S1. The model was built directly in the slicer software PrusaSlicer 2.60. First, as shown in Figure 4-2a, basic function of slicer was used to build a cylinder with a diameter of 50mm and a height of 1mm. Also illustrated in Figure 4-2a, different infill percentages were set and printed to obtain PLA membranes with different pore sizes. (Grid is selected as the Infill pattern). More detailed printing parameters are shown in Table 4-1. The relevant printing parameters are the default parameters of the printer for this filament type. All printing parameters were selected based on the recommendations provided by the slicer software, which considers the specific printer and filament used. For example, the printing time for sample M90 was approximately 23 minutes using the default normal mode settings. In this work, we employed the parameters recommended for normal mode. The fast mode was not selected due to its potential to reduce printing accuracy, while the high-precision mode was also excluded as it would compromise printing efficiency.

Table 4-1 Parameter for the printing PLA membrane

Sample	Infill percentage (%)	Printing speed (mm s^{-1})	Nozzle temperature (°C)	Layer height (mm)
M60	60	30	215	0.2
M70	70	30	215	0.2
M80	80	30	215	0.2
M90	90	30	215	0.2
M95	95	30	215	0.2

4.3.3 Modification of PLA membrane

We designed simple post-treatments for the printed sample and the process was illustrated in Figure 4-3c. First, 0.3 g of silica nano-particles and 10 ml of isopropanol were introduced into 10 ml of ethanol, followed by a 15 min ultrasonic treatment. Silica nanoparticles could provide nano-level roughness and PDMS could connect particles and the membrane. Subsequently, 0.07 g of PDMS and 0.007g curing agent were added to the solution, and the resulting mixture underwent a 30 min ultrasonic treatment to achieve a homogeneous solution. For the spray-coating method, the homogeneous solution was injected into a commercial spray gun. It was then sprayed from a height of approximately 20 cm above the sample at a pressure of 0.2 MPa. During the spraying process, During the spray-coating step, the spray gun was moved laterally at a controlled speed of approximately 5–10 mm/s, and a certain number of cycles (0-20 cycles) were performed. Subsequently, the sample was also placed in a fume hood for over eight hours to ensure the complete evaporation of ethanol.

4.3.4 Characterizations

Contact angles were measured using a contact angle goniometer (SL200KS, KINO, USA) at ambient temperature. The droplet volume utilized for the measurements was 2.5 μL. Scanning electron microscope images of the PLA membrane were acquired with a Hitachi S-4800 operating at 20 kV. Surface structure and EDS mapping of membranes were characterized using a scanning electron microscopy (SEM, 400FEG, America). The pore size was calculated with the support of Nano Measurer software. For each membrane, SEM images were taken at three randomly selected regions. In each region, five pores were measured, yielding 15 data points per sample.

4.3.5 Oil filtration test

In this part of the experiment, samples were placed in a laboratory-made filter device to achieve oil-water separation driven by gravity. Low density solvent used here to represent a low-viscosity polar organic solvent not separation from water.

The separation flux was calculated according to the followed equation:

$$flux = \frac{V}{St} \quad (4-1)$$

where V represents the volume of separated organic solvent, S represents the surface area of membrane, and t is the separation time.

The separation efficiency was calculated as the following equation:

$$flux = \frac{m}{M} \quad (4-2)$$

where M and m represent the weight organic solvent before and after the separation process, respectively.

4.4 Result and discussion

4.4.1 Fabrication of 2D PLA porous membrane

To better study the fabrication process of 3D-printed hydrophobic materials, the theoretical background for constructing superhydrophobic surfaces should be investigated. The contact angle (CA) of the liquid phase on the solid surface are the key indicators to characterize the wettability of the solid surface. The larger the contact angle, the better the hydrophobicity of the material surface. In summary of the wetting theory developed by Wenzel [106] and Cassie [107], existence of low surface energy of intrinsic surface chemical component basal is pivotal for hydrophobicity and micro-nano hybrid micro morphology will achieve synergistic action which greatly improve hydrophobicity.

In this work, we aim to fabricate superhydrophobic oil-water separation material via FFF technology. There are two most important advantages of FFF technology. First, FFF is one of the most cost-effective and widely used 3D printing techniques, making it accessible for large-scale production. Second, biodegradable and eco-friendly PLA filaments can be utilized with FFF technology and the PLA waste generated during printing has high recycling value. The disadvantages of FFF technology in the preparation of hydrophobic materials are also evident. Most importantly, its low resolution makes it incapable of directly fabricating micro- and nanoscale structures.

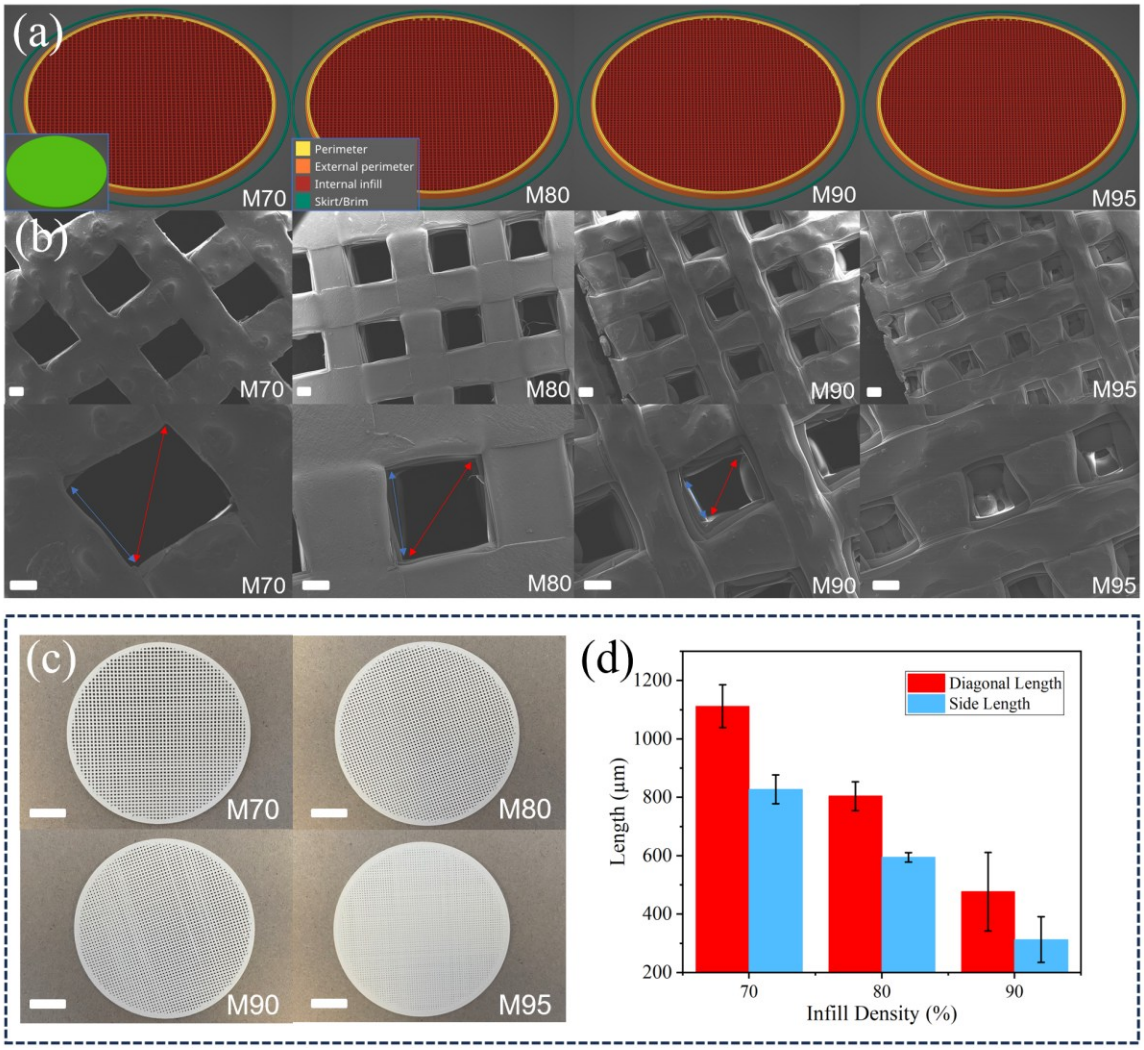

Figure 4.2 ***a*** *Model building and slicing process of PLA membrane with different infill percentage.* ***b*** *SEM images (Scale bar is 200 μm),* ***c*** *digital photograph and* ***d*** *pore size distribution graph of samples with different infill percentage (Scale bar is 1 cm). d Pore size distribution of different samples.*

In previously reported work, model design is typically an indispensable step in the fabrication of hydrophobic materials via 3D printing. However, constructing models for oil-water separation materials with extensive pore structures requires significant computational graphic power; otherwise, it becomes a time-consuming process. Additionally, adjusting the pore size of the samples necessitates re-modelling. Therefore, it is essential to find optimized methods for the model design step. As shown in Figure 4-2a, it was observed that constructing cylindrical shapes in Slicer software and subsequently adjusting infill percentage and infill pattern settings enables the fabrication of porous PLA membranes with varying pore sizes and shapes. Although this method enables the fabrication of porous membranes with various pore shapes, such as triangles

and stars, in this study, we will exclusively employ the grid infill pattern due to its better regularity. In this study, preliminary tests revealed that the infill density has a direct and systematic influence on the resulting pore size of the printed membranes. Therefore, infill density was selected as the primary experimental variable for exploratory investigation into pore-size control. To ensure that the observed effects could be exclusively attributed to this parameter, all other printing conditions—such as nozzle temperature, print speed, and layer height—were kept constant.

The specific printing parameters used in this work were chosen according to the recommendations provided by the slicer software for the selected printer–filament combination. These recommended settings represent optimized values that ensure stable extrusion quality, sufficient interlayer adhesion, and reproducible printing performance. Maintaining these parameters across all samples minimizes unintended variability and allows a controlled assessment of how infill density alone affects the microstructure of the membrane.

Figure 4-2b shows the SEM images of M70, M80, M90 and M95. It is evident that with the increase in infill percentage, the pore size of the PLA membrane gradually decreases. When the infill percentage reaches 95%, the pore structure is no longer through-holes, thus subsequent statistical analysis is not conducted on M95. There are two reasons for the occurrence of non-through holes. Firstly, when PLA leaves the nozzle at 215°C, its temperature is higher than the glass transition temperature. At semi-solid state, PLA may deform under gravity and thus clogging the pore structure to some extent. Additionally, when the pore size is small, FFF printers may not be able to precisely control nozzle movement. Compared with previous studies, the pore size deviation of our samples is visibly smaller in the SEM images [204], with a maximum variation of less than 78.2 μm. Figure 4-2d shows the pore size distribution of different samples. The average Diagonal Length of M70, M80 and M90 is 1112.23 μm, 804.29 μm and 476.86 μm, respectively. The average Side Length of M70, M80 and M90 is 827.53 μm, 594.79 μm and 313.02 μm, respectively. Compared to M70 and M80, M90 shows a larger pore size variation due to the precision limitations of FFF technology. Figure 4-2c shows the digital photographs of M70, M80, M90, and M95. It can be observed that the pore size decreases with increasing infill percentage, and the printed samples exhibit no significant defects. Other porous materials for oil-water separation can achieve smaller pore sizes—for example, phase separation methods can produce pores in the range of 5–50 nm.[6] However, such materials often contain additional micro-sized macropores, resulting in a broad pore size distribution, lack of uniformity, and limited

controllability. Therefore, they do not offer a clear advantage over 3D printing in terms of industrial-scale standardized production.

Pore size and shape are critical parameters for oil-water separation. However, previous literature lacks studies on the impact of them on the oil-water separation process and its theoretical basis. The phenomenon of water blocking on superhydrophobic porous surfaces can be explained by the invasion pressure theory [242]:

$$\Delta P = \frac{2\gamma_{LV}}{R} = -\frac{C\gamma_{LV}\cos\theta}{A} \qquad (4-3)$$

As shown in Figure 4-3a and 3b, the interfacial tension between the liquid (whether water or oil) and air is denoted as γ_{LV}. The contact angle of water or oil on the solid hydrophobic surface is represented by θ. The radius of the curved meniscus is denoted as R. C represents the perimeter of the mesh with a rough structure. A represents the cross-sectional area of the mesh. As illustrated in the equations, it can be inferred that when the water contact angle (θ) is larger than 90°, ΔP will be larger than 0. Consequently, for porous hydrophobic materials, there is a negative capillary effect on water, impeding its penetration. For oleophilic surfaces, the contact angle of oil is less than 90°, resulting in a ΔP less than 0. Therefore, based on capillary forces, oil can traverse the surface. This selective permeability is mainly determined by the surface energy contrast between oil and water. Since most oils have significantly lower surface energy than water, they tend to be absorbed or pass through the superhydrophobic and superoleophilic membrane. Therefore, the membrane exhibits intrinsic selectivity based on interfacial energy differences rather than viscosity or density.

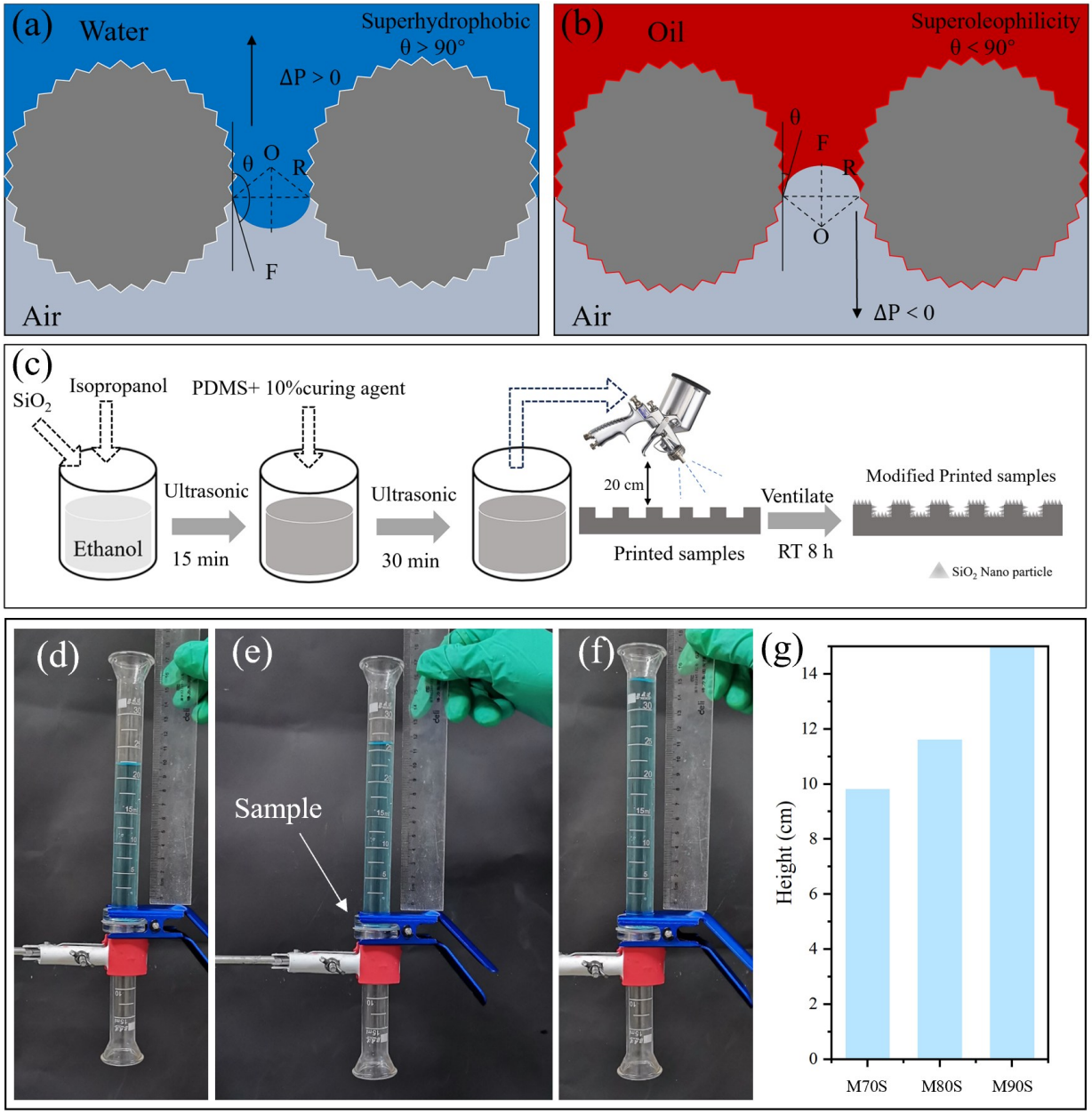

Figure 4.3 ***a*** *The mesh exhibited superhydrophobic characteristics with a positive pressure differential (ΔP > 0), preventing the passage of water through its structure.* ***b*** *Conversely, the mesh demonstrated superoleophilic properties with a negative pressure differential (ΔP < 0), allowing for permeability to oil. Here, O represents the center of the spherical cap of the meniscus, and R signifies the radius of curvature of the spherical cap of the meniscus.* ***c*** *Water Pressure Resistance of Membranes:* ***d*** *M70S,* ***e*** *M80S and* ***f*** *M90S.* ***g*** *Water-blocking height (cm).*

In this work, all pore sizes can be approximated as squares. Let the side length of the square be denoted as a. The formula can be further derived as follows:

$$\Delta P = -\frac{C\gamma_{LV}\cos\theta}{A} = -\frac{4a\gamma_{LV}\cos\theta}{a^2} = -\frac{4\gamma_{LV}\cos\theta}{a} \qquad (4-4)$$

From the formula, we can observe that the negative capillary force exerted on water by the porous hydrophobic surface is inversely proportional to the pore size. Therefore, pore size is a crucial parameter for oil-water separation materials. For instance, when facing high water pressure in deep-water applications, reducing the pore size appropriately can enhance the negative capillary force.

4.4.2 Hydrophobic post-treatment

As illustrated in Figure 4-3c, we explored spray coating methods to enhance the hydrophobicity of the samples. During the solution preparation stage, the addition of isopropanol was found to enhance the dispersibility of nano-silica in ethanol. Nano-silica itself exhibits inherently low surface energy and, due to its small scale, can simultaneously reduce material surface energy while augmenting surface roughness. Post-curing, PDMS can adhere to both nano-silica particles and the material surface, leveraging its own low surface energy to further enhance material hydrophobicity [243].

The nano-coating method is not environmentally friendly; however, it is more cost-effective and simpler to implement. Given the established formulation of the nano-silica solution in the literature [243], this study primarily discusses the influence of spray cycles on hydrophobicity. A spraying pressure of 0.2 MPa was selected because it produces a stable and uniform atomization of the silica–PDMS dispersion, ensuring consistent nanoparticle deposition on the porous surfaces. This pressure falls within the recommended operating pressure provided in the spray-gun manufacturer's technical guidelines. As depicted in Figure 4-4a, before modification, the WCAs of M70, M80, and M90 were 104.24°, 107.83°, and 108.90°, respectively. After 20 spray cycles, the WCAs increased to 155.71°, 158.10°, and 154.64°, respectively. For all samples, the contact angle gradually increases with an increase in spray cycles, reaching a plateau beyond 20 cycles, indicating saturation. Consequently, in subsequent work, our spray coating was limited to 20 cycles. The sample after coating are named as M70S, M80S and M90S. As shown in Figures 4-3d-f, the water blocking capability of the PLA membrane increases by decreasing pore size, consistent with our predictions based on invasion pressure theory. As shown in Figure 4-3g, M70S could block 9.8 cm of water and 11.6 cm for M80S. Specifically, the M90S membrane can block a water column exceeding 15.1 cm (limited by the testing apparatus). Therefore, it has the potential to operate under the water pressure corresponding to a 15.1 cm water column. Figure 4-4b and 4c

illustrate the water contact angle (154.64°) and the oil contact angle (0°) of sample M90S, respectively, confirming its superhydrophobic and superoleophilic property. Figure 4-4d showcases the phenomenon of water droplets sliding off the sample surface, attributed to its low adhesion resulting from superhydrophobicity. Figure 4-4e demonstrates the silver mirror effect observed when the sample is submerged in water, attributed to the capture of air on the surface of the superhydrophobic sample upon immersion, causing the formation of bubbles with different refractive indices from water, thus producing this distinctive phenomenon [244]. Figure 4-4f and g depict the SEM images of M90 before and M90S, respectively. It's evident from these images that the surface of M90S exhibits nano-sized particles, which are the primary reason for the enhanced hydrophobicity of M90S.

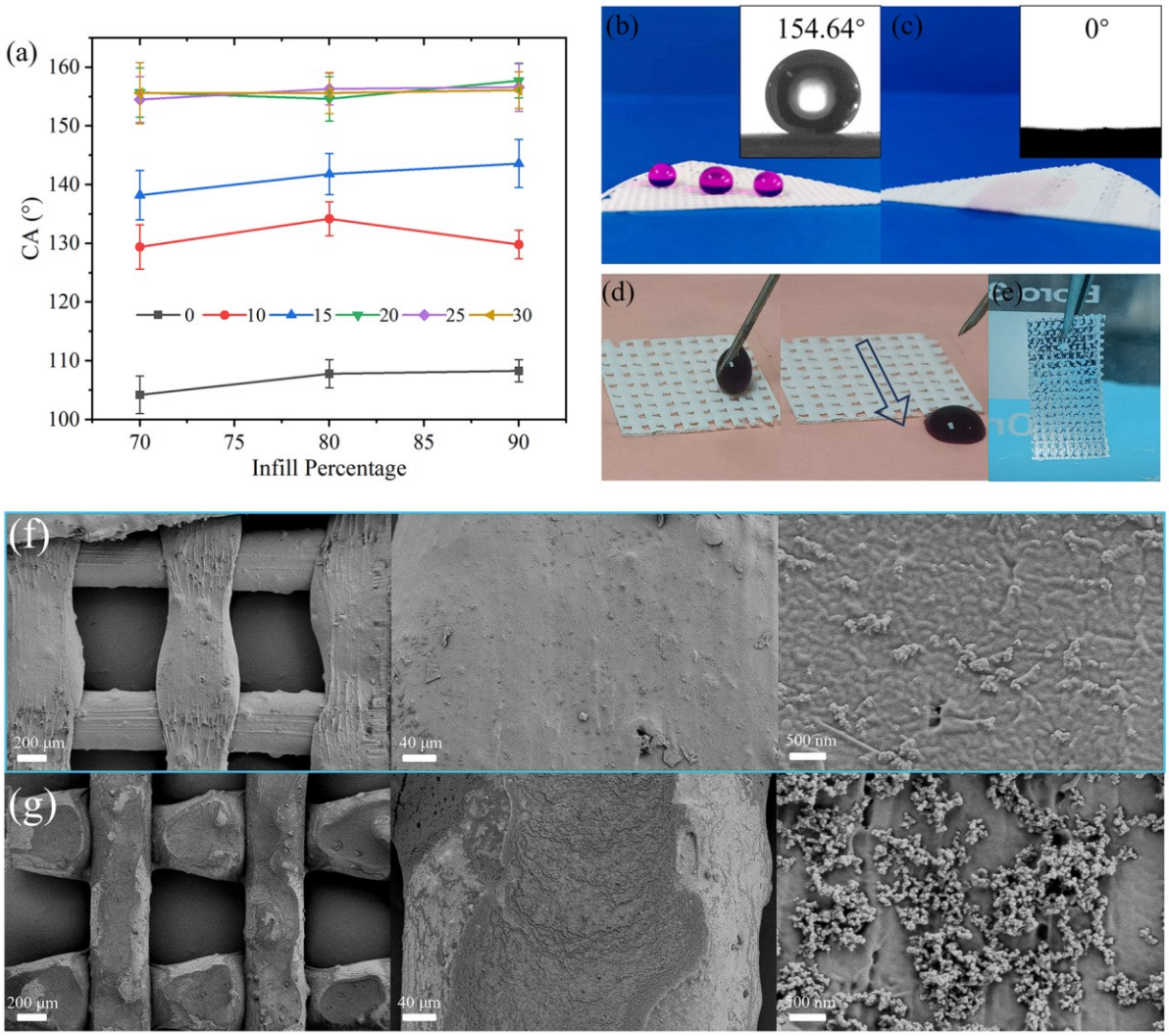

Figure 4.4 ***a*** *Contact angle of samples with different infill percentage and spray cycles. Digital photography of M90 and* ***b*** *its water contact angle and* ***c*** *oil contact angle (hexadecane). The phenomena of* ***d*** *water droplet sliding and* ***e*** *the silver mirror effect. SEM images of* ***f*** *M90 and* ***g*** *M90S.*

Figure 4-5a and b show the changes in the M90 and M90S after immersion in water. It is apparent that the surface of the M90S remains clean with no water adhesion. In contrast, the M90 surface absorbs water, which has been stained with potassium permanganate. Figure 4-5c presents the mass changes of the samples over 10 cycles. It can be observed that the mass of the modified sample M90S remains constant, whereas the mass of the original sample M90 increases due to water absorption. Figure 4-5d presents the results of the water impact experiment. After 10 cycles of water impact at 20 cm/s, M90S maintains its superhydrophobicity with a contact angle of 154.72°. Figure 4-5e shows the contact angle of M90S during the tape peeling experiment. It was

found that the peeling process did not cause a significant decrease in the contact angle. After 10 peeling cycles, the contact angle of the M90S was 151.27°. This result indicates that while the peeling process does damage the nano-silica coating on the surface to some extent, the damage is limited. Figure 4-5f illustrates the changes in the contact angle of the sample under different pH conditions. It can be observed that the hydrophobicity of the sample is maintained in both strong acidic and strong alkaline environments.

Among the modified membranes, M90S was selected as the representative sample for durability evaluation, including tape-peeling, pH stability, and water-impact tests. M90S exhibits the smallest controllable pore size and the highest water-blocking performance, making it the most functionally demanding configuration within this series. Testing the durability of the most restrictive and performance-critical membrane provides a conservative assessment of the coating stability and ensures that the conclusions drawn are representative of the membrane with the strongest capillary barrier. Therefore, M90S was chosen as the reference sample for durability studies, while the other samples mainly serve to illustrate the tunability of pore size and flux.

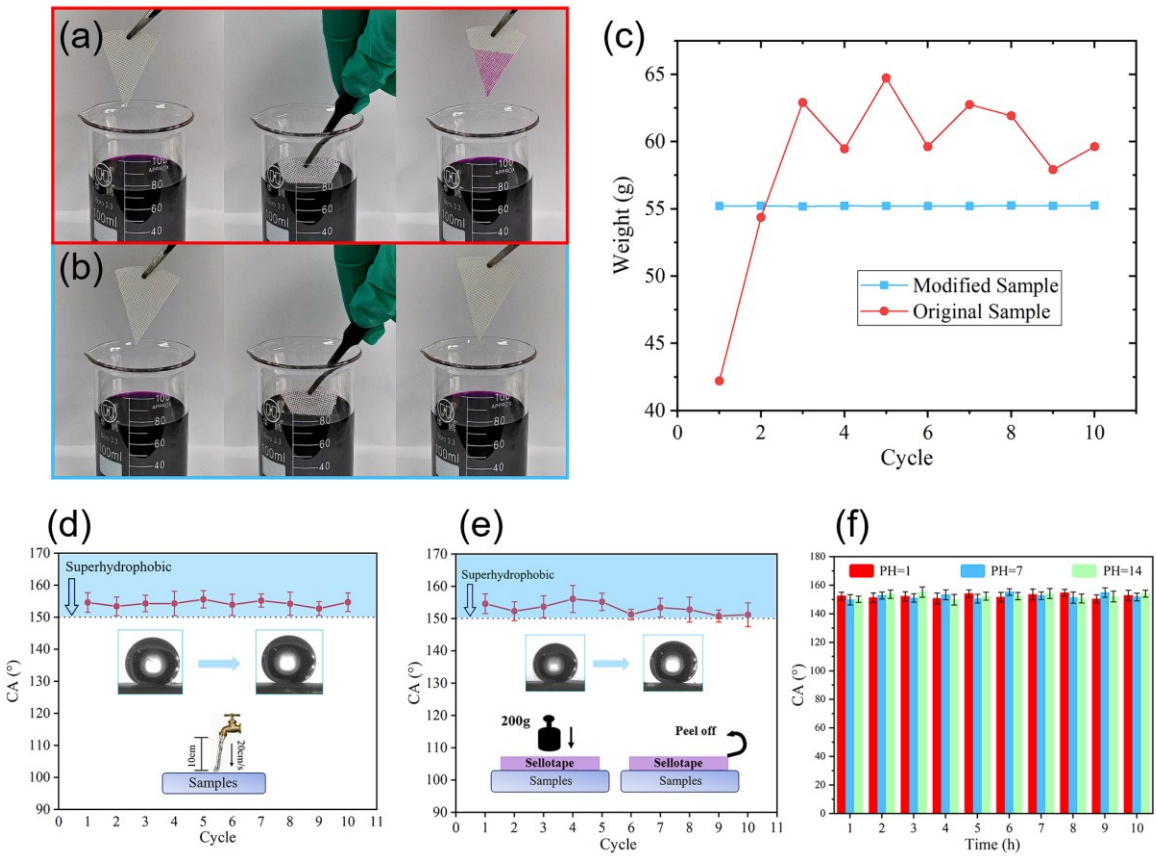

*Figure 4.5 Water absorption of **a** M90 and **b** M90S, **c** Mass increase of different samples. Contact angle of M90S in **d** water impact test and **e** tape peeling test. **f** Contact angle of M90S in different time periods and pH levels.*

4.4.3 Oil-water separation experiment

Based on the invasion pressure theory, the modified PLA membrane generates reverse capillary forces to block water passage, thus enabling selective oil-water separation. Figure 4-6a demonstrates the separation process of water (dyed with methylene blue) and dichloromethane (dyed with Sudan III) using M90S in a custom laboratory setup. It can be observed that M90S blocks water while selectively allowing dichloromethane to pass through. Figure 4-6b shows the flux of M70S, M80S, and M90S for different oils. As predicted, M90S, with its smaller pore size, has the lowest flux. For dichloromethane, the flux of M90S is 67.44 ml cm-2 min-1. M70S, with larger pores, exhibits the highest flux, with a flux of 81.89 ml cm-2 min-1 for dichloromethane. According to the discussion of Han [209], the flux is good compared with other hydrophobic membrane. These results highlight the importance of controlling membrane pore size. For oil-water separation under low-pressure conditions, larger pore sizes should be printed to increase flux.

Conversely, smaller pore sizes should be used to prevent water passage under higher pressure conditions. The varying flux for different oils is attributed to differences in their densities and viscosities. Figure 4-6c shows the separation efficiency of M70S, M80S, and M90S for different oils. There is no clear correlation between separation efficiency and pore size. The separation efficiency of M80S for n-hexane is the lowest at 83.05%. M70S achieves a separation efficiency of 94% for ethanol. The separation efficiency cannot reach 100% because some oil is retained by the membrane itself during the separation process, which is also dependent on the density and viscosity of the oil. In our experiments, separation efficiency did not exhibit a direct correlation with pore size. Beyond experimental uncertainty, two additional factors contributed to oil loss during the separation process, both of which are essentially independent of pore geometry. First, partial emulsification occurs during handling and pouring of the oil–water mixture, producing fine droplets that are difficult to fully recover regardless of membrane pore size. Second, due to capillary-driven adsorption, a fraction of the oil is retained on the modified membrane surface rather than within the pore channels. This surface-level adsorption arises from the superoleophilic nature of the coating and contributes to measurable mass loss in all samples. Because neither emulsification nor surface adsorption is significantly affected by pore diameter, the separation efficiency remains relatively insensitive to changes in pore size.

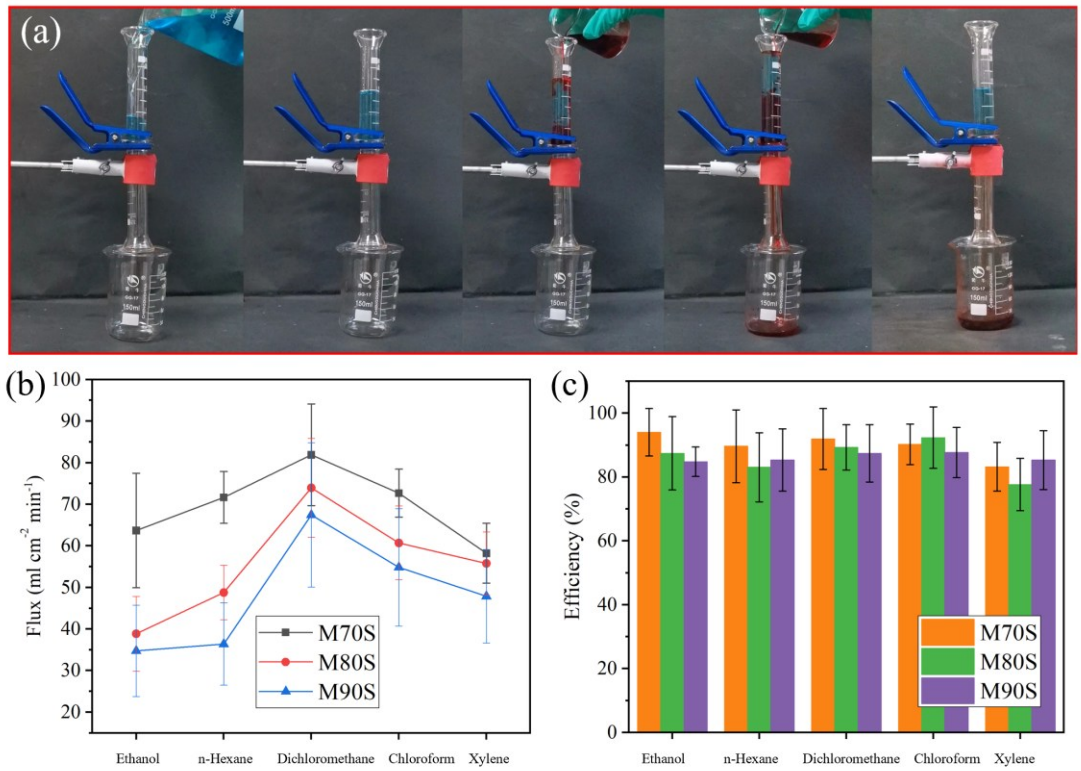

Figure 4.6 ***a*** *Dichloromethane -water separation process by M90S.* ***b*** *Flux of different samples and oils.* ***c*** *Separation efficiency for different oils.*

4.5 Conclusion

This study enabled the fabrication of model-free porous PLA membranes with controllable pore sizes by adjusting the infill percentage. The smallest pore side length could reach 313.02 µm. Using a simple spray coating method, the contact angle of the membrane reached 154.64°. Based on varying infill percentages, the membrane could block water columns exceeding 15.1 cm, demonstrating its potential for operation under such water pressure. The superhydrophobicity of the samples was maintained after 10 cycles of peeling and water impact tests and remained stable across different pH levels. The membranes successfully performed oil-water separation, achieving a maximum flux of 81.89 ml cm^{-2} min^{-1} for dichloromethane. In practical applications, adjusting the pore size of the membrane based on the anticipated water pressure it will encounter can enhance flux significantly. Separation efficiency remained above 83.05% across different oils.

In this work we have proposed for the first time the additive manufacturing of 3D parts with a simple biodegradable shape and with easily modifiable dimensions and shape parameters. In the future, further research should focus on the feasibility of 3D printing more complex structures for

oil-water separation devices. Additionally, exploring the feasibility of more environmentally friendly methods for hydrophobic modification is warranted.

In future work, we aim to conduct extended-duration experiments under realistic operational conditions to further assess the long-term stability of the membrane system. Optimizing the fabrication process, particularly the surface modification step, and enhancing overall sustainability will also remain key focuses of our research.

Chapter 5: Innovative 3D-Printed Superhydrophobic Porous Architectures for Continuous Oil-Water Separation

5.1 Introduction to the Chapter

This chapter presents a research article published on **Polymers**, entitled *"Innovative 3D-Printed Superhydrophobic Porous Architectures for Continuous Oil–Water Separation".* In Chapter 4, although a simplified strategy was proposed for fabricating oil–water separation membranes, the structures remained essentially two-dimensional. In the present work, we designed and fabricated three-dimensional PLA porous structures with controllable rhombic pores using fused filament fabrication (FFF) technology.

Unlike the membrane-based, batch-mode separation demonstrated in the previous chapter, this study reveals the potential of 3D-printed lattice structures in continuous, pump-driven oil–water separation systems. This work further advances the structure–function optimization strategy and highlights the prospects of additive manufacturing in scalable and real-time environmental remediation applications.

5.2 Introduction

Oil-water separation has become a critical environmental and industrial challenge due to the increasing discharge of oily wastewater and frequent oil spill accidents. These issues pose severe threats to aquatic ecosystems and human health, necessitating the development of efficient and sustainable separation technologies [66]. Traditional oil-water separation methods, such as coagulation [245], flotation [246], and in situ Burning [29], often suffer from high energy consumption and low separation efficiency and complex operational processes.

Inspired by natural surfaces such as lotus leaves and water-strider legs, superhydrophobic materials with water contact angle (CA) higher than 150° such as aerogels [207], foams [247], microspheres [208], and membranes [233], have demonstrated exceptional potential in oil-water separation field due to their ability to selectively repel water while permitting oil to pass through. In these works, membranes enable rapid filtrated separation, provide structural flexibility, and offer reusability [209]. However, in practical applications, most existing studies have focused on the fabrication of superhydrophobic 2D structure, which faces significant limitations in achieving

continuous oil-water separation. These materials typically require specialized apparatus for operation and consume considerable energy to collect and filter water, making the separation process less efficient and resource intensive. More importantly, their applicability is constrained as they cannot be directly deployed in contaminated water bodies, limiting their efficiency in large-scale environmental remediation. Therefore, the fabrication of architecture structured superhydrophobic mesh-based oil collection devices present an effective solution to this challenge. We propose that by transforming the conventional 2D superhydrophobic mesh into a three-dimensional (3D) structured design, such as a cubic framework, it can be directly deployed as a contaminant collector in polluted water bodies, such as rivers, for continuous oil cleaning. To fabricate such porous architecture, 3D printing emerges as an ideal candidate due to its ability to customized control structural geometry [248,249]. This technology has been widely applied in various fields, including biomedical engineering [250], aerospace [251], and environmental science [252], owing to its rapid prototyping capabilities and design flexibility. However, most previous studies have predominantly focused on 2D superhydrophobic membranes, failing to fully exploit the advantages of 3D printing for constructing architecturally designed porous structures [253-255]. Only a limited number of studies have reported oil-water separation devices with 3D-structured architectures. Li and co-workers demonstrate an interesting 3D printing device for oil water separation [210]. However, the 3D filter is just an idea. Xu et al reported a smart device consisting of a 3D printing polyvinylidene difluoride (PVDF)skeleton and a hydrophobic coated copper mesh [211]. In this work, the 3D porous component is composed of modified hydrophobic copper mesh, rather than being 3D printed. Inspired by water collecting behavior of cactus, Shin and co-workers fabricated a hollow polydimethylsiloxane (PDMS) sponge with a hydrophobic surface which has more space for the storage of collected oil [202]. In the preparation process, 3D printing is only used to create mold for PDMS. As discussed above, the development of 3D printed 3D porous structures for oil-water separation has not yet been reported. Printing 3D porous structures still presents certain challenges.

In this study, we present an innovative 3D-printed porous architecture for continuous oil-water separation. Although various high-precision 3D printing technologies such as stereolithography (SLA) [162], selective laser sintering (SLS) [134], and digital light processing (DLP) [168] offer excellent printing accuracy, we opted for Fused Filament Fabrication (FFF) due to its low cost, ease of use, and suitability for large-scale industrial production [256]. These advantages make FFF

highly promising for practical applications in oil-water separation. To ensure effective oil-water separation, the porous structures must have small pore sizes to achieve high intrusion pressures [257]. However, the relatively lower resolution of FFF presents challenges in fabricating precise micro-structures with uniform pores [258]. To overcome these limitations, we employed precise computational modeling and optimized printing parameters, including printing speed, printing temperature, and extrusion multiplier, to fabricate cubic porous structures with uniform square pores and minimal defects. The fabricated structures exhibited pore heights ranging from 543.2 μm to a maximum of 677.3 μm. Furthermore, by fine-tuning the printing parameters and model design, we successfully produced samples with pore heights as small as 186.7 μm. Additionally, to enhance printing efficiency, we optimized the layer height during fabrication, achieving a significant 83.60% reduction in printing time while maintaining a minimum pore height of 287.7 μm. This study represents the first report of directly fabricating 3D porous structures with uniform pores (error <36.1 μm) using FFF technology, achieving smaller pore sizes than previously reported studies. Furthermore, to impart superhydrophobicity to the fabricated structures, we successfully modified surfaces using a spray-coating method with nano-silica (SiO_2) particles, achieving a remarkable water contact angle of 158.2°. The mechanical stability of the coated layer was validated through peeling tests, confirming its durability under operational conditions. The resulting superhydrophobic porous structures demonstrate excellent oil-water separation performance across various applications. Notably, in a continuous oil-water separation system driven by suction pumping, the material maintained stable performance for at least 24 hours, achieving a separation efficiency of 87.2%.

This study represents the first report of directly fabricating 3D porous architectures with uniform pores using FFF technology, achieving smaller pore sizes and higher structural precision than previously reported studies. The findings provide a new pathway for scalable, low-cost, and efficient superhydrophobic oil-water separation materials, offering potential applications in environmental remediation and industrial wastewater treatment.

5.3 Materials and Methods

5.3.1 Material

The filament used is PLA (Raise Premium 1.75 mm PLA filament). PDMS and the curing agent were purchased from Dow Corning Co. Ltd Shanghai, China. Silica nanoparticles (Si-

300NM) were purchased from Lanling Chemical Co. Ltd Foshan, China. Ethanol, Isopropanol and other solvent were purchased from Zhiyuan Reagent Co. Ltd Tianjin, China. Commercial sponges were purchased from Aojiawei Co. Ltd Shanghai. All materials were used as-received.

5.3.2 Fabrication of 3D PLA porous architectures

The 3D printing experiments were conducted using a commercial dual-extruder FFF printer (Ender-3 S1). As illustrated in Figure 5-1a–e and Figure 5-2a–e, hollow cube-shaped models featuring diamond and square pore structures were designed with SolidWorks software. In the schematic, 'L' denotes the edge length of the cube, 't' represents the thickness of the porous vertical walls, 'w' indicates the width of the solid portion within the porous structure, and 'l' stands for the edge length of the pore openings. To precisely investigate the variations in pore structures under different printing conditions, various printing parameters were designed, as summarized in Table 5-1 (Dimond pores) and Table 5-2 (Square pores).

The overall dimensions of the printed samples were selected primarily based on experimental practicality. The target size was designed to fit standard laboratory beakers and allow stable placement during pumping-based separation tests, ensuring consistent liquid levels and reliable flow-rate measurements. Furthermore, the chosen dimensions provide a sufficient internal volume to observe continuous oil capture while remaining small enough to minimize printing time and material consumption.

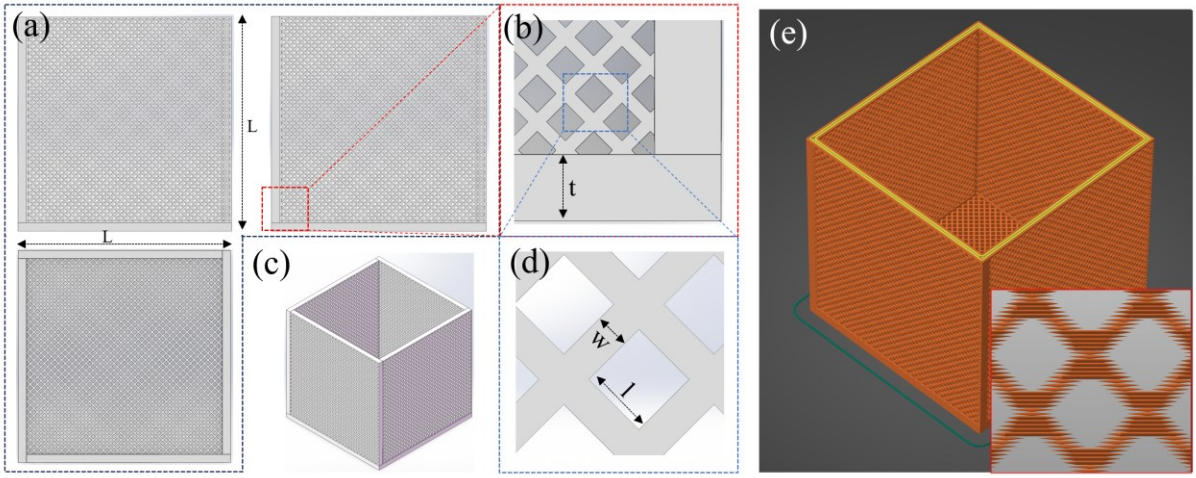

Figure 5.1 ***a*** *Three-view schematic diagram of the diamond pore structure;* ***b*** *Detailed top-view illustration;* ***c*** *Complete 3D model of the sample;* ***d*** *Magnified detail of the pore structure;* ***e*** *Digital model of the sliced sample prepared for 3D printing.*

Table 5-1 Printing parameter for the diamond porous structure

Sample	t(mm)	Speed (mm s^{-1})	T (°C)	Extrusion Multiplier	Layer height(mm)
D1	0.8	30	215	1	0.05
D2	1.6	30	215	1	0.05
D3	2.0	30	215	1	0.05
D4	2.4	30	215	1	0.05
D3LT	2.0	30	205	1	0.05
D3LTF	2.0	45	205	1	0.05
D3LTE	2.0	30	205	0.9	0.05
D3LTE-10	2.0	30	205	0.9	0.10
D3LTE-15	2.0	30	205	0.9	0.15
D3LTE-20	2.0	30	205	0.9	0.20
D3LTE-25	2.0	30	205	0.9	0.25
D3LTE-30	2.0	30	205	0.9	0.30

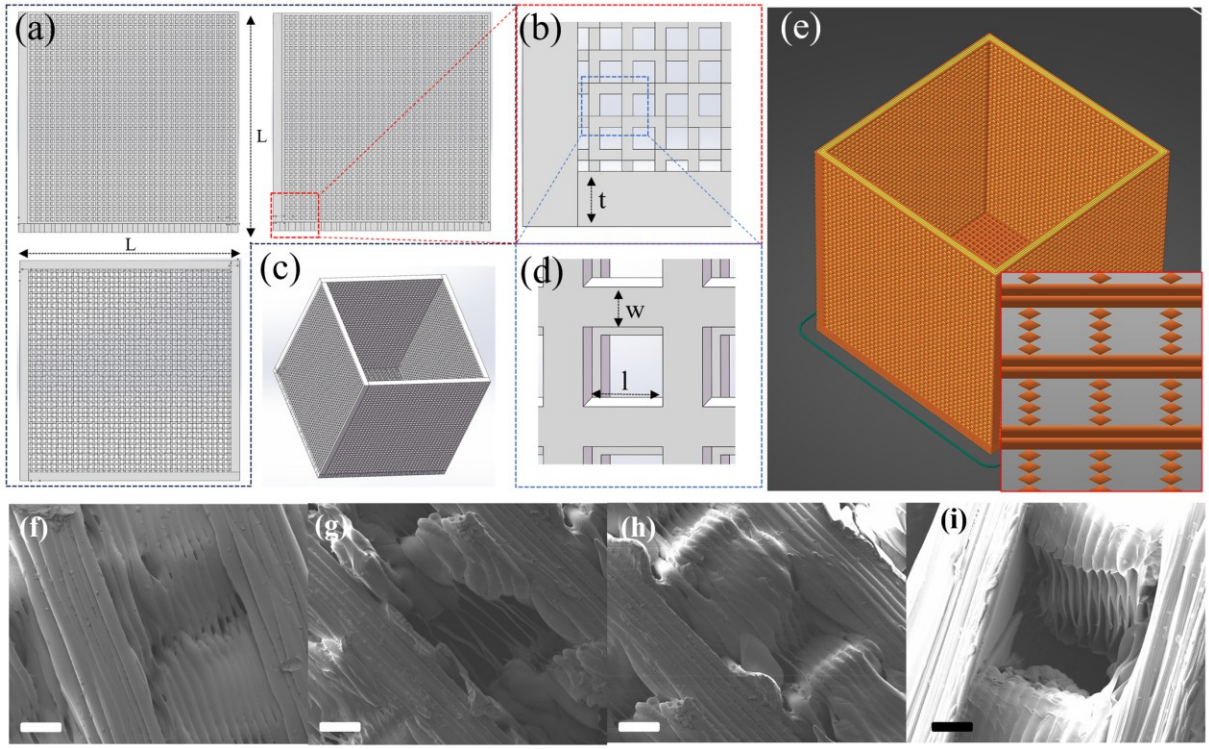

*Figure 5.2 **a** Three-view schematic diagram of the square pore structure; **b** Detailed top-view illustration; **c** Complete 3D model of the sample; **d** Magnified detail of the pore structure; **e** Digital model of the sliced sample prepared for 3D printing. SEM images of printed square pore structures **f** S1, **g** S2, **h** S3 and **I** S4. (Scale bar is 200 µm).*

Table 5-2 Parameter for the Square porous structure

Sample	t(mm)	Speed (mm s^{-1})	T (°C)	Extrusion Multiplier	Layer height(mm)
S1	2	30	215	1	0.05
S2	2	30	215	0.9	0.05
S3	2	30	205	1	0.05

S4	2	30	205	0.9	0.05

5.3.3 Hydrophobic Modification

As illustrated in Figure 5-8a, silica nanoparticles (0.3 g) and isopropanol (10 mL) were initially dispersed into ethanol (10 mL), followed by ultrasonication for 15 min. Subsequently, PDMS (0.07 g) and curing agent (0.007 g) were added, and the mixture was ultrasonicated for another 30 min to achieve a uniform dispersion. For spray coating, this dispersion was transferred into a commercial spray gun and sprayed onto the sample from approximately 20 cm above its surface at a pressure of 0.2 MPa. The spray gun was slowly moved across the substrate surface for a total of 20 cycles. Finally, the coated sample was dried in a fume hood for more than 8 h to ensure complete evaporation of ethanol.

5.3.4 Characterizations

The contact angle measurements were conducted at room temperature using a goniometer (SL200KS, KINO, USA), employing droplets of 2.5 μL volume. Morphological analysis of the samples was performed via scanning electron microscopy (SEM, Hitachi S-4800, Japan), operated at an accelerating voltage of 20 kV. Additionally, surface morphology and elemental distribution were characterized through SEM and energy-dispersive X-ray spectroscopy (EDS) mapping (SEM, 400FEG, USA). Pore sizes were analyzed quantitatively using Nano Measurer software.

5.3.5 Oil-water separation test

In the pumping oil-water separation experiment, the sample (D3LTE) was placed in a mixture of 400 ml water (dyed with methylene blue) and 40 ml cyclohexane (dyed with Sudan III), as illustrated in Figure 5-10. The oil separated by the sample was continuously collected using an electric pump (KCP-B08 from Karmoel Co. Ltd Shanghai). The separation flow rate (f) was calculated according to the following equation:

$$f = \frac{V}{t} \qquad (5-1)$$

where V represents the volume of separated organic solvent, and t is the separation time, defined as the interval from the beginning of the experiment until no further cyclohexane could be collected by the electric pump.

The separation efficiency (e) was calculated as the following equation:

$$e = \frac{m}{M} \quad (5-2)$$

where M and m represent the weight of cyclohexane before and after the separation process, respectively.

In the continuous pumping oil-water separation test, the sample was placed in 440 mL cyclohexane, and the cyclohexane was continuously collected by an electric pump and recirculated back into the beaker, allowing continuous flow across the sample surface. At different time intervals, the sample was taken out and subjected to the standard pumping oil-water separation test mentioned above to evaluate its separation efficiency over time.

5.4 Results and Discussion

5.4.1 Fabrication of Porous Architectures

First, we should analyze the challenges associated with printing vertical porous structures using FFF technology. FFF technology involves the deposition of molten polymer layer by layer, as controlled by a computer program, to form the final structure. This technique typically requires support structures when printing overhangs [259]. However, vertical porous structures inevitably contain numerous overhangs. Printing these unsupported overhangs can lead to material deformation, while using supports would make it impossible to achieve the desired porous structures. Additionally, the precision of FFF is relatively low, as its motors cannot accurately control the extrusion output rate of the polymer. To address these issues, we propose two solutions. First, we could try to precisely adjust the relevant printing parameters, such as printing speed, printing temperature, and extrusion multiplier. Second, we can modify the pore shapes in the design to minimize overhangs.

In this work, as shown in Figure 5-1a-e and Figure 5-2a-e, we primarily designed two different pore shape models. One model has square pores, which are simpler to model, but as indicated by the red box in Figure 5-3a, it includes some overhang structures. The other model has diamond shaped pores, as shown in Figure 5-3b. Although more challenging to model, its 45° inclined structure is not considered an overhang in FFF technology. From a design perspective, square and diamond pore geometries were deliberately selected because they are among the most widely used

unit cells in lattice-type filters and meshes, and can therefore be considered as representative pore motifs. In addition, the square pore topology is consistent with the grid-like infill pattern employed in Chapter 4 for 2D membranes, which facilitates a direct comparison. By introducing both the square and its rotated (diamond) configuration in a cubic architecture, we can simultaneously ensure practical relevance, maintain continuity with the previous chapter, and evaluate the relation between pore structure and separation performance.

The porous architecture of oil-water separation materials plays a pivotal role, as an optimal pore design should selectively hinder water infiltration while allowing oil to pass through. As discussed in our previous work on invasion pressure theory [14], larger pores generate weaker negative capillary forces, whereas smaller pores exhibit stronger capillary resistance. Consequently, different pore structures correspond to varying capacities for withstanding water pressure. Meanwhile, the pore size also influences the flow rate during oil-water separation, which will be further discussed in the oil-water separation section. In FFF technology, the minimum pore size is typically set to twice the nozzle diameter. Although a smaller nozzle diameter could in principle provide higher resolution, we deliberately selected the widely used 0.4 mm nozzle because it represents the standard configuration of most desktop and industrial FFF printers. Using this common nozzle size simplifies operation, enhances process robustness, and makes the proposed architecture more easily transferable to practical large-scale applications. Therefore, unless otherwise specified, l in Figure 5-1 and Figure 5-2 is set to 0.8 mm. To enhance flux while maintaining hydrophobicity, the number of pores should be maximized. Accordingly, w is set to 0.4 mm, corresponding to the 0.4 mm nozzle diameter.

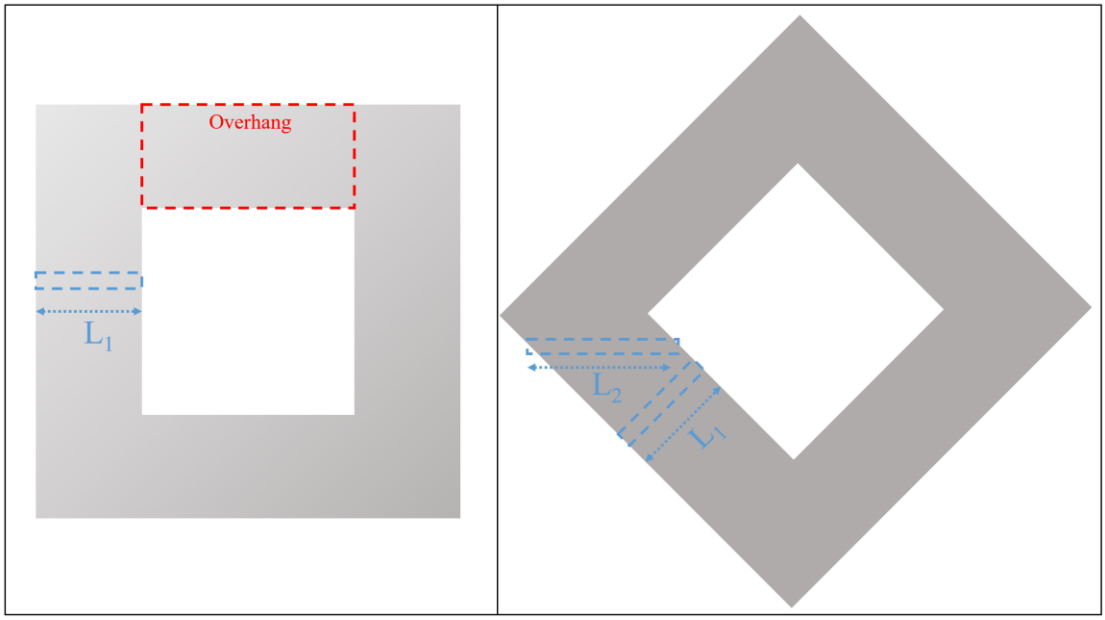

Figure 5.3 ***a*** *square and* ***b*** *diamond pore structure and printing details.*

In the first set of experiments, samples of square pore structures under various parameters, as detailed in Table 5-2, were printed. Among these parameters, the rationale for the setting of t (the thickness of the wall) will be discussed in the diamond pore structure section. Printing speed, printing temperature, and extrusion multiplier are all set to the default recommended settings of the printer. To enhance model accuracy and facilitate observation, the layer height was set to a minimum of 0.05 mm, despite the longer printing time required. As shown in Figure 5-2f, S1 failed to form the intended pore structure, with horizontal layers completely covering the pores. This issue is attributed to the limited precision of FFF technology, where excessive filament extrusion occurs during printing. To improve print quality, adjustments to printing speed, temperature, and extrusion multiplier can be made. Reducing the printing speed enhances print quality [260]; however, when printing microstructures, a speed below 30 mm/s leads to significant deterioration due to the insufficient precision of FFF motors, which struggle to extrude small amounts of polymer accurately at lower speeds. Layer covering of pores may also result from polymer stringing, which can be mitigated by lowering the printing temperature. The minimum printing temperature for PLA is 205°C, as demonstrated in S3 of Figure 5-2h, where reducing the temperature alleviates pore coverage. Adjusting the extrusion multiplier further controls polymer extrusion. When set to 0.9—the lowest practical limit—pore coverage is reduced, as shown in S2 of Figure 5-2g, though significant polymer stringing remains. A combination of lowering both the

temperature and extrusion multiplier (S4 in Figure 5-2i) optimizes both pore coverage and stringing, yet notable defects and overhang issues persist. At this stage, all adjustable parameters have been explored, leading to the conclusion that the square pore structure is unsuitable for vertical porous designs.

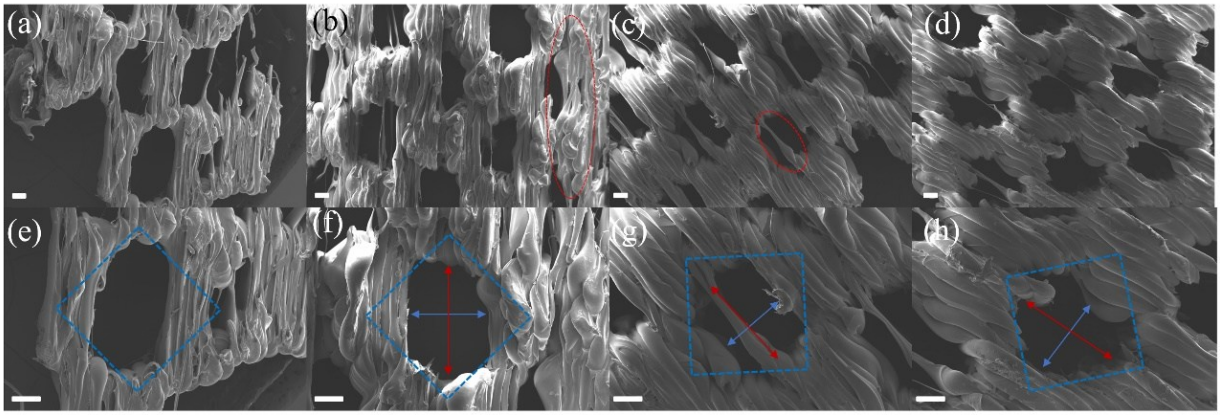

*Figure 5.4 SEM images of diamond pore structure. (**a**)& (**e**) D1, (**b**)& (**f**) D2, (**c**)& (**g**) D3 and (**d**)& (**h**) D4. Scale bar is 200 µm. (Blue box: Designed pore size in the model; Red circle: Defect; Blue arrow: Pore height; Red arrow: Pore width, respectively.)*

Table 5-1 presents the parameters used for printing the diamond pore structures. D1, D2, D3, and D4 were printed under the same conditions but with different model thicknesses (t in Figure 5-1). As shown in Figure 5-4a and e, D1, with a thickness of 0.8 mm, was not successfully printed, and many pore structures were missing. This failure is due to the principles of FFF technology; when the thickness of the previous layer is too low, its mechanical properties are insufficient to support the deposition of the next layer, leading to print failure. As illustrated in Figure 5-4 and f, when the thickness was 1.6 mm, the print quality of D2 was low, with numerous defects still present. With thicknesses of 2 mm and 2.4 mm, shown in Figure 5-4c and g and Figure 5-4 d and h, the material was successfully printed, but defects were still observed in the pore structures. Therefore, in subsequent experiments, models with a thickness of 2 mm will be used to balance printing success and time efficiency.

In the subsequent experiments, based on the printing parameters of D3, the printing temperature was reduced to 205°C to fabricate D3LT. As shown in Figure 5-5a and d, D3LT was successfully printed without a significant decline in quality compared to D3. To enhance energy efficiency, further optimizations will be based on D3LT. To improve printing efficiency, D3LTF was printed at a higher speed than D3LT. However, as clearly illustrated in Figure 5-5b and e, this

led to a substantial deterioration in print quality, confirming that a speed of 30 mm/s is optimal. Additionally, the extrusion multiplier was adjusted to fabricate D3LTE, which significantly improved print quality, as evidenced in Figure 5-5c and f.

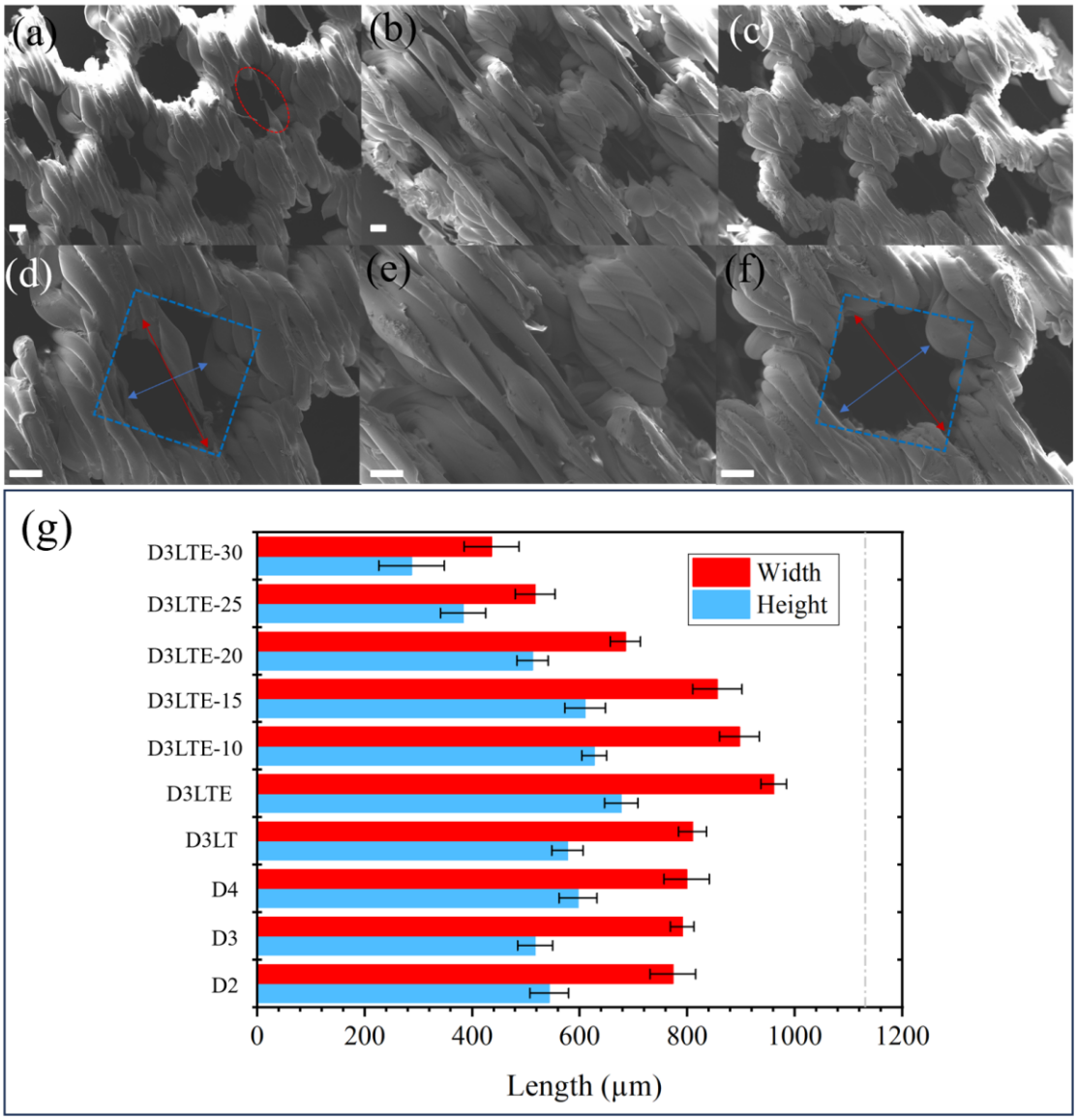

*Figure 5.5 SEM images of diamond pore structure. (**a**)& (**d**) D3LT, (**b**)& (**e**) D3LTF, (**c**)& (**f**) D3LTE. Scale bar is 200 μm. (Blue box: Designed pore size in the model; Red circle: Defect; Blue arrow: Pore height; Red arrow: Pore width, respectively.) (**g**) pore size distribution graph of different samples.*

As shown in Figure 5-5g, the measured pore widths of D2, D3, D4, D3LT, and D3LTE are 773.2 μm, 790.6 μm, 798.9 μm, 810.2 μm, and 961.2 μm, respectively, while the corresponding pore heights are 543.2 μm, 516.9 μm, 596.9 μm, 577.4 μm, and 677.3 μm. SEM images in Figure

5-4 and Figure 5-5 indicate that the actual pore sizes are smaller than the designed values due to the limited precision of FFF technology and polymer deformation. However, reducing the extrusion multiplier effectively increases pore sizes, bringing them closer to the intended dimensions. Compared to square pores, diamond-shaped pores exhibit superior print quality.

As illustrated in Figure 5-3, L1 and L2 represent segments printed in a single print job. Diamond pores demonstrate a 41.4% larger volume per print job compared to square pores. Due to the resolution limitations of FFF technology, printing square pore structures requires the nozzle to extrude smaller amounts of polymer per segment, which can lead to reduced print quality. The diamond structure mitigates this issue, improving overall print fidelity. Additionally, the absence of overhangs in diamond pore structures further enhances print quality.

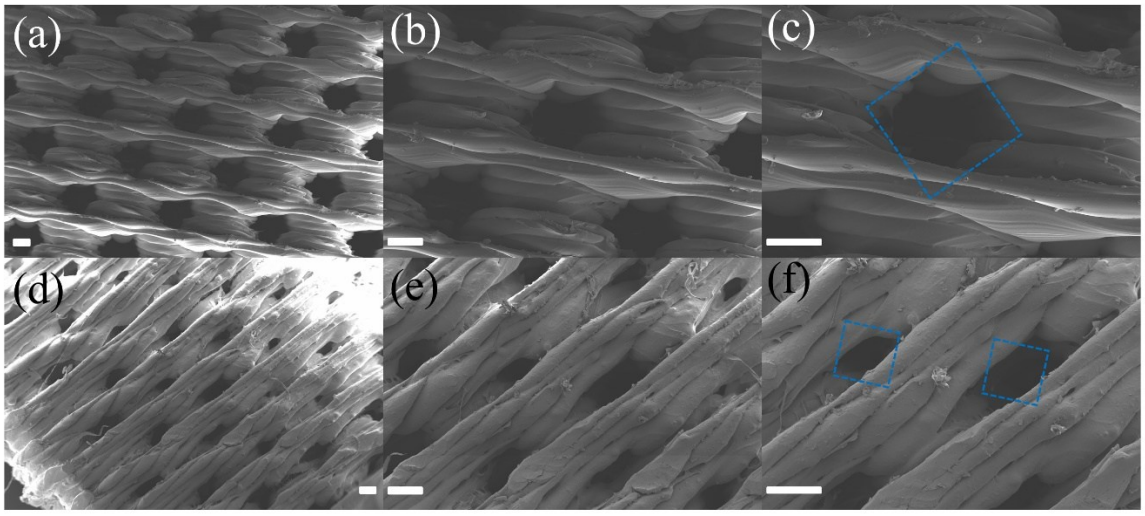

*Figure 5.6 SEM images of diamond pore structure with **a-c** 0.4 mm and **d-f** 0.2 mm pore height.*

Subsequently, we conducted preliminary printing experiments with smaller pore sizes, based on the parameters of D3LTE, while only varying the pore size. Samples with pore sizes of 0.4 mm and 0.2 mm were successfully printed. As shown in Figure 5-6, the porous structures exhibited high print quality. The samples with a designed pore size of 400 μm exhibited uniformly printed pores with an average diameter of 186.7 μm. However, when the pore size was reduced to 0.2 mm, the pore sizes became inconsistent, and many pores were not fully through-holes. Although a vertical porous structure with a pore size of 186.73 μm was successfully fabricated through precise control of printing parameters, its inability to significantly reduce printing time by adjusting the layer height presents potential challenges in practical oil-water separation applications. Due to limitations such as reduced flow rate and increased fabrication complexity ob-served in smaller

pore sizes, subsequent studies will primarily focus on samples with a pore size of 800 µm, which offer a more favorable balance between performance and manufacturability.

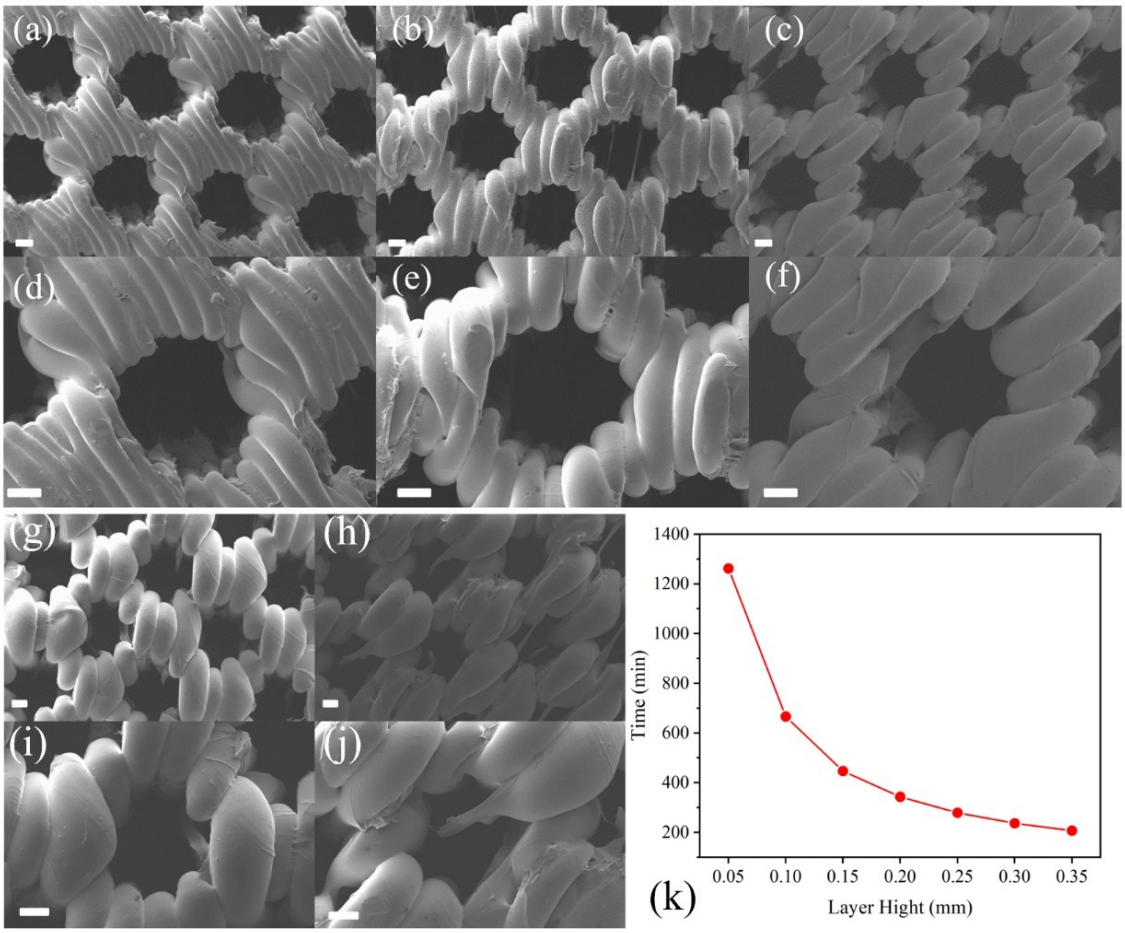

*Figure 5.7 SEM images of diamond pore structure. **a**& **d** D3LTE-10, **b**& **e** D3LTE-15, **c**& **f** D3LTE-20, **g**& **i** D3LTE-25 and **h**& **j** D3LTE-30. Scale bar is 200 µm. **k** Relationship between layer height and printing time. Scale bar is 200 µm.*

Reducing the fabrication time of vertical porous structures is a critical step toward achieving large-scale industrial production, significantly enhancing manufacturing efficiency. Among printing parameters, increasing the printing speed is a direct approach to reducing fabrication time. However, as shown in Figure 5-5b and e, when the speed exceeds 30 mm/s, substantial structural defects emerge due to the precision limitations of FFF technology. An alternative method currently being considered for time reduction is decreasing the layer height. As presented in Table 5-1, samples such as D3LTE-10 were designed based on the printing parameters of D3LTE, with D3LTE-30 featuring a layer height of 0.3 mm—the maximum limit supported by the employed printer. As illustrated in Figure 5-7k, adjusting the layer height effectively reduces printing time.

The printing time for D3LTE with a layer height of 0.05 mm is 1262 minutes, whereas for D3LTE-30 with a 0.3 mm layer height, it is reduced to 207 minutes, representing an 83.60% reduction in printing time. This significant time reduction is attributed to the layer-by-layer deposition mechanism of FFF technology, where a larger layer height results in fewer total layers, thereby shortening the overall printing duration. However, increasing the layer height also compromises print resolution. The SEM images in Figure 5-7a–j depict samples printed with different layer heights, demonstrating that all exhibit well-formed and structurally intact pores due to optimized printing parameters. Nonetheless, as shown in Figure 5-5g, D3LTE-10 has a pore height of 627.4 μm, whereas D3LTE-30 exhibits a significantly smaller pore height of 287.7 μm. The increased layer height introduces larger dimensional deviations, leading to a notable reduction in the actual pore size compared to the designed model. Moreover, as observed in Figure 5-7g–j, an increased occurrence of filament stringing and other printing defects can be identified. These imperfections are also attributed to the precision limitations of FFF technology during the printing process.

In addition to performance optimization, the cost-effectiveness of this fabrication method is also noteworthy. The FFF printer used in this study is commercially available at a market price ranging from approximately $165 to $275 USD, and the PLA filament costs around $38 USD per kilogram. Resulting in a material cost of approximately $0.68 USD per sample. These figures highlight the economic viability of the method, making it highly attractive for large-scale production and field applications in environmental remediation and industrial wastewater treatment. In addition to the material cost, a more comprehensive cost assessment should also consider other practical factors. These include the printing time cost associated with long fabrication durations, the energy consumption of the FFF printer during continuous operation, and the projected scaling cost when producing larger structures for real environmental applications. Although these factors were not quantitatively analyzed in this study, they represent important considerations for future economic evaluations of large-scale deployment.

5.4.2 Hydrophobic modification

In our previous work, the spray-coating method has been demonstrated as an efficient and cost-effective approach for superhydrophobic modification [261], as illustrated in Figure 5-8a. Ethanol, an environmentally friendly and low-cost solvent, was selected as the dispersion medium. The addition of isopropanol enhances the dispersion of silica nanoparticles in ethanol, improving

coating uniformity. PDMS acts as a binder, linking the silica nanoparticles to the sample surface after curing. Silica nanoparticles contribute to reducing the surface energy of the material while simultaneously increasing nanoscale roughness. According to the Cassie and Wenzel models, this dual effect significantly enhances the hydrophobicity of the modified surface [107]. However, the long-term stability of the silica nanoparticles on the surface, particularly their potential detachment during practical applications, remains a concern. Further investigations are required to assess the extent of nanoparticle loss and its potential environmental impact.

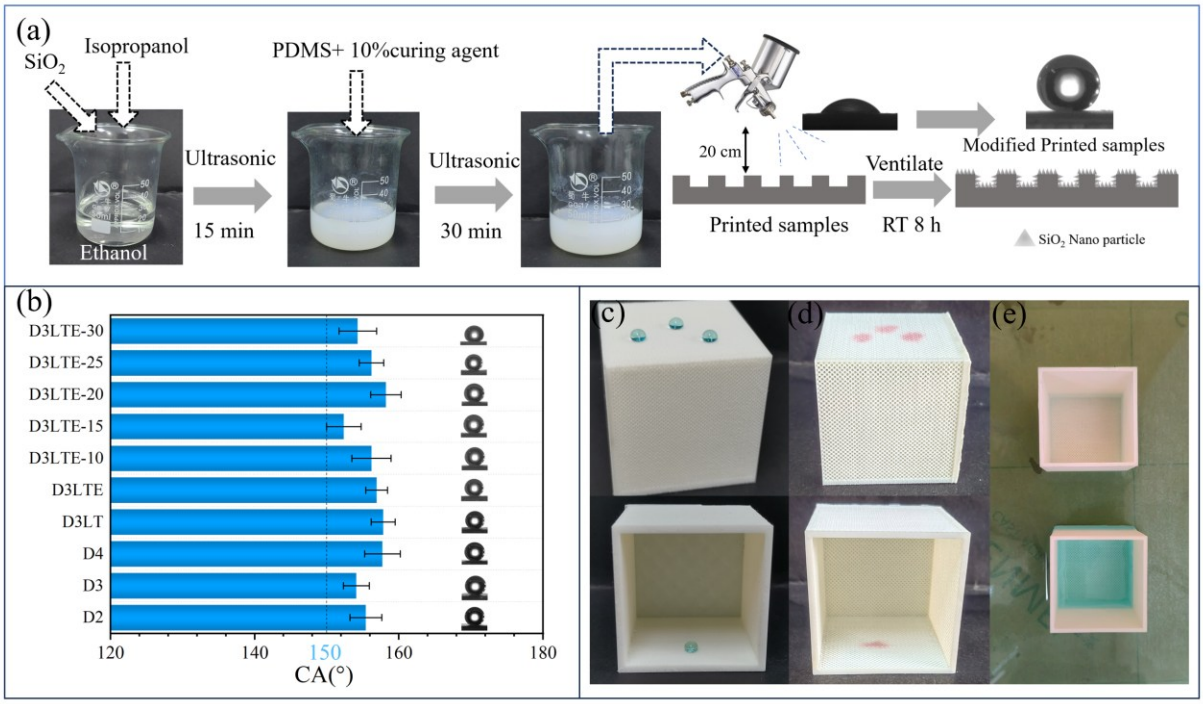

Figure 5.8 ***a*** *Hydrophobic modification process and comparison of water contact angles before and after modification of D3LTE.* ***b*** *Water contact angles of different samples. Digital photograph of D3LTE and* ***c*** *its water contact angle and* ***d*** *oil contact angle (cyclohexane).* ***E*** *Photographs of the D3LTE surface submerged in water before and after modification.*

As shown in Figure 5-8a, after hydrophobic modification, the contact angle of D3LTE increased from 79.2° to 156.9°, reaching the threshold for superhydrophobicity. The digital photograph in Figure 5-8c illustrates that water droplets retain a spherical shape on the modified D3LTE surface, indicating a strong water-repellent effect. For oils such as cyclohexane, as depicted in Figure 5-8d, the liquid is completely absorbed due to capillary forces, resulting in a contact angle of 0°. Furthermore, Figure 5-8e presents a comparison of D3LTE before and after

modification when submerged in water. The unmodified sample exhibits water infiltration into its internal pores, whereas the modified D3LTE remains dry. This is attributed to the negative capillary effect generated by its superhydrophobic surface, which effectively resists water penetration under hydrostatic pressure.

Except for D3LTF, where the pore structure was heavily obstructed, and D1, which failed to print successfully, the contact angles of all other samples were measured. As shown in Figure 5-8b, no significant differences were observed among the contact angles of different samples. The highest contact angle, 158.2°, was recorded for D3LTE-20, while the lowest, 152.3°, was observed for D3LTE-15. Although samples fabricated with different printing parameters exhibit variations in pore size and microscale surface roughness, no clear correlation was found between these parameters and the resulting contact angle. This is because the sample surface consists primarily of PLA, with only minor differences in microscale roughness. The improvement in hydrophobicity is predominantly attributed to the low surface energy provided by the modification process and the introduction of nanoscale roughness [236]. Consequently, all modified samples achieved superhydrophobicity, and the variation in contact angles did not follow a distinct pattern.

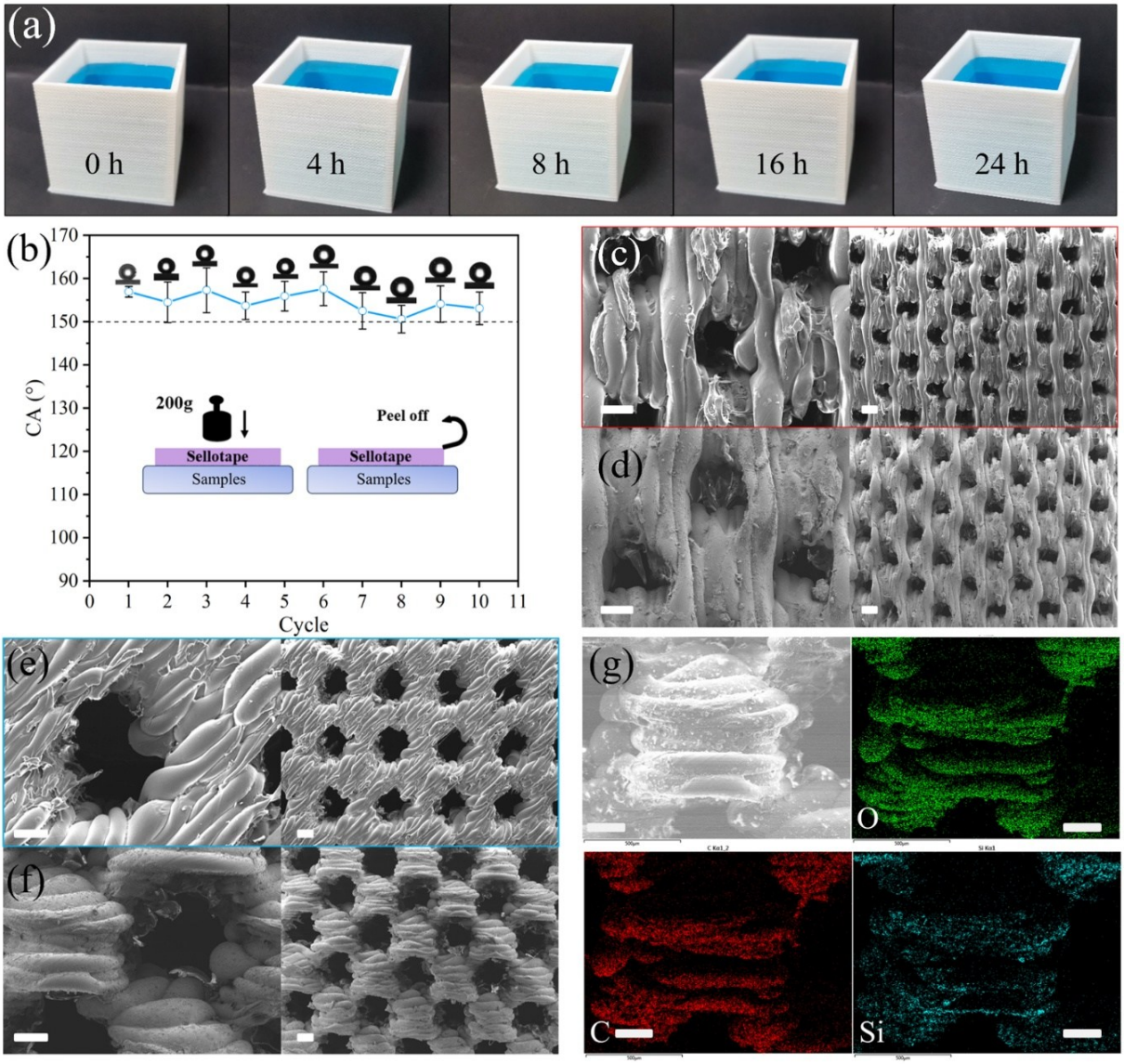

Figure 5.9 ***a*** *Experiment demonstrating the internal water pressure resistance of modified D3LTE over 24 hours.* ***b*** *Contact angle variation of modified D3LTE during the peeling test. SEM images of* ***c*** *the sample with a 0.4 mm pore size and* ***d*** *its modified version. SEM images of* ***e*** *unmodified D3LTE and* ***f*** *modified D3LTE.* ***g*** *Elemental mapping images of modified D3LTE. Scale bar is 200 µm.*

Figure 5-9a illustrates the ability of the sample surface to withstand continuous water pressure. Over a 24-hour period, no water leakage was observed, demonstrating the material's excellent resistance to liquid infiltration. During the experiment, a notable phenomenon was observed: the water inside the sample evaporated rapidly and had to be continuously replenished to maintain the liquid level. This can be attributed to the high surface roughness and porosity of the modified structure based on Cassie-Baxter theory [107,172], which enhances the evaporation rate by

increasing the water-air interface area and reducing the contact between water and the underlying solid, thus minimizing heat dissipation. As shown in Figure 5-9b, the sample surface was repeatedly subjected to peeling tests. After ten cycles, the modified D3LTE retained its hydrophobicity, with a contact angle of 153.1°, demonstrating strong adhesion stability. This stability is attributed to the excellent mechanical properties of PDMS, which serves as an effective binder between silica nanoparticles and the porous skeleton, preventing detachment under mechanical stress [55].

To confirm the presence of silica nanoparticles on the sample surface, SEM images of unmodified and modified D3LTE are shown in Figure 5-9e and f, respectively. The modified surface exhibits significantly increased roughness, indicating successful nanoparticle deposition. Further elemental analysis was conducted using EDS, as shown in Figure 5-9g. Three characteristic elements—C, O, and Si—were detected on the modified surface. Si is uniformly distributed, confirming the successful incorporation of silica nanoparticles. Additionally, Figure 5-9c and d display SEM images of samples with a pore size of 0.4 mm, revealing similar roughness variations, further supporting the uniformity and effectiveness of the surface modification process.

5.4.3 Oil-water separation experiment

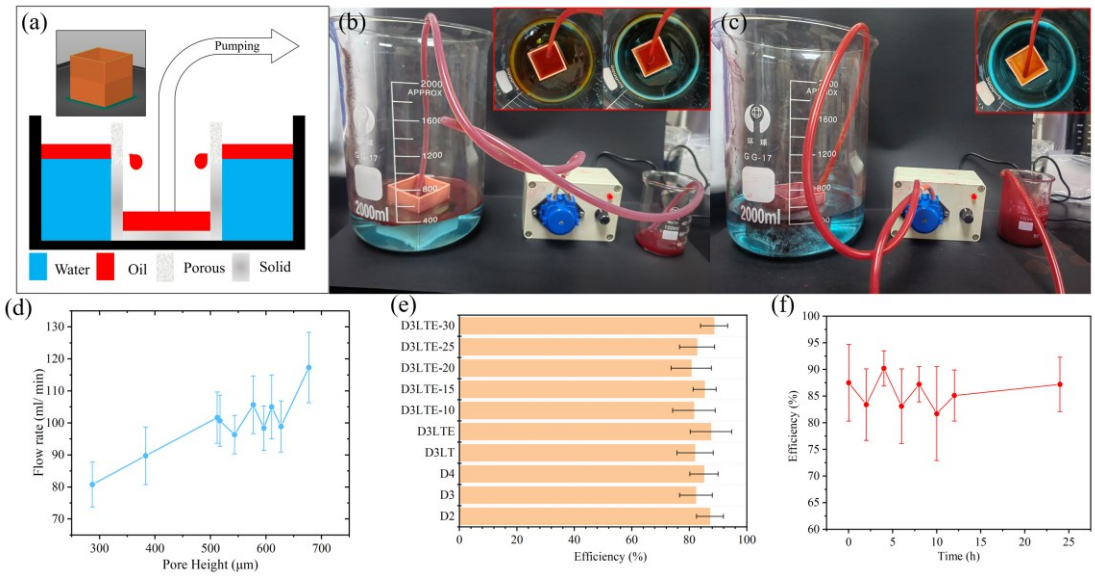

Figure 5.10 ***a*** *Schematic diagram of the continuous pumping oil-water separation experiment.* ***b*** *Photographs taken during the continuous pumping oil-water separation process.* ***c*** *Image of the separated oil and water after the experiment.* ***d*** *Flow rate of different samples (based on pore height) during oil-water separation.* ***e*** *Separation efficiency of different samples.* ***f*** *Efficiency variation of modified D3LTE during continuous oil-water separation over 24 hours.*

To achieve continuous oil-water separation, an experimental setup was designed under laboratory conditions, as illustrated in Figure 5-10a. Modifications were made to the sample model to address the issue of secondary contamination. Since oil inherently passes through porous structures via capillary action, leading to potential leakage, the lower half of the sample was designed as a solid, non-porous region, providing an integrated oil storage capability. As shown in Figure 5-10b, the sample was placed in a beaker and secured underwater using double-sided tape. A controlled volume of water and cyclohexane was then introduced into the system. Due to the negative capillary effect induced by the superhydrophobic surface, water was effectively repelled, whereas cyclohexane permeated the porous structure under the combined effects of liquid pressure and capillary forces and was subsequently collected using an electric pump. After separation, as depicted in Figure 5-10c, the water surface remained clear and free of oil contamination, demonstrating effective oil removal.

Figure 5-10d presents the flow rate of different samples during oil-water separation. The flow behavior of cyclohexane through the porous structure can be analyzed using Darcy's law [262], which describes the relationship between flow velocity and permeability in a porous medium:

$$v = \frac{k\,\Delta P}{\mu\,L} \qquad (5-3)$$

where v is the fluid velocity, k is the permeability of the porous medium, μ is the dynamic viscosity of cyclohexane, ΔP is the pressure difference across the porous structure, and L is the thickness of the porous layer. Since permeability k is proportional to the square of the pore radius ($k \propto r^2$). Darcy's law predicts that larger pores should lead to significantly higher flow rates. This theoretical trend aligns generally with our experimental results, where an in-creasing flow rate is observed with larger pore size, where an increasing trend in flow rate is observed with the enlargement of pore size (height). D3LTE, with a pore height of 677.3 μm, exhibits the highest flow rate (117.3 mL/min), while D3LTE-30, with a smaller pore height of 287.7 μm, demonstrates the lowest flow rate (80.7 mL/min). These results confirm that pore size plays a dominant role in controlling flow rate, as larger pores reduce flow resistance and enhance permeability. However, the observed flow rate differences between samples are less pronounced than those predicted by Darcy's law. According to theoretical calculations, the flow rate should be scaled with r^2, suggesting that the sample with a larger pore size should exhibit a significantly higher flow rate than what is experimentally recorded. This discrepancy indicates that additional factors beyond

permeability influence fluid transport under low hydraulic pressure conditions. One key factor to consider in low-pressure filtration environments is the capillary effect, which becomes more significant in smaller pores. The Laplace theory shows that smaller pores generate higher capillary pressure. These capillary forces will cause cyclohexane to pass through the porous structure more quickly. In this experiment, the small-pore sample (D3LTE-30) exhibits greater capillary resistance, counteracting the permeability-driven flow enhancement predicted by Darcy's law. This effectively narrows the flow rate difference between samples with large and small pores, explaining why the experimental results deviate from purely permeability-based predictions. Therefore, the observed non-linearity in the flow response should not be interpreted as a violation of Darcy's law, but rather as a reflection of complex interfacial phenomena, particularly in porous membranes with superhydrophobic modifications.

Figure 5-10e presents the separation efficiency of different samples, with D3LTE-30 exhibiting the highest efficiency at 88.6%. As observed in Figure 5-10c, residual cyclohexane remains on the sample surface and water surface after separation, which accounts for the inability to achieve 100% separation efficiency. Additionally, a 24-hour continuous oil-water separation test was conducted using D3LTE. After 24 hours, the separation efficiency remained at 87.2%, demonstrating the sample's potential for long-term oil-water separation applications.

The above analysis provides valuable insights into the practical application of the samples. However, these results are based on preliminary exploratory experiments conducted under controlled laboratory conditions. In real-world applications, the fluid environment is significantly more complex and dynamic. Therefore, further studies are required to validate these findings and optimize the samples for practical implementation.

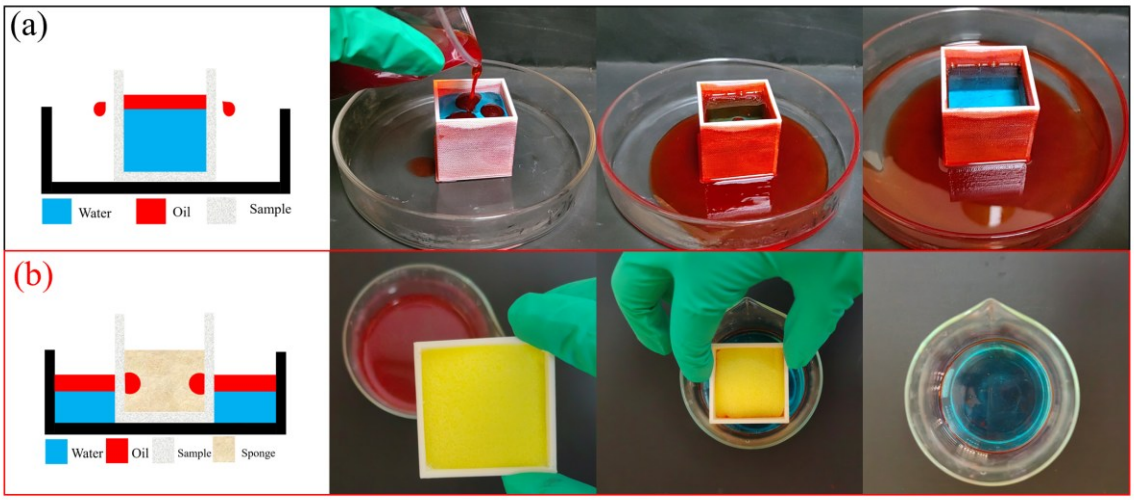

Figure 5.11 ***a*** *Schematic diagram of the internal oil-water separation method and its corresponding photos.* ***b*** *Schematic diagram of the adsorption-based oil-water separation method combines with sponge and its corresponding photos.*

Due to the superhydrophobic porous structure of the sample, alternative oil-water separation methods can be employed. As illustrated in Figure 5-11a, cyclohexane and water are introduced into the internal space of the sample, where cyclohexane selectively permeates through the porous structure, enabling separation. Additionally, the sample can be combined with a sponge to achieve an adsorption-based oil-water separation process (Figure 5-11b). When a sponge is placed inside the sample, the cyclohexane that passes through the porous surface is immediately absorbed by the sponge, enabling the removal of cyclohexane from the water.

5.5 Conclusion

In this study, a 3D-printed superhydrophobic porous architecture was successfully fabricated using FFF technology, demonstrating efficient and continuous oil-water separation. By optimizing printing parameters, including extrusion multiplier, printing speed, and layer height, a diamond-pore structure was developed, minimizing overhang defects while achieving uniform pores with a maximum deviation of 36.1 μm.

Superhydrophobic modification was achieved via spray-coating with silica nanoparticles and PDMS, increasing the water contact angle of D3LTE from 79.2° to 158.2°. The coated structures exhibited strong mechanical stability, retaining a contact angle of 153.1° after 10 peeling cycles and withstanding internal water pressure for 24 hours without leakage.

Oil-water separation experiments demonstrated significant performance advantages. In a continuous pumping system, the material (D3LTE) maintained 87.2% separation efficiency over 24 hours, with the highest efficiency recorded at 88.6% (D3LTE-30). Flow rate analysis confirmed the strong influence of pore size, with D3LTE (677.3 μm pores) achieving a flow rate of 117.3 mL/min, while D3LTE-30 (287.7 μm pores) exhibited a reduced flow rate of 80.7 mL/min. These findings establish a new pathway for scalable, energy-efficient oil-water separation, offering a cost-effective and industrially viable solution for environmental remediation and wastewater treatment.

Looking forward, several directions remain to be explored to further advance the applicability of this approach. These include the use of large-scale industrial 3D printers to fabricate porous structures while maintaining high geometric fidelity, long-term environmental assessment of potential nanoparticle release during continuous operation, and structural optimization for effective separation under complex real-world conditions such as viscous oils or saline wastewater. These future efforts will be essential for translating the current laboratory-scale success into robust, field-deployable solutions.

Chapter 6: General Discussion, Conclusions and Perspectives

6.1 Integrated Discussion of Chapters 4–5

The experimental studies presented in Chapters 4 and 5 collectively demonstrate how geometric design freedom, fabrication precision and post-processing treatment jointly determine the performance of superhydrophobic porous materials for oil–water separation. The 2D PLA membranes developed through the model-free infill approach highlight the remarkable flexibility of slicing-based structural control, enabling tunable pore sizes without the need for CAD modelling. However, their planar nature inherently restricts the depth of fluid pathways and limits their applicability to gravity-driven or static separation scenarios.

In contrast, the 3D printed diamond-structured architectures reveal the advantages of spatially interconnected pore networks, which enhance fluid transport, mechanical stability and structural integrity under continuous pumping conditions. The vertically aligned rhombic pores offer predictable channel geometry and significantly higher stiffness compared to 2D membranes, allowing the system to maintain separation performance during prolonged operation. These differences underline a key insight of this dissertation: the transition from 2D to 3D architectures fundamentally shifts the separation mode from batch operation to continuous flow, thereby expanding the application potential of printed porous materials.

Moreover, although both systems rely on the same PDMS–silica coating for superhydrophobicity, the 3D architectures exhibit more uniform coating deposition due to their larger accessible surface area and reduced edge effects. This highlights the synergistic interplay between geometry and surface treatment, showing that the benefits of hydrophobic modification are most effectively exploited when combined with structurally optimized lattice designs.

Overall, the comparative analysis of Chapters 4 and 5 illustrates a clear progression from rapid prototyping and feasibility demonstration (2D membranes) toward more application-ready, mechanically robust separation modules (3D lattices). This integrated interpretation lays the foundation for the scalability considerations and broader perspectives discussed in the following sections.

6.2 Scientific Contributions

The key scientific contributions of this dissertation can be summarized as follows:

- This thesis conducted a comprehensive and in-depth review and analysis of fabrication strategies, fundamental theories, and application prospects of 3D-printed superhydrophobic materials, based on literature retrieved from the Web of Science database. It systematically examined the theoretical foundations of wettability and clarified their role in the surface design of 3D-printed structures. Although various printing materials and techniques have been reported, this work identified a generalized fabrication workflow consisting of four essential steps: material preparation, model design, printing process, and post-processing. This framework provides a unified basis for comparing different strategies and optimizing processing parameters across platforms.
- In this work, a novel strategy was proposed for the fabrication of 2D porous PLA membranes without the need for complex CAD modeling. By simply adjusting the infill percentage in the slicing software, porous structures with tunable pore sizes were generated. The smallest measured pore side length reached 313.02 μm, confirming the feasibility of achieving structural control through a model-free approach. This innovation significantly simplifies the design process, making the method accessible for rapid prototyping and functional customization.
- To fully exploit the advantages of 3D printing for fabricating spatially designed porous architectures, this study developed a superhydrophobic oil–water separation device featuring vertically aligned diamond-like pores. The structure was fabricated using Fused Filament Fabrication (FFF) technology with carefully optimized printing parameters—including extrusion multiplier, printing speed, and layer height—to achieve high pore uniformity and dimensional precision. The maximum deviation in pore dimensions was limited to just 36.1 μm, demonstrating excellent geometric control while minimizing overhang defects.
- A solvent-free surface modification strategy was developed using PDMS and silica nanoparticle spray-coating, enabling the formation of durable superhydrophobic surfaces with water contact angles exceeding 150°. This post-treatment approach is simple and scalable, allowing continuous oil–water separation under laboratory conditions while maintaining hydrophobic performance over repeated use.

These contributions have systematically advanced the development of fabrication strategies for 3D-printed superhydrophobic porous materials, provided new perspectives for future research in the field, and further accelerated the potential for real-world application and technological translation.

6.3 Scalability Considerations for FFF-based Architectures

While the current work demonstrates the feasibility of fabricating well-defined porous structures using FFF at the laboratory scale, scaling these architectures toward practical separation modules introduces several engineering challenges. First, printing time increases almost linearly with projected area, meaning that the fabrication of centimeter-scale specimens can be completed within minutes, whereas modules approaching tens of centimeters require several hours and may exhibit reduced dimensional consistency due to thermal accumulation and material shrinkage. Maintaining pore uniformity across large areas is therefore non-trivial and may require advanced slicing strategies or parallel multi-nozzle systems.

Second, the reproducibility of wetting properties becomes increasingly sensitive to local geometric variations as the printed area grows. Surface robustness strongly depends on consistent coating thickness; however, manual spray-coating tends to produce uneven deposition when applied to large or highly complex geometries. Upscaling thus necessitates the integration of automated coating technologies such as controlled atomization, dip-coating, or rotary spraying to ensure uniform hydrophobic performance.

Finally, although printed devices withstand the low pressures used in laboratory experiments, larger structures may experience significant mechanical stresses during continuous flow operation. The inherent anisotropy of FFF, particularly the weaker interlayer bonding, poses limitations on the maximum operational pressure of large modules. These considerations emphasize the need to clearly distinguish between experimentally validated capabilities at the current scale and prospective developments required for real-world implementation.

6.4 Limitations

Despite the significant progress achieved in this study, several limitations remain. While the 3D printing strategy enabled controllable pore size fabrication, the resolution is still constrained by the nozzle diameter and the thermal properties of PLA, which limits the minimum achievable feature size. As this work represents an initial exploration of 3D printing for oil–water separation,

it lacks in-depth investigation into the effects of pore geometry, pore shape, and complex 3D structural designs on separation performance.

Although the surface modification strategy proved effective, it relies on the mechanical stability of the nano-coating layer, which may deteriorate under real-world conditions due to abrasion or prolonged immersion. In particular, the detachment of silica nanoparticles could pose potential environmental risks.

Lastly, all oil–water separation experiments were conducted under controlled laboratory conditions. The system has not yet been tested in real-world marine environments, such as natural seawater, where salinity, contaminants, and turbulence may affect long-term separation performance. Moreover, the intrinsic anisotropy of FFF introduces structural vulnerabilities that become more pronounced during scale-up. Because mechanical strength is primarily governed by interlayer adhesion, printed lattices may exhibit reduced compressive or bending resistance when subjected to higher pump pressures or extended cyclic loading. While this effect is negligible for small laboratory-scale samples, it could significantly influence the long-term durability and failure modes of larger continuous-separation modules. In addition to geometric and process-related factors, the biodegradability of PLA must also be taken into account when considering long-term or real-world operation. PLA is known to undergo hydrolytic degradation in aqueous environments, particularly under elevated temperature or acidic/basic conditions, which may progressively weaken the structural integrity of the printed lattice. Future studies should therefore evaluate the extent of PLA degradation under continuous separation conditions and assess how such changes may affect mechanical performance, coating stability and overall service life. Addressing these limitations will require not only process optimization but also potential reinforcement strategies or the exploration of alternative, more hydrolytically stable polymers.

6.5 Perspectives

In addition to these findings, future work should primarily address the limitations identified in this study.

For instance, with the continuous advancement of 3D printing technology, the latest FFF printers now offer significantly improved printing resolution and speed, which could be explored in future studies to overcome the current structural constraints. Moreover, further literature review is needed to assess the potential ecological risks of silica nanoparticles and to identify alternative

hydrophobic modification strategies that are more environmentally sustainable. Finally, performing long-term tests in marine, river, or industrial wastewater environments will provide valuable insights into the scalability and robustness of the proposed system under real-world conditions.

Besides, two future research directions are particularly worth exploring:

(1) Environmentally Friendly Strategies Alternatives

While this study employed a PDMS/silica nanoparticle coating to achieve superhydrophobicity, future work should explore more sustainable and biodegradable approaches. This includes the use of naturally derived, environmentally benign hydrophobic materials, or a paradigm shift toward hydrophilic–underwater oleophobic surfaces for oil–water separation. The latter approach mimics biological membranes and often involves natural polymers such as cellulose or chitosan, which are renewable and degradable.

(2) Application in Medical Implants

The porous structures developed in this study also hold significant potential for biomedical applications. Their morphology resembles that of clinical implantable materials used in procedures such as pelvic floor repair, where porous designs facilitate tissue ingrowth, fluid exchange, and mechanical stability after implantation. In this context, 3D printing offers several key advantages, including customizable geometries tailored to patient anatomy, the use of biodegradable polymers such as PLA, and the possibility of incorporating functional agents like drugs or antibacterial coatings. These features collectively support the translation of such porous systems into next-generation personalized medical devices.

These two directions—greener wettability control and biomedical translation—represent promising frontiers for expanding the impact of 3D-printed porous materials across environmental and healthcare domains.

List of Publications

[1] **X. Wang**, A. Hassan, H. Boudaoud, F. Xue, Z. Zhou*, X. Liu*, A Review on 3D-printing of bioinspired hydrophobic material and its applications, Advanced Composites and Hybrid Materials, 2023, 6, 170. https://doi.org/10.1007/s42114-023-00740-2. (Chapter 3)

[2] **X. Wang**, J. An, A. Hassan, Q. Gao, X. Liu*, H. Boudaoud, Simplified 3D Printing Method for Fabrication of Superhydrophobic Oil-Water Separation Membrane with Controllable Pore Size, Journal of Applied Polymer Science, 2025, 142, e57217. http://doi.org/10.1002/app.57217 (Chapter 4)

[3] **X. Wang**, J. An, A. Hassan, Q. Gao, X. Liu*, H. Boudaoud, Innovative 3D-Printed Superhydrophobic Porous Architectures for Continuous Oil–Water Separation, Polymers, 2025, 17(11), 1465. https://doi.org/10.3390/polym17111465 (Chapter 5)

References

1 Chen C, Weng D, Mahmood A, Chen S, Wang J (**2019**) Separation Mechanism and Construction of Surfaces with Special Wettability for Oil/Water Separation. *ACS Appl. Mater. Interfaces* 11:11006-27. https://doi.org/10.1021/acsami.9b01293

2 Ma Q, Cheng H, Fane AG, Wang R, Zhang H (**2016**) Recent Development of Advanced Materials with Special Wettability for Selective Oil/Water Separation. *Small* 12:2186-202. https://doi.org/10.1002/smll.201503685

3 International Tanker Owners Pollution Federation (ITOPF) (**2022**) Oil Tanker Spill Statistics 1970 to 2021 [Online]. Available at: https://www.itopf.org/knowledge-resources/data-statistics/statistics/ (Accessed: 19 May 2025).

4 Ossai IC, Ahmed A, Hassan A, Hamid FS (**2020**) Remediation of soil and water contaminated with petroleum hydrocarbon: A review. *Environ. Technol. Innov.* 17:100526. https://doi.org/10.1016/j.eti.2019.100526

5 El-Zahaby AM, Kabeel AE, Bakry AI, Khaira AM (**2010**) Effect of Disk Offset Angle on the Hydrodynamic Performance of Rotating Disk Skimmers During Oil Spill Recovery. *Environ. Eng. Sci.* 28:113-9. https://doi.org/10.1089/ees.2010.0092

6 Rahsepar S, Smit MPJ, Murk AJ, Rijnaarts HHM, Langenhoff AAM (**2016**) Chemical dispersants: Oil biodegradation friend or foe? *Mar. Pollut. Bull.* 108:113-9. https://doi.org/10.1016/j.marpolbul.2016.04.044

7 Riis V, Brandt M, Miethe D, Babel W (**2000**) Influence of special surfactants on the microbial degradation of mineral oils. *Chemosphere* 41:1001-6. https://doi.org/10.1016/S0045-6535(99)00484-1

8 Yong J, Yang Q, Huo J, Hou X, Chen F (**2021**) Superwettability-based separation: From oil/water separation to polymer/water separation and bubble/water separation. *Nano Sel.* 2:1580-8. https://doi.org/10.1002/nano.202000246

9 Fritz DE (**2003**) In Situ Burning of Spilled Oil in Freshwater Inland Regions of the United States. *Spill Sci. Technol. Bull.* 8:331-5. https://doi.org/10.1016/S1353-2561(03)00013-6

10 Yan G, B. C, C. C, Y. Y, Q. W, H. D, S. L, and Guo S (**2015**) Bioremediation of Crude Oil Contaminated Soil. Petrol. Sci. Technol. 33:717-23. https://doi.org/10.1080/10916466.2014.954670

11 Rasouli S, Rezaei N, Hamedi H, Zendehboudi S, Duan X (**2021**) Superhydrophobic and superoleophilic membranes for oil-water separation application: A comprehensive review. *Mater. Des.* 204:109599. https://doi.org/10.1016/j.matdes.2021.109599

12 Chu Z, Feng Y, Seeger S (**2015**) Oil/Water Separation with Selective Superantiwetting/Superwetting Surface Materials. *Angew. Chem. Int. Ed.* 54:2328-38. https://doi.org/10.1002/anie.201405785

13 Cheng XQ, Jiao Y, Sun Z, Yang X, Cheng Z, Bai Q, Zhang Y, Wang K, Shao L (**2021**) Constructing Scalable Superhydrophobic Membranes for Ultrafast Water–Oil Separation. *ACS Nano* 15:3500-8. https://doi.org/10.1021/acsnano.1c00158

14 Wang X, Liu Q, Pan Y, Tu Y, Liu X (**2024**) Fabrication of Superhydrophobic Polycaprolactone Foam via Phase Separation and Silica Modification for Oil–Water Separation. *Macromol. Chem. Phys.* 225:2300436. https://doi.org/10.1002/macp.202300436

15 Wen T, Lin J, Jiang Z, Han L, Yang W, Chen H, Zhang X (**2024**) Modifier-free sol–gel preparation of cotton fiber@SiO2 superhydrophobic fabric for oil/water separation. *Microchem. J.* 202:110808. https://doi.org/10.1016/j.microc.2024.110808

16 Chen H, Yang J, Su J, Cui Y (**2022**) Facile fabrication of biobased porous material via the photocuring technique and a template-assisted approach for oil/water separation. Sep. *Purif. Technol.* 303:122239. https://doi.org/10.1016/j.seppur.2022.122239

17 Manapat JZ, Chen Q, Ye P, Advincula RC (**2017**) 3D Printing of Polymer Nanocomposites via Stereolithography. *Macromol. Mater. Eng.* 302:1600553. https://doi.org/10.1002/mame.201600553

18 Hong H, Seo YB, Kim DY, Lee JS, Lee YJ, Lee H, Ajiteru O, Sultan MT, Lee OJ, Kim SH, Park CH (**2020**) Digital light processing 3D printed silk fibroin hydrogel for cartilage tissue engineering. *Biomaterials* 232:119679. https://doi.org/10.1016/j.biomaterials.2019.119679

19 Schirmeister CG, Hees T, Licht EH, Mülhaupt R (**2019**) 3D printing of high density polyethylene by fused filament fabrication. *Addit. Manuf.* 28:152-9. https://doi.org/10.1016/j.addma.2019.05.003

20 Kumar S, Singh R, Singh T, Batish A (**2020**) Fused filament fabrication: A comprehensive review. *J. Thermoplast. Compos. Mater.* 36:794-814. https://doi.org/10.1177/0892705720970629

21 Samykano M, Kumaresan R, Kananathan J, Kadirgama K, Pandey AK (**2024**) An overview of fused filament fabrication technology and the advancement in PLA-biocomposites. *Int. J. Adv. Manuf. Technol.* 132:27-62. https://doi.org/10.1007/s00170-024-13394-1

22 Turner BN, Gold SA (**2015**) A review of melt extrusion additive manufacturing processes: II. Materials, dimensional accuracy, and surface roughness. *Rapid Prototyp. J.* 21:250-61. https://doi.org/10.1108/RPJ-02-2013-0017

23 Varjani SJ, Upasani VN (**2017**) A new look on factors affecting microbial degradation of petroleum hydrocarbon pollutants. *Int. Biodeterior. Biodegrad.* 120:71-83. https://doi.org/10.1016/j.ibiod.2017.02.006

24 Alegbeleye OO, Opeolu BO, Jackson VA (**2017**) Polycyclic Aromatic Hydrocarbons: A Critical Review of Environmental Occurrence and Bioremediation. *Environ. Manage.* 60:758-83. https://doi.org/10.1007/s00267-017-0896-2

25 Ng AKY, Song S (**2010**) The environmental impacts of pollutants generated by routine shipping operations on ports. *Ocean Coast. Manag.* 53:301-11. https://doi.org/10.1016/j.ocecoaman.2010.03.002

26 Pintor AMA, Vilar VJP, Botelho CMS, Boaventura RAR (**2014**) Optimization of a primary gravity separation treatment for vegetable oil refinery wastewaters. *Clean Technol. Environ. Policy* 16:1725-34. https://doi.org/10.1007/s10098-014-0754-3

27 Broje V, Keller AA (**2006**) Improved Mechanical Oil Spill Recovery Using an Optimized Geometry for the Skimmer Surface. *Environ. Sci. Technol.* 40:7914-8. https://doi.org/10.1021/es061842m

28 Chapman H, Purnell K, Law RJ, Kirby MF (**2007**) The use of chemical dispersants to combat oil spills at sea: A review of practice and research needs in Europe. *Mar. Pollut. Bull.* 54:827-38. https://doi.org/10.1016/j.marpolbul.2007.03.012

29 Mullin JV, Champ MA (**2003**) Introduction/Overview to In Situ Burning of Oil Spills. *Spill Sci. Technol. Bull.* 8:323-30. https://doi.org/10.1016/S1353-2561(03)00076-8

30 Ron EZ, Rosenberg E (**2014**) Enhanced bioremediation of oil spills in the sea. *Curr. Opin. Biotechnol.* 27:191-4. https://doi.org/10.1016/j.copbio.2014.02.004

31 Matilda MI, Samuel HS (**2024**) Bioremediation of oil spill: concept, methods and applications. *Discov. chem.* 1:42. https://doi.org/10.1007/s44371-024-00038-2

32 Fingas M (**2011**) Oil Spill Science and Technology: Prevention, Response, and Cleanup. *Gulf Professional Publishing, Oxford*. https://doi.org/10.1016/C2009-0-21572-2

33 Zhu Q, Pan Q, Liu F (**2014**) Oil–water separation with selective superantiwetting–superwetting surfaces: recent developments and future perspectives. *Chem Soc Rev* 43:4335–4358. https://doi.org/10.1039/C3CS60415G

34 Niu H, Luo S, Yao X, Li T, Ai M, Zhou R, Wang H, Wan L, Du Y, Hu L, Xu B, Xu J (**2023**) A review of transparent superhydrophobic materials and their research in the field of photovoltaic dust removal. *Mater. Sci. Semicond. Process.* 166:107741. https://doi.org/10.1016/j.mssp.2023.107741

35 Latthe SS, Sutar RS, Kodag VS, Bhosale AK, Kumar AM, Kumar Sadasivuni K, Xing R, Liu S (**2019**) Self – cleaning superhydrophobic coatings: Potential industrial applications. *Prog. Org. Coat.* 128:52-8. https://doi.org/10.1016/j.porgcoat.2018.12.008

36 Rasitha TP, Krishna NG, Anandkumar B, Vanithakumari SC, Philip J (**2024**) A comprehensive review on anticorrosive/antifouling superhydrophobic coatings: Fabrication, assessment, applications, challenges and future perspectives. *Adv. Colloid Interface Sci.* 324:103090. https://doi.org/10.1016/j.cis.2024.103090

37 Wang B, Zhang Y, Shi L, Li J, Guo Z (**2012**) Advances in the theory of superhydrophobic surfaces. *J. Mater. Chem.* 22:20112-27. https://doi.org/10.1039/C2JM32780E

38 Erbil HY, Cansoy CE (**2009**) Range of Applicability of the Wenzel and Cassie−Baxter Equations for Superhydrophobic Surfaces. *Langmuir* 25:14135-45. https://doi.org/10.1021/la902098a

39 Gao N, Yan Y (**2009**) Modeling Superhydrophobic Contact Angles and Wetting Transition. *J. Bionic Eng.* 6:335-40. https://doi.org/10.1016/S1672-6529(08)60135-3

40 He S, Zhu Z, Zhang B, Tian Y (**2023**) Wetting thresholds for long-lasting superwettability: From intrinsic wetting boundary to critical roughness value. *Chem. Eng. J.* 454:140058. https://doi.org/10.1016/j.cej.2022.140058

41 Xue Z, Cao Y, Liu N, Feng L, Jiang L (**2014**) Special wettable materials for oil/water separation. *J. Mater. Chem. A* 2:2445-60. https://doi.org/10.1039/C3TA13397D

42 Liang Y, Kim S, Kallem P, Choi H (**2019**) Capillary effect in Janus electrospun nanofiber membrane for oil/water emulsion separation. *Chemosphere* 221:479-85. https://doi.org/10.1016/j.chemosphere.2019.01.048

43 Yan X, Xiao X, Au C, Mathur S, Huang L, Wang Y, Zhang Z, Zhu Z, Kipper MJ, Tang J, Chen J (**2021**) Electrospinning nanofibers and nanomembranes for oil/water separation. *J. Mater. Chem. A* 9:21659-84. https://doi.org/10.1039/D1TA05873H

44 Li J-J, Zhu L-T, Luo Z-H (**2016**) Electrospun fibrous membrane with enhanced swithchable oil/water wettability for oily water separation. *Chem. Eng. J.* 287:474-81. https://doi.org/10.1016/j.cej.2015.11.057

45 Lu T, Cui J, Qu Q, Wang Y, Zhang J, Xiong R, Ma W, Huang C (**2021**) Multistructured Electrospun Nanofibers for Air Filtration: A Review. *ACS Appl. Mater. Interfaces* 13:23293-313. https://doi.org/10.1021/acsami.1c06520

46 Cao H, Chai S, Tan Z, Wu H, Mao X, Wei L, Zhou F, Sun R, Liu C (**2023**) Recent Advances in Physical Sensors Based on Electrospinning Technology. *ACS Mater. Lett.* 5:1627-48. https://doi.org/10.1021/acsmaterialslett.3c00144

47 Tai MH, Gao P, Tan BYL, Sun DD, Leckie JO (**2014**) Highly Efficient and Flexible Electrospun Carbon–Silica Nanofibrous Membrane for Ultrafast Gravity-Driven Oil–Water Separation. *ACS Appl. Mater. Interfaces* 6:9393-401. https://doi.org/10.1021/am501758c

48 Sun X, Bai L, Li J, Huang L, Sun H, Gao X (**2021**) Robust preparation of flexibly super-hydrophobic carbon fiber membrane by electrospinning for efficient oil-water separation in harsh environments. *Carbon* 182:11-22. https://doi.org/10.1016/j.carbon.2021.05.047

49 Luo Y, Sun Y, An S, Wei P, Wang S, Li Z, Pan Y, Li F (**2025**) Janus Composite Porous Structure with Asymmetric Selective-Wettability for Unidirectional Liquid Transportation and High-Efficiency Oil–Water Separation. *ACS Appl. Mater. Interfaces* 17:31654-66. https://doi.org/10.1021/acsami.5c06797

50 Su Y, Fan T, Cui W, Li Y, Ramakrishna S, Long Y (**2022**) Advanced Electrospun Nanofibrous Materials for Efficient Oil/Water Separation. *Adv. Fiber Mater.* 4:938-58. https://doi.org/10.1007/s42765-022-00158-3

51 Mailley D, Hébraud A, Schlatter G (**2021**) A Review on the Impact of Humidity during Electrospinning: From the Nanofiber Structure Engineering to the Applications. *Macromol. Mater. Eng.* 306:2100115. https://doi.org/10.1002/mame.202100115

52 Han Y, Xu Y, Zhang S, Li T, Ramakrishna S, Liu Y (**2020**) Progress of Improving Mechanical Strength of Electrospun Nanofibrous Membranes. *Macromol. Mater. Eng.* 305:2000230. https://doi.org/10.1002/mame.202000230

53 Worajittiphon P, Majan P, Wangkawong K, Somsunan R, Jantrawut P, Panraksa P, Chaiwarit T, Srithep Y, Sommano SR, Jantanasakulwong K, Rachtanapun P (**2024**) Inside-out templating: A strategy to decorate helical carbon nanotubes and 2D MoS2 on ethyl cellulose sponge for enhanced oil adsorption and oil/water separation. International Journal of Biological *Macromolecules* 273:133119. https://doi.org/10.1016/j.ijbiomac.2024.133119

54 Xue Z, Xing X, Zhu S, Zhang W, Luan L, Niu Y, Bai L, Chen H, Tao Q (**2019**) Underwater superoleophobic porous hydrogel film prepared by soluble salt-template method for oil/water separation in complex environments. *Desalin. Water Treat.* 164:151-61. https://doi.org/10.5004/dwt.2019.24456

55 Yu C, Yu C, Cui L, Song Z, Zhao X, Ma Y, Jiang L (**2017**) Facile Preparation of the Porous PDMS Oil-Absorbent for Oil/Water Separation. *Adv. Mater. Interfaces* 4:1600862. https://doi.org/10.1002/admi.201600862

56 Turco A, Primiceri E, Frigione M, Maruccio G, Malitesta C (**2017**) An innovative, fast and facile soft-template approach for the fabrication of porous PDMS for oil–water separation. *J. Mater. Chem. A* 5:23785-93. https://doi.org/10.1039/C7TA06840A

57 Zhao C, Chen L, Yu C, Hu B, Huang H, Chen Y, Wang X, Ye Y, Zhuang X, Li Y (**2021**) Fabrication of hydrophobic NiFe2O4@poly(DVB–LMA) sponge via a Pickering emulsion template method for oil/water separation. *Soft Matter* 17:2327-39. https://doi.org/10.1039/D0SM01902J

58 El Ghoul J, El Mir L (**2014**) Sol–gel synthesis and luminescence of undoped and Mn-doped zinc orthosilicate phosphor nanocomposites. *J. Lumin.* 148:82-8. https://doi.org/10.1016/j.jlumin.2013.11.090

59 Wu X, Fan M, Shen X, Cui S, Tan G (**2018**) Silica aerogels formed from soluble silicates and methyl trimethoxysilane (MTMS) using CO2 gas as a gelation agent. *Ceram. Int.* 44:821-9. https://doi.org/10.1016/j.ceramint.2017.10.005

60 Gupta S, Lalwani R, Gupta M, Sahu PK, Onkarnath, Banerjee S (**2025**) Impact of Dy ion on the structure and optoelectronic properties of CdO thin films: sol-gel spin coating method. *Appl. Phys. A* 131:561. https://doi.org/10.1007/s00339-025-08690-w

61 Fan S, Kunthom R, Meng Y, Kostjuk SV, Liu H (**2025**) Superhydrophobic fabric coated with double-decker silsesquioxane-based hybrid polymer for efficient oil/water separation and enhanced antifouling performance. *Cellulose* https://doi.org/10.1007/s10570-025-06593-w

62 Taurino R, Fabbri E, Messori M, Pilati F, Pospiech D, Synytska A (**2008**) Facile preparation of superhydrophobic coatings by sol–gel processes. *J. Colloid Interface Sci.* 325:149-56. https://doi.org/10.1016/j.jcis.2008.05.007

63 Xie A, Cui J, Chen Y, Lang J, Li C, Yan Y, Dai J (**2019**) One-step facile fabrication of sustainable cellulose membrane with superhydrophobicity via a sol-gel strategy for efficient oil/water separation. *Surf. Coat. Technol.* 361:19-26. https://doi.org/10.1016/j.surfcoat.2019.01.040

64 Akbarzadeh R, Yousefi A-M (**2014**) Effects of processing parameters in thermally induced phase separation technique on porous architecture of scaffolds for bone tissue engineering. *J. Biomed. Mater. Res. – B Appl. Biomater.* 102:1304-15. https://doi.org/10.1002/jbm.b.33101

65 Zuo J-H, Li Z-K, Wei C, Yan X, Chen Y, Lang W-Z (**2019**) Fine tuning the pore size and permeation performances of thermally induced phase separation (TIPS) -prepared PVDF membranes with saline water as quenching bath. *J. Membr. Sci.* 577:79-90. https://doi.org/10.1016/j.memsci.2019.02.005

66 Wang X, Pan Y, Liu X, Liu H, Li N, Liu C, Schubert DW, Shen C (**2019**) Facile Fabrication of Superhydrophobic and Eco-Friendly Poly(lactic acid) Foam for Oil–Water Separation via Skin Peeling. *ACS Appl. Mater. Interfaces* 11:14362-7. https://doi.org/10.1021/acsami.9b02285

67 Dehban A, Hosseini Saeedavi F, Kargari A (**2022**) A study on the mechanism of pore formation through VIPS-NIPS technique for membrane fabrication. *J. Ind. Eng. Chem.* 108:54-71. https://doi.org/10.1016/j.jiec.2021.12.023

68 Hai A, Durrani AA, Selvaraj M, Banat F, Haija MA (**2019**) Oil-water emulsion separation using intrinsically superoleophilic and superhydrophobic PVDF membrane. *Sep. Purif. Technol.* 212:388-95. https://doi.org/10.1016/j.seppur.2018.10.001

69 Lewis JA (**2006**) Direct ink writing of 3D functional materials. *Adv Funct Mater* 16:2193–2204. https://doi.org/10.1002/adfm.200600434

70 Liu K, Jiang L (**2016**) Design and creation of superwetting/antiwetting surfaces and their applications in oil–water separation. *Adv Mater* 28:7034–7057. https://doi.org/10.1002/adma.201602381

71 Song J, Guo X (**2018**) Superhydrophobic materials: a review on recent progress and applications. *J Mater Chem A* 6:21189–21212. https://doi.org/10.1039/C8TA07597A

72 Zhang W, Zhu Y, Liu X, Wang S, Jiang L (**2013**) Superhydrophobic membranes for oil–water separation. *Adv Mater* 25:2071–2076. https://doi.org/10.1002/adma.201203711

73 Barthlott W, Neinhuis C (**1997**) Purity of the sacred lotus, or escape from contamination in biological surfaces. *Planta* 202:1-8. https://doi.org/10.1007/s004250050096

74 Ghasemlou M, Daver F, Ivanova EP, Adhikari B (**2019**) Bio-inspired sustainable and durable superhydrophobic materials: from nature to market. *J. Mater. Chem. A* 7:16643-70. https://doi.org/10.1039/C9TA05185F

75 Koch K, Bhushan B, Barthlott W (**2009**) Multifunctional Surface Structures of Plants: An Inspiration for Biomimetics. *Prog. Mater. Sci.* 54:137-78. https://doi.org/10.1016/j.pmatsci.2008.07.003

76 Liu W, Chen H, Shen Y, Wu Z (**2019**) Facilely fabricating superhydrophobic resin-based coatings with lower water freezing temperature and ice adhesion for anti-icing application. *J. Bio. Eng.* 16:794-805. https://doi.org/10.1007/s42235-019-0097-1

77 Webb H, Hasan J, Truong VK, Crawford R, Ivanova E (**2011**) Nature inspired structured surfaces for biomedical applications. *Curr. Med. Chem.* 18:3367-75. https://doi.org/10.2174/092986711796504673

78 Zheng Y, Bai H, Huang Z, Tian X, Nie FQ, Zhao Y, Zhai J, Jiang L (**2010**) Directional water collection on wetted spider silk. *Nature* 463:640-3. https://doi.org/10.1038/nature08729

79 Chen H, Zhang P, Zhang L, Liu H, Jiang Y, Zhang D, Han Z, Jiang L (**2016**) Continuous directional water transport on the peristome surface of Nepenthes alata. *Nature* 532:85-9. https://doi.org/10.1038/nature17189

80 Li DW, Wang HY, Liu Y, Wei DS, Zhao ZX (**2019**) Large-scale fabrication of durable and robust super-hydrophobic spray coatings with excellent repairable and anti-corrosion performance. *Chem. Eng. J.* 367:169-79. https://doi.org/10.1016/j.cej.2019.02.093

81 Darmanin T, Guittard F (**2014**) Recent advances in the potential applications of bioinspired superhydrophobic materials. *J. Mater. Chem. A* 2:16319-59. https://doi.org/10.1039/C4TA02071E

82 Wang N, Xiong D, Deng Y, Shi Y, Wang K (**2015**) Mechanically robust superhydrophobic steel surface with anti-icing, uv-durability, and corrosion resistance properties. *ACS Appl. Mater. Interfaces* 7:6260-72. https://doi.org/10.1021/acsami.5b00558

83 Lai Y, Tang Y, Gong J, Gong D, Chi L, Lin C, Chen Z (**2012**) Transparent superhydrophobic/superhydrophilic TiO2-based coatings for self-cleaning and anti-fogging. *J. Mater. Chem.* 22:7420-6. https://doi.org/10.1039/C2JM16298A

84 Ge J, Shi L, Wang Y, Zhao H, Yao H, Zhu Y, Zhang Y, Zhu H, Wu H, Yu S (**2017**) Joule-heated graphene-wrapped sponge enables fast clean-up of viscous crude-oil spill. *Nat. Nanotechnol.* 12:434-40. https://doi.org/10.1038/nnano.2017.33

85 Banerjee S, Dionysiou DD, Pillai SC (**2015**) Self-cleaning applications of TiO2 by photo-induced hydrophilicity and photocatalysis. *Appl. Catal., B* 176-177:396-428. https://doi.org/10.1016/j.apcatb.2015.03.058

86 Su B, Tian Y, Jiang L (**2016**) Bioinspired interfaces with superwettability: from materials to chemistry. *J. Am. Chem. Soc.* 138:1727-48. https://doi.org/10.1021/jacs.5b12728

87 Wang D, Sun Q, Hokkanen MJ, Zhang C, Lin F-Y, Liu Q, Zhu S-P, Zhou T, Chang Q, He B, Zhou Q, Chen L, Wang Z, Ras RHA, Deng X (**2020**) Design of robust superhydrophobic surfaces. *Nature* 582:55-9. https://doi.org/10.1038/s41586-020-2331-8

88 Zhang S, Huang J, Chen Z, Lai Y (**2017**) Bioinspired special wettability surfaces: from fundamental research to water harvesting applications. *Small* 13:1602992. https://doi.org/10.1002/smll.201602992

89 El-Atab N, Qaiser N, Badghaish H, Shaikh SF, Hussain MM (**2020**) Flexible nanoporous template for the design and development of reusable anti-covid-19 hydrophobic face masks. *ACS Nano* 14:7659-65. https://doi.org/10.1021/acsnano.0c03976

90 Jiang W, Zhang X, Liu P, Zhang Y, Song W, Yu DG, Lu X (**2022**) Electrospun healthcare nanofibers from medicinal liquor of Phellinus igniarius. *Adv. Compos. Hybrid Mater.* 5:3045-56. https://doi.org/10.1007/s42114-022-00551-x

91 Wang M, Ge R, Zhao P, Williams GR, Yu DG, Bligh SWA (**2023**) Exploring wettability difference-driven wetting by utilizing electrospun chimeric Janus microfiber comprising cellulose acetate and polyvinylpyrrolidone. *Mater. Des.* 226:111652. https://doi.org/10.1016/j.matdes.2023.111652

92 Wang M, Hou J, Yu DG, Li S, Zhu J, Chen Z (**2020**) Electrospun tri-layer nanodepots for sustained release of acyclovir. *J. Alloys Compd.* 846:156471. https://doi.org/10.1016/j.jallcom.2020.156471

93 Wang X, Pan Y, Yuan H, Su M, Shao C, Liu C, Guo Z, Shen C, Liu X (**2020**) Simple fabrication of superhydrophobic PLA with honeycomb-like structures for high-efficiency oil-water separation. *Chin. Chem. Lett.* 31:365-8. https://doi.org/10.1016/j.cclet.2019.07.044

94 Wang X, Pan Y, Shen C, Liu C, Liu X (**2018**) Facile thermally impacted water-induced phase separation approach for the fabrication of skin-free thermoplastic polyurethane foam and its' recyclable counterpart for oil–water separation. *Macromol. Rapid Commun.* 39:1800635. https://doi.org/10.1002/marc.201800635

95 Choi SJ, Kwon TH, Im H, Moon DI, Baek DJ, Seol ML, Duarte JP, Choi YK (**2011**) A polydimethylsiloxane (pdms) sponge for the selective absorption of oil from water. *ACS Appl. Mater. Interfaces* 3:4552-6. https://doi.org/10.1021/am201352w

96 Wang Y, Liu X, Lian M, Zheng G, Dai K, Guo Z, Liu C, Shen C (**2017**) Continuous fabrication of polymer microfiber bundles with interconnected microchannels for oil/water separation. *Appl. Mater. Today* 9:77-81. https://doi.org/10.1016/j.apmt.2017.05.007

97 Zhang X, Wang X, Liu X, Lv C, Wang Y, Zheng G, Liu H, Liu C, Guo Z, Shen C (**2018**) Porous polyethylene bundles with enhanced hydrophobicity and pumping oil-recovery ability via skin-peeling. *ACS Sustainable Chem. Eng.* 6:12580-5. https://doi.org/10.1021/acssuschemeng.8b03305

98 Liu J, Zhang HB, Sun R, Liu Y, Liu Z, Zhou A, Yu ZZ (**2017**) Hydrophobic, flexible, and lightweight mxene foams for high-performance electromagnetic-interference shielding. *Adv. Mater.* 29:1702367. https://doi.org/10.1002/adma.201702367

99 Liu G, Zhang X, Chen X, He Y, Cheng L, Huo M, Yin J, Hao F, Chen S, Wang P, Yi S, Wan L, Mao Z, Chen Z, Wang X, Cao Z, Lu J (**2021**) Additive manufacturing of structural materials. *Mater. Sci. Eng.: R: Rep.* 145:100596. https://doi.org/10.1016/j.mser.2020.100596

100 Yu DG, Zhu LM, Branford-White CJ, Yang XL (**2008**) Three-Dimensional Printing in Pharmaceutics: Promises and Problems. *J. Pharm. Sci.* 97:3666-90. https://doi.org/10.1002/jps.21284

101 Barahman M, Lyons AM (**2011**) Ratchetlike slip angle anisotropy on printed superhydrophobic surfaces. *Langmuir* 27:9902-9. https://doi.org/10.1021/la201222a

102 Yang Y, Li X, Zheng X, Chen Z, Zhou Q, Chen Y (**2018**) 3D-Printed biomimetic super-hydrophobic structure for microdroplet manipulation and oil/water separation. *Adv. Mater.* 30:1704912. https://doi.org/10.1002/adma.201704912

103 Peng L, Chen K, Chen D, Chen J, Tang J, Xiang S, Chen W, Liu P, Zheng F, Shi J (**2021**) Study on the enhancing water collection efficiency of cactus- and beetle-like biomimetic structure using UV-induced controllable diffusion method and 3D printing technology. *RSC Adv* 11:14769-76. https://doi.org/10.1039/D1RA00652E

104 Yang Y, Guo Z, Liu W (**2022**) Special superwetting materials from bioinspired to intelligent surface for on-demand oil/water separation: a comprehensive review. *Small* 18:2204624. https://doi.org/10.1002/smll.202204624

105 Young T (**1805**) III. An essay on the cohesion of fluids. Philos. *Trans. R. Soc. London* 95:65-87. https://doi.org/10.1098/rstl.1805.0005

106 Wenzel RN (**1936**) Resistance of solid surfaces to wetting by water. *Ind. Eng. Chem.* 28:988-94. https://doi.org/10.1021/ie50320a024

107 Cassie ABD, Baxter S (**1944**) Wettability of porous surfaces. *Trans. Faraday Soc.* 40:546-51. https://doi.org/10.1039/TF9444000546

108 Wang S, Liu K, Yao X, Jiang L (**2015**) Bioinspired surfaces with superwettability: new insight on theory, design, and applications. *Chem. Rev.* 115:8230-93. https://doi.org/10.1021/cr400083y

109 Liu M, Wang S, Jiang L (**2017**) Nature-inspired superwettability systems. *Nat. Rev. Mater. 2:17036.* https://doi.org/10.1038/natrevmats.2017.36

110 Feng XJ, Jiang L (**2006**) Design and creation of superwetting/antiwetting surfaces. *Adv. Mater.* 18:3063-78. https://doi.org/10.1002/adma.200501961

111 Zhang J, Liu H, Jiang L (**2017**) Membrane-based strategy for efficient ionic liquids/water separation assisted by superwettability. *Adv. Funct. Mater.* 27:1606544. https://doi.org/10.1002/adfm.201606544

112 Kwok DY, Neumann AW (**1999**) Contact angle measurement and contact angle interpretation. *Adv. Colloid Interface Sci.* 81:167-249. https://doi.org/10.1016/S0001-8686(98)00087-6

113 Wang L, Zhao Y, Tian Y, Jiang L (**2015**) A general strategy for the separation of immiscible organic liquids by manipulating the surface tensions of nanofibrous membranes. *Angew. Chem., Int. Ed.* 54:14732-7. https://doi.org/10.1002/anie.201506866

114 Wallin TJ, Pikul J, Shepherd RF (**2018**) 3D printing of soft robotic systems. *Nat. Rev. Mater.* 3:84-100. https://doi.org/10.1038/s41578-018-0002-2

115 Chen L, He Y, Yang Y, Niu S, Ren H (**2017**) The research status and development trend of additive manufacturing technology. *Int. J. Adv. Manuf. Technol.* 89:3651-60. https://doi.org/10.1007/s00170-016-9335-4

116 Jiang R, Kleer R, Piller FT (**2017**) Predicting the future of additive manufacturing: A Delphi study on economic and societal implications of 3D printing for 2030. *Technol. Forecast. Soc. Change* 117:84-97. https://doi.org/10.1016/j.techfore.2017.01.006

117 Rahman Z, Barakh Ali SF, Ozkan T, Charoo NA, Reddy IK, Khan MA (**2018**) Additive manufacturing with 3d printing: progress from bench to bedside. *AAPS J.* 20:101. https://doi.org/10.1208/s12248-018-0225-6

118 Bourell D, Kruth JP, Leu M, Levy G, Rosen D, Beese AM, Clare A (**2017**) Materials for additive manufacturing. *CIRP Annals* 66:659-81. https://doi.org/10.1016/j.cirp.2017.05.009

119 Beltagui A, Rosli A, Candi M (**2020**) Exaptation in a digital innovation ecosystem: The disruptive impacts of 3D printing. *Res. Policy* 49:103833. https://doi.org/10.1016/j.respol.2019.103833

120 West J, Kuk G (**2016**) The complementarity of openness: how makerbot leveraged thingiverse in 3d printing. Technol. *Forecast. Soc. Change* 102:169-81. https://doi.org/10.1016/j.techfore.2015.07.025

121 Yan C, Jiang P, Jia X, Wang X (**2020**) 3D printing of bioinspired textured surfaces with superamphiphobicity. *Nanoscale* 12:2924-38. https://doi.org/10.1039/C9NR09620E

122 Alexandre A, Cruz Sanchez FA, Boudaoud H, Camargo M, Pearce JM (**2020**) Mechanical properties of direct waste printing of polylactic acid with universal pellets extruder: comparison to fused filament fabrication on open-source desktop three-dimensional printers. *3D Print. Addit. Manuf.* 7:237-47. https://doi.org/10.1089/3dp.2019.0195

123 Lee KM, Park H, Kim J, Chun DM (**2019**) Fabrication of a superhydrophobic surface using a fused deposition modeling (FDM) 3D printer with poly lactic acid (PLA) filament and dip coating with silica nanoparticles. *Appl. Surf. Sci.* 467-468:979-91. https://doi.org/10.1016/j.apsusc.2018.10.205

124 Mohamed OA, Masood SH, Bhowmik JL, Nikzad M, Azadmanjiri J (**2016**) Effect of process parameters on dynamic mechanical performance of fdm pc/abs printed parts through

design of experiment. *J. Mater. Eng. Perform.* 25:2922-35. https://doi.org/10.1007/s11665-016-2157-6

125 Chen Q, Mangadlao JD, Wallat J, De Leon A, Pokorski JK, Advincula RC (**2017**) 3D printing biocompatible polyurethane/poly (lactic acid)/graphene oxide nanocomposites: anisotropic properties. *ACS Appl. Mater. Interfaces* 9:4015-23. https://doi.org/10.1021/acsami.6b11793

126 Ning F, Cong W, Qiu J, Wei J, Wang S (**2015**) Additive manufacturing of carbon fiber reinforced thermoplastic composites using fused deposition modeling. *Composites, Part B* 80:369-78. https://doi.org/10.1016/j.compositesb.2015.06.013

127 Tu Y, Arrieta-Escobar JA, Hassan A, Zaman UKu, Siadat A, Yang G (**2021**) Optimizing process parameters of direct ink writing for dimensional accuracy of printed layers. *3D Print. Addit. Manuf.* https://doi.org/10.1089/3dp.2021.0208

128 Tu Y, Hassan A, Arrieta-Escobar JA, Zaman UKu, Siadat A, Yang G (**2022**) Modeling and evaluation of freeform extruded filament based on numerical simulation method for direct ink writing. *Int. J. Adv. Manuf. Technol.* 120:3821-9. https://doi.org/10.1007/s00170-022-08999-3

129 Tu Y, Hassan A, Siadat A, Yang G, Chen Z (**2022**) Numerical simulation and experimental validation of deposited corners of any angle in direct ink writing. *Int. J. Adv. Manuf. Technol.* 123:559-70. https://doi.org/10.1007/s00170-022-10195-2

130 Tu Y, Hassan A, Siadat A, Yang G (**2022**) Analytical modeling of deposited filaments for high viscosity material-based piston-driven direct ink writing. *Int. J. Adv. Manuf. Technol.* 123:3387-98. https://doi.org/10.1007/s00170-022-10511-w

131 Badea A, McCracken JM, Tillmaand EG, Kandel ME, Oraham AW, Mevis MB, Rubakhin SS, Popescu G, Sweedler JV, Nuzzo RG (**2017**) 3D-Printed pHEMA materials for topographical and biochemical modulation of dorsal root ganglion cell response. *ACS Appl. Mater. Interfaces* 9:30318-28. https://doi.org/10.1021/acsami.7b06742

132 Jiang P, Yan C, Guo Y, Zhang X, Cai M, Jia X, Wang X, Zhou F (**2019**) Direct ink writing with high-strength and swelling-resistant biocompatible physically crosslinked hydrogels. *Biomater. Sci.* 7:1805-14. https://doi.org/10.1039/C9BM00081J

133 Li V, Mulyadi A, Dunn CK, Deng Y, Qi HJ (**2018**) Direct ink write 3d printed cellulose nanofiber aerogel structures with highly deformable, shape recoverable, and functionalizable

properties. *ACS Sustainable Chem. Eng.* 6:2011-22. https://doi.org/10.1021/acssuschemeng.7b03439

134 Yuan S, Strobbe D, Li X, Kruth JP, Van Puyvelde P, Van der Bruggen B (**2020**) 3D printed chemically and mechanically robust membrane by selective laser sintering for separation of oil/water and immiscible organic mixtures. *Chem. Eng. J.* 385:123816. https://doi.org/10.1016/j.cej.2019.123816

135 Jiao L, Chua ZY, Moon SK, Song J, Bi G, Zheng H (**2018**) Femtosecond laser produced hydrophobic hierarchical structures on additive manufacturing parts. *Nanomater.* 8(8):601. https://doi.org/10.3390/nano8080601

136 Lawson S, Al-Naddaf Q, Krishnamurthy A, Amour MS, Griffin C, Rownaghi AA, Knox JC, Rezaei F (**2018**) UTSA-16 Growth within 3D-printed Co-Kaolin monoliths with high selectivity for CO2/CH4, CO2/N2, and CO2/H2 Separation. *ACS Appl. Mater. Interfaces* 10:19076-86. https://doi.org/10.1021/acsami.8b05192

137 Shin J, Jeong B, Kim J, Nam VB, Yoon Y, Jung J, Hong S, Lee H, Eom H, Yeo J, Choi J, Lee D, Ko SH (**2020**) Sensitive wearable temperature sensor with seamless monolithic integration. *Adv. Mater.* 32:1905527. https://doi.org/10.1002/adma.201905527

138 Al Jabbari YS, Koutsoukis T, Barmpagadaki X, Zinelis S (**2014**) Metallurgical and interfacial characterization of PFM Co–Cr dental alloys fabricated via casting, milling or selective laser melting. *Dent. Mater.* 30:79-88. https://doi.org/10.1016/j.dental.2014.01.008

139 McManus D, Vranic S, Withers F, Sanchez-Romaguera V, Macucci M, Yang H, Sorrentino R, Parvez K, Son SK, Iannaccone G, Kostarelos K, Fiori G, Casiraghi C (**2017**) Water-based and biocompatible 2D crystal inks for all-inkjet-printed heterostructures. *Nat. Nanotechnol.* 12:343-50. https://doi.org/10.1038/nnano.2016.281

140 Zhu D, Wang Z, Zhu D (**2020**) Highly conductive graphene electronics by inkjet printing. *J. Electron. Mater.* 49:1765-76. https://doi.org/10.1007/s11664-019-07920-1

141 Secor EB, Prabhumirashi PL, Puntambekar K, Geier ML, Hersam MC (**2013**) Inkjet printing of high conductivity, flexible graphene patterns. *J. Phys. Chem. Lett.* 4:1347-51. https://doi.org/10.1021/jz400644c

142 Bloomquist CJ, Mecham MB, Paradzinsky MD, Januszewicz R, Warner SB, Luft JC, Mecham SJ, Wang AZ, DeSimone JM (**2018**) Controlling release from 3D printed medical devices using CLIP and drug-loaded liquid resins. *J. Control.* 278:9-23. https://doi.org/10.1016/j.jconrel.2018.03.026

143 Tumbleston JR, Shirvanyants D, Ermoshkin N, Januszewicz R, Johnson AR, Kelly D, Chen K, Pinschmidt R, Rolland JP, Ermoshkin A, Samulski ET, DeSimone JM (**2015**) Continuous liquid interface production of 3D objects. *Science* 347:1349-52. https://doi.org/10.1126/science.aaa2397

144 van Lith R, Baker E, Ware H, Yang J, Farsheed AC, Sun C, Ameer G (**2016**) 3D-Printing strong high-resolution antioxidant bioresorbable vascular stents. *Adv. Mater. Technol.* 1:1600138. https://doi.org/10.1002/admt.201600138

145 Melchels FPW, Feijen J, Grijpma DW (**2010**) A review on stereolithography and its' applications in biomedical engineering. *Biomater.* 31:6121-30. https://doi.org/10.1016/j.biomaterials.2010.04.050

146 Kim SY, Shin YS, Jung HD, Hwang CJ, Baik HS, Cha J-Y (**2018**) Precision and trueness of dental models manufactured with different 3-dimensional printing techniques. *Am. J. Orthod. Dentofac. Orthop.* 153:144-53. https://doi.org/10.1016/j.ajodo.2017.05.025

147 Wang J, Goyanes A, Gaisford S, Basit AW (**2016**) Stereolithographic (SLA) 3D printing of oral modified-release dosage forms. *Int. J. Pharm.* 503:207-12. https://doi.org/10.1016/j.ijpharm.2016.03.016

148 Dehurtevent M, Robberecht L, Hornez JC, Thuault A, Deveaux E, Béhin P (**2017**) Stereolithography: A new method for processing dental ceramics by additive computer-aided manufacturing. *Dent. Mater.* 33:477-85. https://doi.org/10.1016/j.dental.2017.01.018

149 Krkobabić M, Medarević D, Cvijić S, Grujić B, Ibrić S (**2019**) Hydrophilic excipients in digital light processing (DLP) printing of sustained release tablets: Impact on internal structure and drug dissolution rate. Int. J. Pharm. 572:118790. https://doi.org/10.1016/j.ijpharm.2019.118790

150 Bernal PN, Bouwmeester M, Madrid-Wolff J, Falandt M, Florczak S, Rodriguez NG, Li Y, Größbacher G, Samsom R-A, van Wolferen M, van der Laan LJW, Delrot P, Loterie D, Malda J, Moser C, Spee B, Levato R (**2022**) Volumetric bioprinting of organoids and optically tuned hydrogels to build liver-like metabolic biofactories. *Adv. Mater.* 34:2110054. https://doi.org/10.1002/adma.202110054

151 Ge Q, Li Z, Wang Z, Kowsari K, Zhang W, He X, Zhou J, Fang NX (**2020**) Projection micro stereolithography based 3D printing and its applications. *Int. J. Extreme Manuf.* 2:022004. https://doi.org/10.1088/2631-7990/ab8d9a

152 Ertugrul I (**2020**) The fabrication of micro beam from photopolymer by digital light processing 3d printing technology. *Micromachines* 11(5):518. https://doi.org/10.3390/mi11050518

153 Xing JF, Zheng ML, Duan XM (**2015**) Two-photon polymerization microfabrication of hydrogels: an advanced 3D printing technology for tissue engineering and drug delivery. *Chem. Soc. Rev.* 44:5031-9. https://doi.org/10.1039/C5CS00278H

154 Ngo TD, Kashani A, Imbalzano G, Nguyen KTQ, Hui D (**2018**) Additive manufacturing (3D printing): A review of materials, methods, applications and challenges. *Compos. B Eng.* 143:172-96. https://doi.org/10.1016/j.compositesb.2018.02.012

155 Moura CS, Ferreira FC, Bártolo PJ (**2016**) Comparison of Three-dimensional Extruded Poly (ε-Caprolactone) and Polylactic acid Scaffolds with Pore size Variation. *Procedia CIRP* 49:209-12. https://doi.org/10.1016/j.procir.2015.11.018

156 Cheng C, Gupta M (**2017**) Surface functionalization of 3D-printed plastics via initiated chemical vapor deposition. *Beilstein J. Nanotechnol.* 8:1629-36. https://doi.org/10.3762/bjnano.8.162

157 Slegers S, Linzas M, Drijkoningen J, D'Haen J, Reddy NK, Deferme W (**2017**) Surface Roughness Reduction of Additive Manufactured Products by Applying a Functional Coating Using Ultrasonic Spray Coating. *Coatings* 7(12): 208. https://doi.org/10.3390/coatings7120208

158 He Z, Chen Y, Yang J, Tang C, Lv J, Liu Y, Mei J, Lau W-m, Hui D (**2017**) Fabrication of Polydimethylsiloxane films with special surface wettability by 3D printing. *Compos. B Eng.* 129:58-65. https://doi.org/10.1016/j.compositesb.2017.07.025

159 Credi C, Levi M, Turri S, Simeone G (**2017**) Stereolithography of perfluoropolyethers for the microfabrication of robust omniphobic surfaces. *Appl. Surf. Sci.* 404:268-75. https://doi.org/10.1016/j.apsusc.2017.01.208

160 Wang X, Liu J, Yang L, He Y, Wang Y (**2018**) Nano-sized amorphous carbon covered surface formed by selective laser melting of ink-printed (SLM-IP) copper (Cu) nanoparticles (NPs). *Appl. Surf. Sci.* 448:133-7. https://doi.org/10.1016/j.apsusc.2018.04.109

161 Nargang TM, Dierkes R, Bruchmann J, Keller N, Sachsenheimer K, Lee-Thedieck C, Kotz F, Helmer D, Rapp BE (**2018**) Photolithographic structuring of soft, extremely foldable and autoclavable hydrophobic barriers in paper. *Anal. Methods* 10:4028-35. https://doi.org/10.1039/C8AY01010B

162 Li Y, Mao H, Hu P, Hermes M, Lim H, Yoon J, Luhar M, Chen Y, Wu W (**2019**) Bioinspired functional surfaces enabled by multiscale stereolithography. *Adv. Mater. Technol.* 4:1800638. https://doi.org/10.1002/admt.201800638

163 Anokhina TS, Ilyin SO, Ignatenko VY, Bakhtin DS, Kostyuk AV, Antonov SV, Volkov AV (**2019**) Formation of Porous Films with Hydrophobic Surface from a Blend of Polymers. *Polym. Sci. Ser. A* 61:619-26. https://doi.org/10.1134/S0965545X19050018

164 Kang B, Sung J, So H (**2021**) Realization of Superhydrophobic Surfaces Based on Three-Dimensional Printing Technology. *Int. J. Precis. Eng. Manuf.-Green Technol.* 8:47-55. https://doi.org/10.1007/s40684-019-00163-9

165 Pajarito B, Cayabyab C, Costales P, Francisco J (**2019**) Exfoliated graphite/acrylic composite film as hydrophobic coating of 3D-printed polylactic acid surfaces. J. Coat. Technol. Res. 16:1133-40. https://doi.org/10.1007/s11998-019-00188-4

166 Davoudinejad A, Cai Y, Pedersen DB, Luo X, Tosello G (**2019**) Fabrication of micro-structured surfaces by additive manufacturing, with simulation of dynamic contact angle. *Mater. Des.* 176:107839. https://doi.org/10.1016/j.matdes.2019.107839

167 Li X, Yang Y, Liu L, Chen Y, Chu M, Sun H, Shan W, Chen Y (**2020**) 3D-Printed cactus-inspired spine structures for highly efficient water collection. *Adv. Mater. Interfaces* 7:1901752. https://doi.org/10.1002/admi.201901752

168 Kaur G, Marmur A, Magdassi S (**2020**) Fabrication of superhydrophobic 3D objects by Digital Light Processing. *Addit. Manuf.* 36:101669. https://doi.org/10.1016/j.addma.2020.101669

169 Yu T, Guo W, Wang X, Liu J, Wang Y, Chen M (**2020**) Surface hydrophobicity and oleophilicity of hierarchical metal structures fabricated using ink-based selective laser melting of micro/nanoparticles. *Nanotechnol. Rev.* 9:626-36. https://doi:10.1515/ntrev-2020-0050

170 Zhang Y, Yin M-J, Ouyang X, Zhang AP, Tam H-Y (**2020**) 3D μ-printing of polytetrafluoroethylene microstructures: A route to superhydrophobic surfaces and devices. *Appl. Mater. Today* 19:100580. https://doi.org/10.1016/j.apmt.2020.100580

171 Männel MJ, Weigel N, Hauck N, Heida T, Thiele J (**2021**) Combining Hydrophilic and Hydrophobic Materials in 3D Printing for Fabricating Microfluidic Devices with Spatial Wettability. *Adv. Mater. Technol.* 6:2100094. https://doi.org/10.1002/admt.202100094

172 Yin Q, Guo Q, Wang Z, Chen Y, Duan H, Cheng P (**2021**) 3D-Printed Bioinspired Cassie–Baxter Wettability for Controllable Microdroplet Manipulation. *ACS Appl. Mater. Interfaces* 13:1979-87. https://doi.org/10.1021/acsami.0c18952

173 Ciffréo L, Marchand C, Szczepanski CA, Medici MG (**2021**) GA-O Bioinspired and Post-Functionalized 3D-Printed Surfaces with Parahydrophobic Properties. *Biomimetics* 6(4):71. https://doi.org/10.3390/biomimetics6040071

174 Lv C, Qi Y, Hu R, Zheng J (**2021**) Robust, healable and hydrophobically recoverable polydimethylsiloxane based supramolecular material with dual-activate hard segment. *Sci. China Technol. Sci.* 64:423-32. https://doi.org/10.1007/s11431-020-1674-7

175 Yan D, Wang Y, Liu J, Zhao D, Ming P, Song J (**2021**) Electrochemical 3D printing of superhydrophobic pillars with conical, cylindrical, and inverted conical shapes. *Colloids Surf. A Physicochem. Eng. Asp.* 625:126869. https://doi.org/10.1016/j.colsurfa.2021.126869

176 Specht M, Berwind M, Eberl C (**2021**) Adaptive Wettability of a Programmable Metasurface. *Adv. Eng. Mater.* 23:2001037. https://doi.org/https://doi.org/10.1002/adem.202001037

177 Jin Z, Mei H, Yan Y, Pan L, Liu H, Xiao S, Cheng L (**2021**) 3D-printed controllable gradient pore superwetting structures for high temperature efficient oil-water separation. *J. Materiomics* 7:8-18. https://doi.org/10.1016/j.jmat.2020.07.002

178 Farrell ES, Ganonyan N, Cooperstein I, Moshkovitz MY, Amouyal Y, Avnir D, Magdassi S (**2021**) 3D-printing of ceramic aerogels by spatial photopolymerization. *Appl. Mater. Today* 24:101083. https://doi.org/10.1016/j.apmt.2021.101083

179 Kim D, Sasidharanpillai A, Lee Y, Lee S (**2021**) Self-Stratified Versatile Coatings for Three-Dimensional Printed Underwater Physical Sensors Applications. *Nano Lett.* 21:6820-7. https://doi.org/10.1021/acs.nanolett.1c01770

180 Aldhaleai A, Tsai PA (**2021**) Fabrication of Transparent and Microstructured Superhydrophobic Substrates Using Additive Manufacturing. *Langmuir* 37:348-56. https://doi.org/10.1021/acs.langmuir.0c02945

181 Mayoussi F, Doeven EH, Kick A, Goralczyk A, Thomann Y, Risch P, Guijt RM, Kotz F, Helmer D, Rapp BE (**2021**) Facile fabrication of micro-/nanostructured, superhydrophobic membranes with adjustable porosity by 3D printing. *J. Mater. Chem. A* 9:21379-86. https://doi.org/10.1039/D1TA03352B

182 Mekhiel S, Koshy P, Elbestawi MA (**2021**) Additive texturing of metallic surfaces for wetting control. *Addit. Manuf.* 37:101631. https://doi.org/10.1016/j.addma.2020.101631

183 Mahmut ŞK, Remzi EE, Omer K, Abdul Q, Bekir S. (**2022**) Effect of Post Processes on Mechanical Properties of 3D Printed Ti6Al4V Gears. *J. Mater. Eng. Perform.* 31:6300-6309. https://doi.org/10.1080/2374068X.2021.1912539

184 Wu C, Wei X, Chen Y, Liu J, Guo C, Wang Q, Liang SY (**2022**) Surface wettability analysis and preparation of hydrophobic microcylindrical arrays by μ-SLA 3D printing. *J. Manuf. Process.* 83:14-26. https://doi.org/10.1016/j.jmapro.2022.08.041

185 Campos JA, Szczepanski CA, Medici MG, Godeau GA (**2022**) Inspired by the Nature: A Post-printed Strategy to Efficiently Elaborate Parahydrophobic Surfaces. *Biomimetics* 7(3):122. https://doi.org/10.3390/biomimetics7030122

186 Huang W, Nelson B, Tian S, Ordikhani-Seyedlar R, Auyeung RCY, Samanta A, Hu H, Shaw S, Lamuta C, Ding H (**2022**) Superhydrophobic surface processing for metal 3D printed parts. *Appl. Mater. Today* 29:101630. https://doi.org/10.1016/j.apmt.2022.101630

187 Barraza B, Olate-Moya F, Montecinos G, Ortega JH, Rosenkranz A, Tamburrino A, Palza H (**2022**) Superhydrophobic SLA 3D printed materials modified with nanoparticles biomimicking the hierarchical structure of a rice leaf. *Sci. Technol. Adv. Mater.* 23:300-21. https://doi.org/10.1080/14686996.2022.2063035

188 Chand R, Sharma VS, Trehan R, Verma R, Gupta MK, Srivastava S (**2023**) Developing Superhydrophobic Surface Using Multi Jet 3D Printing Durability Analysis. *J. Mater. Eng. Perform.* 32:1133-44. https://doi.org/10.1007/s11665-022-07154-z

189 Jiang D, Tian Y, Zhu Y, Huang A (**2022**) Investigation of surface roughness post-processing of additively manufactured nickel-based superalloy Hastelloy X using electropolishing. *Surf. Coat. Technol.* 441:128529. https://doi.org/10.1016/j.surfcoat.2022.128529

190 Xiang Y, Huang S, Huang TY, Dong A, Cao D, Li H, Xue Y, Lv P, Duan H (**2020**) Superrepellency of underwater hierarchical structures on Salvinia leaf. *Proc. Natl. Acad. Sci.* 117:2282-7. https://doi.org/10.1073/pnas.1900015117

191 Bonilla-Cruz J, Sy JAC, Lara-Ceniceros TE, Gaxiola-López JC, García V, Basilia BA, Advincula RC (**2021**) Superhydrophobic μ-pillars via simple and scalable SLA 3D-printing: the stair-case effect and their wetting models. *Soft Matter* 17:7524-31. https://doi.org/10.1039/D1SM00655J

192 Reeves PE, Cobb RC (**1997**) Reducing the surface deviation of stereolithography using in-process techniques. *Rapid Prototyping J.* 3:20-31. https://doi.org/10.1108/13552549710169255

193 Lv J, Gong Z, He Z, Yang J, Chen Y, Tang C, Liu Y, Fan M, Lau W-M (**2017**) 3D printing of a mechanically durable superhydrophobic porous membrane for oil–water separation. *J. Mater. Chem.* 5:12435-44. https://doi.org/10.1039/C7TA02202F

194 Wang Y, Willenbacher N (**2022**) Phase-change-enabled, rapid, high-resolution direct ink writing of soft silicone. *Adv. Mater.* 34:2109240. https://doi.org/10.1002/adma.202109240

195 Kim Y, Yuk H, Zhao R, Chester SA, Zhao X (**2018**) Printing ferromagnetic domains for untethered fast-transforming soft materials. *Nature* 558:274-9. https://doi.org/10.1038/s41586-018-0185-0

196 Rajakaruna RADNV, Subeshan B, Asmatulu E (**2022**) Fabrication of hydrophobic PLA filaments for additive manufacturing. *J. Mater. Sci.* 57:8987-9001. https://doi.org/10.1007/s10853-022-07217-5

197 Dong Z, Vuckovac M, Cui W, Zhou Q, Ras RHA, Levkin PA (**2021**) 3D printing of superhydrophobic objects with bulk nanostructure. *Adv. Mater.* 33:2106068. https://doi.org/10.1002/adma.202106068

198 Joyee EB, Szmelter A, Eddington D, Pan Y (**2020**) Magnetic field-assisted stereolithography for productions of multimaterial hierarchical surface structures. *ACS Appl. Mater. Interfaces* 12:42357-68. https://doi.org/10.1021/acsami.0c11693

199 Yang H, Ji F, Li Z, Tao S (**2020**) Preparation of hydrophobic surface on PLA and ABS by fused deposition modeling. *Polymers* 12(7):1539. https://doi.org/10.3390/polym12071539

200 Chen W, Zhang X, Tan D, Xu P, Yang B, Shi K, Zhu B, Liu Q, Lei Y, Liu S, Xue L (**2022**) Improvement in mechanical properties of 3d-printed peek structure by nonsolvent vapor annealing. *Macromol. Rapid Commun.* 43:2100874. https://doi.org/10.1002/marc.202100874

201 Wang J, Mubarak S, Dhamodharan D, Divakaran N, Wu L, Zhang X (**2020**) Fabrication of thermoplastic functionally gradient composite parts with anisotropic thermal conductive properties based on multicomponent fused deposition modeling 3D printing. *Compos Commun* 19:142-6. https://doi.org/10.1016/j.coco.2020.03.012

202 Shin JH, Heo JH, Jeon S, Park JH, Kim S, Kang HW (**2019**) Bio-inspired hollow PDMS sponge for enhanced oil–water separation. *J. Hazard. Mater.* 365:494-501. https://doi.org/10.1016/j.jhazmat.2018.10.078

203 Kang B, Hyeon J, So H (**2020**) Facile microfabrication of 3-dimensional (3D) hydrophobic polymer surfaces using 3D printing technology. *Appl. Surf. Sci.* 499:143733. https://doi.org/10.1016/j.apsusc.2019.143733

204 Guo Y, Luo B, Wang X, Liu S, Geng T (**2022**) Wettability control and oil/water separation performance of 3D-printed porous materials. *J. Appl. Polym. Sci.* 139:51570. https://doi.org/10.1002/app.51570

205 Atlas RM (**1991**) Microbial hydrocarbon degradation—bioremediation of oil spills. *J. Chem. Technol. Biotechnol.* 52:149-56. https://doi.org/10.1002/jctb.280520202

206 Lin Q, Mendelssohn IA, Carney K, Miles SM, Bryner NP, Walton WD (**2005**) In-situ burning of oil in coastal marshes. 2. oil spill cleanup efficiency as a function of oil type, marsh type, and water depth. environ. *Sci. Technol.* 39:1855-60. 10.1021/es0490626

207 Tan Z, Hu L, Yang D, Zheng D, Qiu X (**2023**) Lignin: Excellent hydrogel swelling promoter used in cellulose aerogel for efficient oil/water separation. *J. Colloid Interface Sci.* 629:422-33. https://doi.org/10.1016/j.jcis.2022.08.185

208 Yuan H, Zhang M, Pan Y, Liu C, Shen C, Chen Q, Liu X (**2022**) Microspheres modified with superhydrophobic non-woven fabric with high-efficiency oil–water separation: controlled water content in pla solution. *Macromol. Mater. Eng.* 307:2100919. https://doi.org/10.1002/mame.202100919

209 Han L, Chen C, Shen L, Lin H, Li B, Huang Z, Xu Y, Li R, Hong H (**2022**) Novel membranes with extremely high permeability fabricated by 3D printing and nickel coating for oil/water separation. *J. Mater. Chem. A* 10:12055-61. https://doi.org/10.1039/D2TA01971J

210 Li G, Mo X, Wang Y, Chan CY, Chan KC (**2019**) All 3d-printed superhydrophobic/oleophilic membrane for robotic oil recycling. *Adv. Mater. Interfaces* 6:1900874. https://doi.org/10.1002/admi.201900874

211 Xu W, Zhang Z, Cai X, Hong Y, Lin T, Lei T (**2021**) Design aspects of (super)hydrophobic mesh-based oil-collecting device with improved efficiency. *Appl. Sci.* 3:135. https://doi.org/10.1007/s42452-021-04179-2

212 He CH, He JH, Sedighi HM (**2020**) Fangzhu : An ancient Chinese nanotechnology for water collection from air: History, mathematical insight, promises, and challenges. *Math. Methods in the Appl. Sci.* https://doi.org/10.1002/mma.6384

213 Ju J, Bai H, Zheng Y, Zhao T, Fang R, Jiang L (**2012**) A multi-structural and multi-functional integrated fog collection system in cactus. *Nat. Commun.* 3:1247. https://doi.org/10.1038/ncomms2253

214 Lorenceau É, QuÉRÉ D (**2004**) Drops on a conical wire. *J. Fluid Mech.* 510:29-45. https://doi.org/10.1017/S0022112004009152

215 Han S, Sung J, So H (**2021**) Simple fabrication of water harvesting surfaces using three-dimensional printing technology. *Int. J. Precision Manuf. Technol.* 8:1449-59. https://doi.org/10.1007/s40684-020-00263-x

216 Bai H, Wang L, Ju J, Sun R, Zheng Y, Jiang L (**2014**) Efficient water collection on integrative bioinspired surfaces with star-shaped wettability patterns. *Adv. Mater.* 26:5025-30. https://doi.org/10.1002/adma.201400262

217 Yu Z, Yun FF, Wang Y, Yao L, Dou S, Liu K, Jiang L, Wang X (**2017**) Desert beetle-inspired superwettable patterned surfaces for water harvesting. *Small* 13:1701403. https://doi.org/10.1002/smll.201701403

218 Xu C, Feng R, Song F, Wang XL, Wang YZ (**2018**) Desert beetle-inspired superhydrophilic/superhydrophobic patterned cellulose film with efficient water collection and antibacterial performance. *ACS Sustainable Chem. Eng.* 6:14679-84. https://doi.org/10.1021/acssuschemeng.8b03247

219 Li X, Yang Y, Liu L, Chen Y, Chu M, Sun H, Shan W, Chen Y (**2020**) 3D-Printed Cactus-Inspired Spine Structures for Highly Efficient Water Collection. *Adv. Mater. Interfaces* 7:1901752. https://doi.org/10.1002/admi.201901752

220 Ricco P, Skote M, Leschziner MA (**2021**) A review of turbulent skin-friction drag reduction by near-wall transverse forcing. *Prog. Aerosp. Sci.* 123:100713. https://doi.org/10.1016/j.paerosci.2021.100713

221 Bixler GD, Bhushan B (**2013**) Fluid drag reduction and efficient self-cleaning with rice leaf and butterfly wing bioinspired surfaces. *Nanoscale* 5:7685-710. https://doi.org/10.1039/C3NR01710A

222 Wen L, Weaver JC, Lauder GV (**2014**) Biomimetic shark skin: design, fabrication and hydrodynamic function. **J. Exp. Biol.** 217:1656-66. https://doi.org/10.1242/jeb.097097

223 Domel AG, Domel G, Weaver JC, Saadat M, Bertoldi K, Lauder GV (**2018**) Hydrodynamic properties of biomimetic shark skin: effect of denticle size and swimming speed. *Bioinspir. Biomim.* 13:056014. https://doi.org/10.1088/1748-3190/aad418

224 Lauder GV, Wainwright DK, Domel AG, Weaver JC, Wen L, Bertoldi K (**2016**) Structure, biomimetics, and fluid dynamics of fish skin surfaces. *Phys. Rev. Fluids* 1:060502. https://doi.org/10.1103/PhysRevFluids.1.060502

225 Liu Y, Zhang H, Wang P, He Z, Dong G (**2022**) 3D-printed bionic superhydrophobic surface with petal-like microstructures for droplet manipulation, oil-water separation, and drag reduction. *Mater. Des.* 219:110765. https://doi.org/10.1016/j.matdes.2022.110765

226 Liu X, Zhang X, Chen Q, Pan Y, Liu C, Shen C (**2021**) A simple superhydrophobic/superhydrophilic Janus-paper with enhanced biocompatibility by PDMS and candle soot coating for actuator. *Chem. Eng. J.* 406:126532. https://doi.org/10.1016/j.cej.2020.126532

227 Mirvakili SM, Hunter IW (**2018**) Artificial muscles: mechanisms, applications, and challenges. *Adv. Mater.* 30:1704407. https://doi.org/10.1002/adma.201704407

228 Guo H, Dai W, Miao Y, Wang Y, Ma D, Xue W (**2018**) Sustained heparin release actuator achieved from thermal and water activated shape memory hydrogels containing main-chain LC units. *Chem. Eng. J.* 339:459-67. https://doi.org/10.1016/j.cej.2018.02.009

229 Ma C, Lu W, Yang X, He J, Le X, Wang L, Zhang J, Serpe MJ, Huang Y, Chen T (**2018**) Bioinspired anisotropic hydrogel actuators with on–off switchable and color-tunable fluorescence behaviors. *Adv. Funct. Mater.* 28:1704568. https://doi.org/10.1002/adfm.201704568

230 Zhao Z, Kuang X, Yuan C, Qi HJ, Fang D (**2018**) Hydrophilic/Hydrophobic composite shape-shifting structures. *ACS Appl. Mater. Interfaces* 10:19932-9. https://doi.org/10.1021/acsami.8b02444

231 Yang W, Zhao Z, Pan M, Gong L, Wu F, Huang C, Wang X, Wang J, Zeng H (**2022**) Mussel-inspired polyethylene glycol coating for constructing antifouling membrane for water purification. *J. Colloid Interface Sci.* 625:628-39. https://doi.org/10.1016/j.jcis.2022.06.038

232 Xie A, Cui J, Liu Y, Xue C, Wang Y, Dai J (**2021**) Preparation of Janus membrane based on biomimetic polydopamine interface regulation and superhydrophobic attapulgite spraying for on-demand oil-water emulsion separation. *J. Membr. Sci.* 627:119242. https://doi.org/10.1016/j.memsci.2021.119242

233 Wei Y, Qi H, Gong X, Zhao S (**2018**) Specially Wettable Membranes for Oil–Water Separation. *Adv. Mater. Interfaces* 5:1800576. https://doi.org/10.1002/admi.201800576

234 Zhang L, Li H, Lai X, Su X, Liang T, Zeng X (**2017**) Thiolated graphene-based superhydrophobic sponges for oil-water separation. *Chem. Eng. J.* 316:736-43. https://doi.org/10.1016/j.cej.2017.02.030

235 Li F, Bhushan B, Pan Y, Zhao X (**2019**) Bioinspired superoleophobic/superhydrophilic functionalized cotton for efficient separation of immiscible oil-water mixtures and oil-water emulsions. *J. Colloid Interface Sci.* 548:123-30. https://doi.org/10.1016/j.jcis.2019.04.031

236 Wang X, Zhang J, Wang Y, Qin S, Pan Y, Tu Y, Liu X (**2023**) Superhydrophobic Thermoplastic Polyurethane Foam Fabricated by Phase Separation and Silica Coating for Oil-Water Separation. *Macromol. Rapid Commun.* 44:2300333. https://doi.org/10.1002/marc.202300333

237 Xu Y, Liao J, He R, Yang S, Luo Z, Xu M, Tao Y, Wang X (**2024**) Superhydrophobic and oleophilic polyurethane sponge for oil/water separation. *Mater. Today Commun.* 38:107658. https://doi.org/10.1016/j.mtcomm.2023.107658

238 Wang X, Hassan A, Boudaoud H, Xue F, Zhou Z, Liu X (**2023**) A review on 3D printing of bioinspired hydrophobic materials: oil-water separation, water harvesting, and diverse applications. *Adv. Compos. Hybrid Mater.* 6:170. https://doi.org/10.1007/s42114-023-00740-2

239 Yan C, Ji Z, Ma S, Wang X, Zhou F (**2016**) 3D Printing as Feasible Platform for On-Site Building Oil-Skimmer for Oil Collection from Spills. *Adv. Mater. Interfaces* 3:1600015. https://doi.org/10.1002/admi.201600015

240 Acierno D, Patti A (**2023**) Fused Deposition Modelling (FDM) of Thermoplastic-Based Filaments: Process and Rheological Properties—An Overview. *Mater.* 16:7664. https://doi.org/10.3390/ma16247664

241 Liu X, Zhang M, Hou Y, Pan Y, Liu C, Shen C (**2022**) Hierarchically Superhydrophobic Stereo-Complex Poly (Lactic Acid) Aerogel for Daytime Radiative Cooling. *Adv. Funct. Mater.* 32:2207414. https://doi.org/10.1002/adfm.202207414

242 Chen F, Wang Y, Tian Y, Zhang D, Song J, Crick CR, Carmalt CJ, Parkin IP, Lu Y (**2022**) Robust and durable liquid-repellent surfaces. *Chem. Soc. Rev.* 51:8476-583. https://doi.org/10.1039/D0CS01033B

243 Wang T, Xing L, Qu M, Pan Y, Liu C, Shen C, Liu X (**2022**) Superhydrophobic polycarbonate blend monolith with micro/nano porous structure for selective oil/water separation. *Polymer* 253:124994. https://doi.org/10.1016/j.polymer.2022.124994

244 Zhou Y, Li M, Su B, Lu Q (**2009**) Superhydrophobic surface created by the silver mirror reaction and its drag-reduction effect on water. *J. Mater. Chem.* 19:3301-6. https://doi.org/10.1039/B819251K

245 Zouboulis AI, Avranas A (**2000**) Treatment of oil-in-water emulsions by coagulation and dissolved-air flotation. *Colloids Surf. A Physicochem. Eng. Asp.* 172:153–61. https://doi.org/10.1016/S0927-7757(00)00561-6

246 Rubio J, Souza ML, Smith RW (**2002**) Overview of flotation as a wastewater treatment technique. *Miner. Eng.* 15:139–55. https://doi.org/10.1016/S0892-6875(01)00216-3

247 Cui Z, Ssa M, Zhao M, Wu J, Liu X, Si J, Wang Q (**2022**) Thermoplastic polyurethane/titania/polydopamine (TPU/TiO_2/PDA) 3-D porous composite foam with outstanding oil/water separation performance and photocatalytic dye degradation. *Adv. Compos. Hybrid Mater.* 5:2801–16. https://doi.org/10.1007/s42114-022-00503-5

248 Xue F, Robin G, Boudaoud H, Cruz Sanchez FA, Daya EM (**2022**) General methodology to investigate the effect of process parameters on the vibration properties of structures produced by additive manufacturing using fused filament fabrication. *JOM* 74:1166–75. https://doi.org/10.1007/s11837-021-05051-9

249 Vishwakarma J, Chattopadhyay K, Srinivas NCS (**2023**) Influence of build orientation and aging on corrosion behaviour of 18Ni300 maraging steel produced via powder bed fusion using laser beam (PBF-LB). *Mater. Today Commun.* 35:105825. https://doi.org/10.1016/j.mtcomm.2023.105825

250 Lai J, Wang C, Wang M (**2021**) 3D printing in biomedical engineering: Processes, materials, and applications. *Appl. Phys. Rev.* 8:021322. https://doi.org/10.1063/5.0024177

251 Joshi SC, Sheikh AA (**2015**) 3D printing in aerospace and its long-term sustainability. *Virtual Phys. Prototyp.* 10:175–85. https://doi.org/10.1080/17452759.2015.1111519

252 Hu L, Jiang G (**2017**) 3D printing techniques in environmental science and engineering will bring new innovation. *Environ. Sci. Technol.* 51:3597–99. https://doi.org/10.1021/acs.est.7b00302

253 Koh JJ, Lim GJH, Zhou X, Zhang X, Ding J, He C (**2019**) 3D-printed anti-fouling cellulose mesh for highly efficient oil/water separation applications. *ACS Appl. Mater. Interfaces* 11:13787–95. https://doi.org/10.1021/acsami.9b01753

254 Chen Z, Zhang D, Peng E, Ding J (**2019**) 3D-printed ceramic structures with in situ grown whiskers for effective oil/water separation. *Chem. Eng. J.* 373:1223–32. https://doi.org/10.1016/j.cej.2019.05.150

255 Li X, Shan H, Zhang W, Li B (**2020**) 3D printed robust superhydrophilic and underwater superoleophobic composite membrane for high efficient oil/water separation. *Sep. Purif. Technol.* 237:116324. https://doi.org/10.1016/j.seppur.2019.116324

256 Krishnanand S, Soni S, Taufik M (**2021**) Design and assembly of fused filament fabrication (FFF) 3D printers. *Mater. Today Proc.* 46:5233–41. https://doi.org/10.1016/j.matpr.2020.08.627

257 Lv W, Mei Q, Xiao J, Du M, Zheng Q (**2017**) 3D multiscale superhydrophilic sponges with delicately designed pore size for ultrafast oil/water separation. *Adv. Funct. Mater.* 27:1704293. https://doi.org/10.1002/adfm.201704293

258 Kechagias J, Chaidas D, Vidakis N, Salonitis K, Vaxevanidis NM (**2022**) Key parameters controlling surface quality and dimensional accuracy: A critical review of FFF process. *Mater. Manuf. Process.* 37:963–84. https://doi.org/10.1080/10426914.2022.2032144

259 Wei W, Wu H, Zhang J, Zhang M, Yuan L, Zhou Z, Long Y (**2025**) Model decomposition method for minimizing the consumption of support structure for FFF. *J. Manuf. Process.* 133:395–407. https://doi.org/10.1016/j.jmapro.2024.11.068

260 Chaidas D, Kechagias JD (**2022**) An investigation of PLA/W parts quality fabricated by FFF. *Mater. Manuf. Process.* 37:582–90. https://doi.org/10.1080/10426914.2021.1944193

261 Yang R, Xie F, Li Y, Wang X, Pan Y, Liu C, Shen C, Liu X (**2024**) Advancing thermal comfort: An innovative SiO_2 microsphere-decorated shish-kebab film composite for enhanced personal cooling. *Adv. Nanocompos.* 1:86–93. https://doi.org/10.1016/j.adna.2024.02.001

262 Hubbert MK (**1956**) Darcy's law and the field equations of the flow of underground fluids. *Trans. AIME* 207:222–39. https://doi.org/10.2118/749-G